Inclusive Charmonium Production Above 4 GeV at the BESIII Experiment

Dissertation
zur Erlangung des Doktorgrades
der Naturwissenschaften

vorgelegt beim Fachbereich Physik
der Johann Wolfgang Goethe-Universität
in Frankfurt am Main

von
Simon Nakhoul
aus, Kafaraabida, Libanon

Frankfurt am Main (2020)
D30

vom Fachbereich Physik der
Johann Wolfgang Goethe-Universität als Dissertation angenommen.

Dekan: Prof. Dr. Michael Lang

Gutachter: Prof. Dr. Klaus Peters
Prof. Dr. Wolfgang Gradl

Datum der Disputation:

ABSTRACT

In the last two decades, new unpredicted charmonium-like states with extraordinary characteristics have been observed experimentally. These states also known as the XYZ states, e.g., the $Y(4260)$ [1] or the $X(3872)$ [2], are mostly interpreted as QCD allowed exotic hadrons. One of the leading hadron physics experiments in the world, the Beijing Electron Spectrometer III (BESIII) [3] at the Beijing Electron-Positron Collider II (BEPCII) is aiming towards revealing the internal structure of these states. It has brought numerous breakthrough discoveries including the discovery of the charged $Z_c(3900)$ [4]. In order to understand the nature of the $Y(4260)$ state and its decay patterns, an inclusive analysis is performed for different recoil systems ($\pi^+\pi^-$, K^+K^- and $K^\pm\pi^\mp$) using the BESIII data samples for center of mass energies above 4 GeV collected between 2013 and 2019.
The aim of this analysis is twofold: on one hand, we search for new unobserved charmonium-like decay channels using the missing mass technique and on the other hand, it provides an accurate inclusive cross section measurements for $e^+e^- \to X_{c\bar{c}}\pi^+\pi^-$, with the $X_{c\bar{c}}$ being the J/ψ, h_c and $\psi(2S)$, respectively. Two resonant structures are observed in the inclusive energy dependent Born cross section of $e^+e^- \to h_c\pi^+\pi^-$, which is consistent with the BESIII exclusive measurements. The first resonance is the $Y(4220)$ with a mass of (4232.4 $\pm$ 3.96) MeV and a width of (71.31 $\pm$ 10.72) MeV, while the second one is the $Y(4390)$ with a mass of (4387.5 $\pm$ 4.58) MeV and a width of (110.2 ± 30.86) MeV. Moreover, the energy dependent cross section of $e^+e^- \to J\psi\pi^+\pi^-$ is investigated, in which two resonances have consistently been observed with the previous BESIII exclusive studies, namely, the $Y(4220)$ with a mass of (4224.0 ± 1.8) MeV and a width of (47.91 ± 2.33) MeV and the $Y(4320)$ with a mass of (4317.0 ± 7.9) MeV and a width of (135 ± 20.5) MeV. In the ($K^\pm\pi^\pm$) recoil system, possible $Y(4260)$ open charm decay channels are investigated. Two enhancements are observed in the inclusive energy dependent cross section of $e^+e^- \to D^0\bar{D}^0[K^\pm\pi^\mp]$ above 4.13 GeV, which could possibly be the $\psi(4160)$ and the $\psi(4415)$. The first one has a mass of (4187.0 ± 3.05) MeV and a width of (78.87 ± 6.62) MeV, while the second one has a mass of (4428 ± 4.28) MeV and a width of (149.8 ± 7.28) MeV.

KURZFASSUNG

In den letzten zwei Jahrzehnten wurden experimentell neue unvorhergesehene charmonium-ähnlichen Zustände mit außergewöhnlichen Eigenschaften und Verhaltensweisen beobachtet. Diese Zustände, die auch als XYZ-Zustände bekannt sind, z.B. $Y(4260)$ [1] oder $X(3872)$ [2], werden meist als QCD-erlaubte exotische Hadronen interpretiert. Eines der weltweit führenden Experimente zur Hadronenphysik, das Beijing Electron Spectrometer III (BESIII) [3] am Beijing Electron-Positron Collider II (BEPCII), arbeitet daran, die interne Struktur dieser Zustände aufzudecken. Es hat zahlreiche bahnbrechende Entdeckungen gemacht, einschließlich der ersten Beobachtung des elektrisch geladenen $Z_c(3900)$ [4]. Um die Natur des $Y(4260)$-Zustands und seine Zerfälle zu verstehen, wird eine umfassende Analyse für verschiedene Rückstoßsysteme ($\pi^+\pi^-$, K^+K^-, $K^\pm\pi^\mp$...) basierend auf den BESIII-Datensätzen für Schwerpunktsenergien über 4 GeV durchgeführt welche zwischen 2013 und 2019 aufgenommen wurden. Das Ziel dieser Analyse ist zweifältig: einerseits, suchen wir nach neuen unbeobachteten Charmonium-ähnlichen Zerfallskanälen mit der sogenannten "Missing Mass"-Technik und andererseits, führen wir eine genaue Messung der inklusiven Wirkungsquerschnitt für $e^+e^- \to X_{c\bar{c}}\pi^+\pi^-$ durch, mit $X_{c\bar{c}}$ ist das J/ψ, h_c und $\psi(2S)$. Zwei Resonanzstrukturen werden im inklusiven energieabhängigen Wirkungsquerschnitt von $e^+e^- \to h_c\pi^+\pi^-$ beobachtet, was mit den bislang erfolgten exklusiven Messungen von BESIII übereinstimmt. Dies ist zum einen die erste Resonanz, das $Y(4220)$, mit einer Masse von (4232.4 ± 3.96) MeV und einer Breite von (71.31 ± 10.72) MeV, zum anderen das $Y(4390)$ mit einer Masse von (4387.5 ± 4.58) MeV und eine Breite von (110.2 ± 30.86) MeV. Im energieabhängige Wirkungquerschnitt der Reaktion $e^+e^- \to J/\psi\pi^+\pi^-$ werden ebenfalls zwei Resonanzen in Übereinstimmung mit den vorherigen exklusiven BESIII-Studien beobachtet. Beim $Y(4220)$ wird eine Masse von (4224.0 ± 1.8) MeV und eine Breite von (47.91 ± 2.33) MeV beobachtet und für das $Y(4320)$ eine Masse von (4317.0 ± 7.9) MeV und eine Breite von (135 ± 20.5) MeV. Auch im Rückstoßsystem ($K^\pm\pi^\pm$) mögliche Zerfallskanäle des $Y(4260)$ untersucht worden. Im inklusiven Energie-abhängige Wirkungsquerschnitt der Reaktion $e^+e^- \to D^0\bar{D}^0[K^\pm\pi^\mp]$ werden zwei Resonanzen oberhalb von 4.13 GeV beobachtet, welche möglicherweise die Zustände $\psi(4160)$ und $\psi(4415)$ sind. Der erste hat eine Masse von (4187.0 ± 3.05) MeV und eine Breite von (78.87 ± 6.62) MeV, während der zweite eine Masse von (4428 ± 4.28) MeV und eine Breite von (149.8 ± 7.28) MeV hat.

Contents

CHAPTER 1

INTRODUCTION

1 Theoretical Background

1.1 The Standard Model of Particle Physics

All the matter we see around us in the universe is made of atoms which are composed of the sub-nuclear objects such as protons and neutrons. These hadrons are made of smaller particles named quarks and are bound together by a fundamental force called "the strong interaction". Understanding everything about this force and its behavior will help us to better understand our universe.

Besides the strong interaction, there are three other fundamental interactions that play very important roles in nature. Decays of subatomic particles are governed by the "weak interaction". Interactions of electrically charged particles are described by the "electromagnetic interaction". The "gravitational force" is concerned with massive bodies and gravity. Since the 1970's, the standard model of particle physics had great success in providing the best theoretical understanding of subatomic particles and three out of four of the above mentioned fundamental interactions. However, there are still so many uncharted corners of the subatomic world not reached or explained by the standard model. It has failed to answer many crucial questions including some aspects of the fundamental theory of the strong force (QCD) in the low-energy regime.

In the standard model there are seventeen fundamental particles: Six quarks, six leptons, four force-carrier particles and the Higgs boson. These elementary particles are organized in three generations and their properties are shown in table 1.1. The six quarks can be combined in pairs with antiquarks or triplets to make conventional mesons or baryons. A proton, for example as shown in figure 1.1, is a baryon composed of three quarks: up (u), up (u) and down (d). A pion is a meson that exists in different up/down quarks and antiquarks combinations: π^0(superposition of $u\bar{u}$ or $d\bar{d}$) , $\pi^+(u\bar{d})$ and $\pi^-(d\bar{u})$. The mesons and baryons are classified based on a set of quantum numbers J^{PC}. Where J is the total angular momentum, P is the spatial parity and C is the charge parity. This classification is discussed in detail in subsection 1.3.

Table 1.1: Properties of quarks and leptons.

Quark	up (u)	down (d)	charm (c)	strange (s)	top (t)	bottom (b)
mass[MeV/c^2]	$2.3^{+0.7}_{-0.5}$	$4.8^{+0.5}_{-0.3}$	1275 ± 25	95 ± 5	$(173.21 \pm 0.51) \times 10^3$	4180 ± 30
charge	$\frac{2}{3}e$	$-\frac{1}{3}e$	$\frac{2}{3}e$	$-\frac{1}{3}e$	$\frac{2}{3}e$	$-\frac{1}{3}e$
I(J^P)	$\frac{1}{2}(\frac{1}{2}^+)$	$\frac{1}{2}(\frac{1}{2}^+)$	$0(\frac{1}{2}^+)$	$0(\frac{1}{2}^+)$	$0(\frac{1}{2}^+)$	$0(\frac{1}{2}^+)$
Leptons	e	ν_e	μ	ν_μ	τ	ν_τ
mass[MeV/c^2]	0.511	$< 2.10^{-6}$	105.66	< 0.19	1776.82 ± 0.16	< 18.2
charge	$1e$	0	$1e$	0	$1e$	0

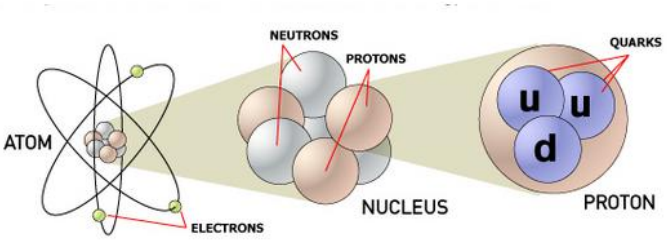

Figure 1.1: The atom's nucleus is composed of positively charged particles "protons" and neutral particles "neutrons". These nucleons are made of three smaller particles, the quarks.

The standard model is a re-normalizable quantum field theory based on a $SU(3)_c \otimes SU(2)_L \otimes U(1)$ local gauge symmetry providing a quantitative description of the electroweak and strong interactions. The electromagnetic and weak interactions are the manifestations of the same fundamental interaction, the electroweak force. These interactions are mediated by gauge bosons, their properties are summarized in table 1.2. The photon (γ) is the force carrier of the electromagnetic interaction, the $W^\pm$ and Z bosons are the mediators of the weak interaction and the strong interaction is mediated by eight gluons (g).

Table 1.2: Properties of the gauge bosons of the standard model. The masses are taken from the particle data group [5].

Gauge boson	mass (GeV/c^2)	spin	interaction
photon	0	1	electromagnetic
$W^\pm$	80.3 ± 00.15	1	weak
Z	91.187 ± 0.002	1	weak
gluon	0	1	strong

1.2 The Theory of Quantum Chromodynamics (QCD)

In the 1960s, new particles were being discovered, in particular the Δ resonances. These particles proved to be crucial to establish the Quark model, the notion of the color charge and later on the theory of quantum chromodynamics (QCD). Particles were described by Murray Gell-Mann and Yuval Neeman in a scheme based on the SU(3) symmetry group. For example, the ground-state baryons (p, n, Σ, Ξ ...) were represented as octet and decuplet shown in Fig 1.2.

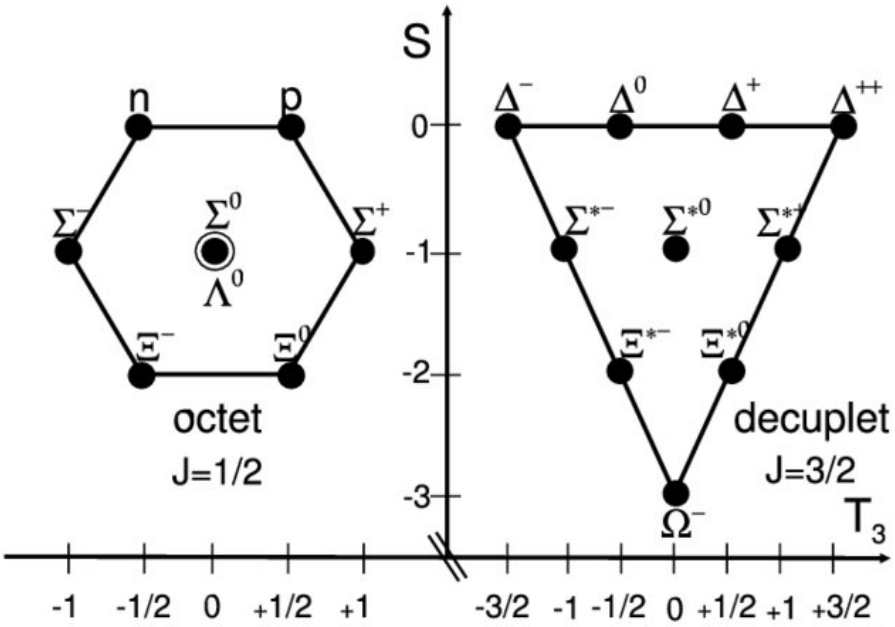

Figure 1.2: SU(3) flavor octet and decuplet of ground-state baryons characterized by their strangeness S (vertical axis) and isospin component T3 (horizontal axis) [6]

The Δ^{++} baryon with a spin of 3/2, is interpreted as a bound state of three u quarks with same spin alignment. This means that the total wave function of the three quarks is completely symmetric. However, according to the Pauli principle, the wave function for the exchange of identical fermions must be anti-symmetric. In order to solve this problem, an additional quantum number named "color" was introduced.
It was suggested that (anti-)quarks carry a (anti-)color charge (red $\overset{(-)}{R}$, green $\overset{(-)}{G}$ and blue $\overset{(-)}{B}$) while the mediators of this force, the massless gluons, come in eight different combinations of color and anti-color charges. The color group was interpreted as a gauge group and the resulting gauge theory was named quantum chromodynamics or QCD. Since then, it was known to be the part of the standard model concerned exclusively with the strong force.
The dynamics of the quarks and gluons are described by the QCD Lagrangian. It is given as:

$$\mathcal{L}_{\mathcal{QCD}} = \Sigma_q \bar{\psi}_{q,a}(i\gamma^\mu \partial_u \delta_{ab} - g_s \gamma^\mu t^C_{ab} \mathcal{A}^C_\mu - m_q \delta_{ab})\psi_{q,b} - \frac{1}{4} F^A_{\mu\nu} F^{A\mu\nu}. \tag{1.1}$$

The γ^μ are the Dirac γ-matrices. The $\psi_{q,a}$ are quark-field spinors for a quark of flavor q and mass m_q, with a color-index a that runs from $a = 1$ to $N_c = 3$. i.e. quarks come in three colors. The $\mathcal{A}^C_\mu$ correspond to the gluon fields, with C running from 1 to N_c^2 - 1 = 8, i.e. there are eight different

kind of gluons. The quantity g_s (or $\alpha_s = \frac{g_s^2}{4\pi}$) is the coupling constant of QCD. The field tensor $F^A_{\mu\nu}$ is given by:

$$F^A_{\mu\nu} = \partial_\mu \mathcal{A}^{\mathcal{A}}_\nu - \partial_\nu \mathcal{A}^{\mathcal{A}}_\mu - g_s f_{ABC} \mathcal{A}^B_\mu \mathcal{A}^C_\nu, \tag{1.2}$$

where the f_{ABC} are the structure constants of the SU(3) group. [7]
The diagrams of the different quark/gluon interactions in QCD are shown in figure 1.3. Gluons can decay to a couple of quarks, be radiated by quarks or interact also with other gluons.

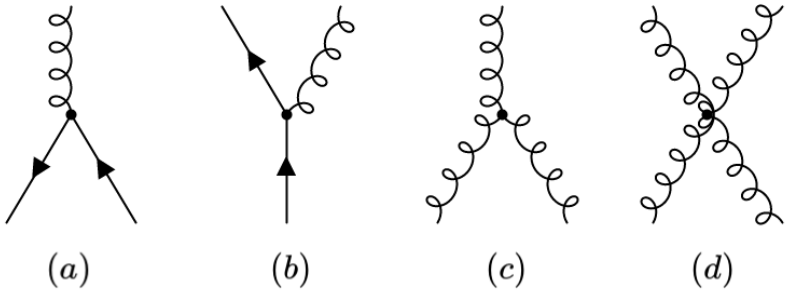

Figure 1.3: Interactions of quarks and gluons in QCD. (a) Decay of a gluon to a quark and antiquark pair. (b) Radiation of a gluon by a quark. (c) Self coupling of three gluons. (d) Self coupling of four gluons.

The coupling $\alpha_s(Q^2)$ determines the strength of the interactions involving quarks and gluons in QCD and it is a function of the momentum transfer Q^2:

$$\alpha_s(Q^2) = \frac{12\pi}{(11n_c - 2n_f) \cdot \ln(Q^2/\Lambda^2_{QCD})}, \tag{1.3}$$

where Λ_{QCD} is a free parameter of QCD, n_c is the number of colors and n_f is the number of quark flavors. The dependence of the coupling strength on the momentum transfer is represented in figure 1.4 At short distances (high Q^2) $\alpha_s(Q^2)$ is crucial to match the accuracy of hadron scattering experiments and to test high-energy models unifying strong and electroweak forces. At large distances (low Q^2) it is necessary in order to describe hadronic structure, quark confinement and hadronization processes.

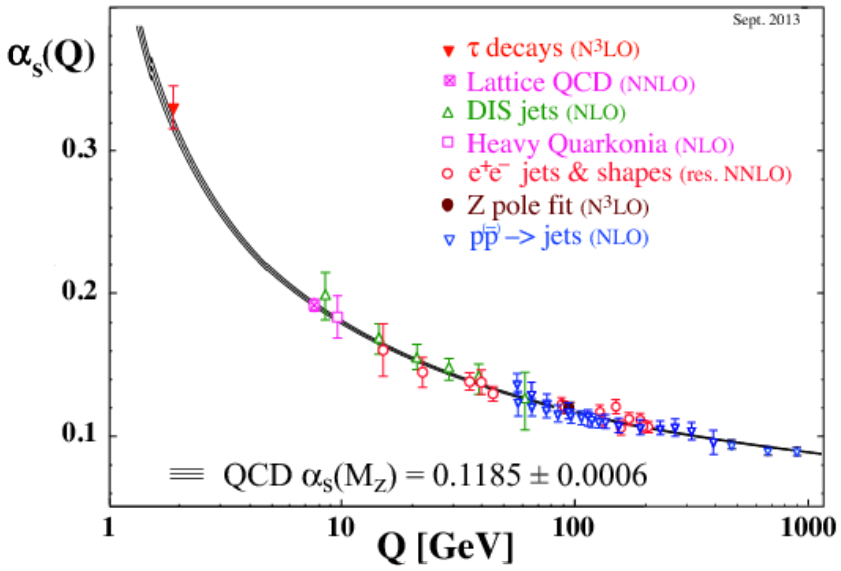

Figure 1.4: Dependence of the strong coupling constant α_s on the momentum transfer Q [5].

$\alpha_s(Q)$ decreases with increasing momentum transfer. For short distances, quarks are considered asymptotically free. On the other hand, at larger distances, the interaction between quark pairs is very strong and it is impossible to detach individual quarks from hadrons. This effect is called "confinement".

1.3 Charmonium Spectroscopy

In November 1974, a charm-anticharm ($c\bar{c}$) meson named J/ψ with a mass of roughly 3100 MeV/c^2 was discovered at SLAC and Brookhaven [8]. Shortly afterwards SLAC discovered another narrow charmonium state called $\psi(2S)$ which is in fact the first radial excitation of the J/ψ. In the following years other predicted charmonium states ($h_c, \eta_c, \chi_{c1}, \chi_{c2}$) were observed experimentally. These discoveries contributed to the creation of the charmonium spectroscopy field. A field with an aim to discover, predict and understand all ($c\bar{c}$) mass states.
Contrary to the light quarks (u, d, s), the charm quark is heavy with a mass of $m_c = 1.275\ ^{0.025}_{0.035}$ GeV/c^2 [5]. Therefore $c\bar{c}$ bound states can be described by non-relativistic potential models. In analogy to the positronium potential, an effective potential can be derived. The Cornell potential is given by [9]:

$$V = -\frac{4\alpha_s(r)}{3r} + k \cdot r, \tag{1.4}$$

where r is the distance between the quark and antiquark and k is the string tension. These models allows us to organize all the known charmonium and charmonium-like states in a diagram called the "charmonium spectrum".
In this diagram, states are labeled using the X(nL) notation, where L is the angular momentum between two quarks, for different values of L a capital letter is assigned (S, P, D, F) and $n = 1, 2, 3...$ is the radial excitation. The location of a state on the charmonium spectrum is determined by its

quantum numbers J^{PC}, where J is the total angular momentum, given by:

$$|L - S| \leqslant J \leqslant L + S \tag{1.5}$$

and S is the spin of the quark and antiquark pair. The different allowed J^{PC} combinations for a simple $q\bar{q}$ system are shown in table 1.3.

L	S	J^{PC}	L	S	J^{PC}	L	S	J^{PC}
0	0	0^{-+}	1	0	1^{+-}	2	0	2^{-+}
0	1	1^{--}	1	1	0^{++}	2	1	1^{--}
			1	1	1^{++}	2	1	2^{--}
			1	1	2^{++}	2	1	3^{--}

Table 1.3: The allowed J^{PC} quantum numbers for $q\bar{q}$ systems.

The spectrum of the established charmonium states is shown in figure 1.5. The vertical line represents the mass of the charmonium states in MeV. They are ordered horizontally based on their J^{PC} quantum numbers.

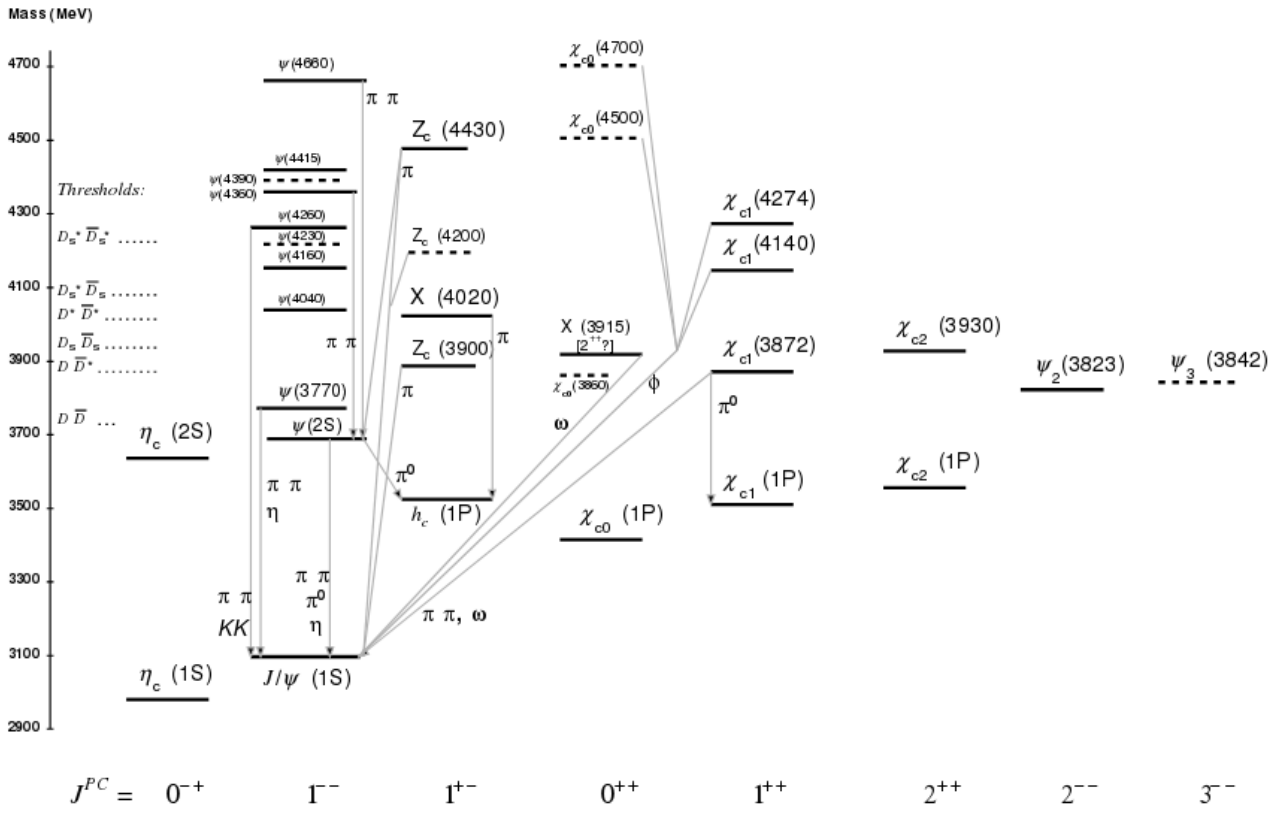

Figure 1.5: The spectrum of established charmonium states with their hadronic transitions ordered according to J^{PC} quantum numbers [5]

The arrows indicate the transition between different charmonium states. For instance, the

arrow between $\psi(2S)$ and $J/\psi(1S)$ represents the following three decay channels of the $\psi(2S)$: $\psi(2S) \to J/\psi\pi\pi$, $J/\psi\pi^0$, $J/\psi\eta$.

1.4 Exotic states

within QCD, the existence of "exotic" hadrons is predicted, which have more complex structures than the quark-antiquark mesons or the three quarks baryons. The most common combinations are listed below and represented in Fig 1.6:

- **Tetraquarks**: states containing two tightly bound quark-antiquark pair ($qq\bar{q}\bar{q}$).
- **Molecular states**: two mesons forming bound systems separated and bound by pion-exchange at long distances and gluon exchange at shorter distances.
- **Hybrid states**: states containing a mixture of quarks and excited gluons ($q\bar{q}g$).
- **Glueballs**: pure gluonic states entirely composed of gluons, e.g., two or three gluons (gg, ggg) .
- **Pentaquarks**: particles consisting of a bound system of four quarks and one antiquark ($qqqq\bar{q}$).

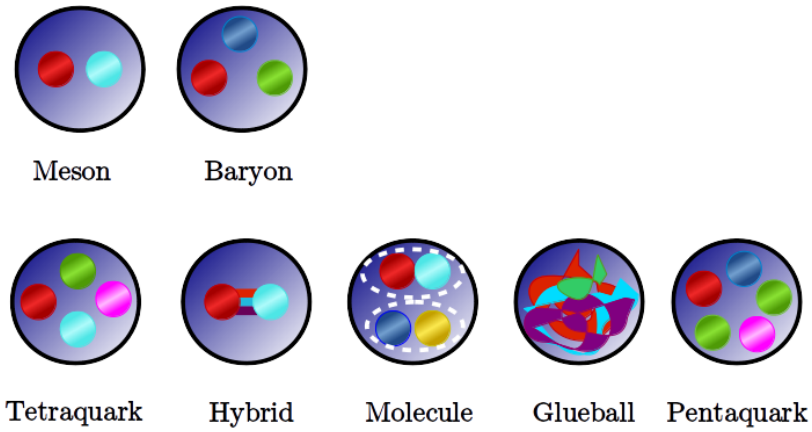

Figure 1.6: Representation of standard hadrons and the QCD allowed exotic hadrons

Based on the way these exotic hadrons are distinguished from the conventional mesons, three different categories could be defined:

- **The first order:** particles that possess exotic values of principal quantum numbers, e.g., the charge $Q > 1$ or the strangeness $S > 1$.
- **The second order or spin-exotics:** refers to mesons possessing J^{PC} combinations that do not appear in table 1.3, i.e. forbidden J^{PC} combinations: 0^{--}, 0^{+-}, $1^{-+}$and 2^{+-}.

- **The third order:** the most common category and the hardest to distinguish from conventional mesons. These states do not possess any obvious exotic quantum numbers or features. The XYZ states belong to this category and they are discussed in details in the next section.

1.5 The Charmonium-like XYZ States

XYZ refers to a wide range of unexpected experimentally detected particles that do not appear to fit in the standard picture of charmonium states. The Y refers to the vector states with $J^{PC} = 1^{--}$, the Z label is assigned to the charged charmonium-like states and the X particles are the ones that do not follow a Y or Z label.
The XYZ states are expected to be strong candidates for non-$q\bar{q}$ mesons. Ever since the observation of the first of these states in 2003, they generated great interest by both experimentalists and theorists. Huge efforts by particle physics experiments are being invested in understanding their nature and behavior. The XYZ states could be produced in different mechanisms and experiments as illustrated in figure 1.7. In the BaBar [10] and LHCb [11] experiments, the XYZ states are produced via B-meson decays. In e^+e^- experiments, for instance at BESIII they can be produced directly via annihilation while at BELLE [12] they can be detected via double charm production. Other production mechanisms could include photo-production at GlueX [13] and proton anti-proton annihilation at the PANDA experiment at the Facility for Antiproton and Ion Research in Darmstadt (FAIR) [13].

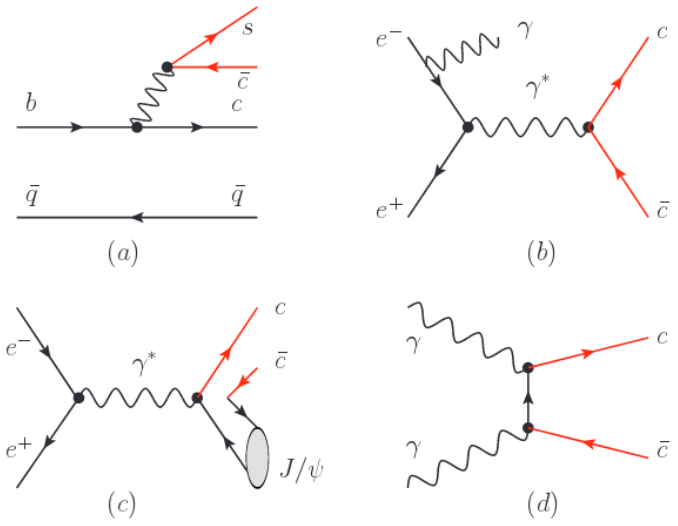

Figure 1.7: The diagrammatic description of some of the production mechanism of the charmonium and the XYZ charmonium-like states. (a) B meson decay ($B \to K + XYZ$), (b) e^+e annihilation ($e^+e^- \to XYZ$), (c) double charm production ($e^+e^- \to J/\psi + XYZ$), (d) $\gamma\gamma$ fusion process ($\gamma\gamma \to XYZ$) [15]

The mass spectrum of the predicted and unpredicted charmonium states based on the potential model calculations is shown in figure 1.8. The red and purple colored boxes are the XYZ states

observed but never been predicted. The yellow colored boxes are the predicted states by the potential models and confirmed experimentally. The gray colored boxes are the predicted states but not yet discovered. Below the $D\bar{D}$ open-charm threshold (at 3.73 GeV) there is an excellent agreement between theory predictions and experimental observations. However, the region above the threshold is populated with many unexpected XYZ and non-observed states.
If restricted to only the confirmed states, the XYZ family in the charmonium sector is comprised of four charged states ($Z_c(3900)^{\pm}$, $Z_c(4020)^{\pm}$, $Z_c(4200)^{\pm}$ and $Z_c(4430)^{\pm}$) and four neutral states ($X(3872)$, $Y(4260)$, $Y(4360)$ and $Y(4660)$). A quarkonium meson is composed of a heavy quark and its own antiquark, making it a neutral particle. So the observations of these charmonium-like charged particles, point out the fact that they are not conventional $c\bar{c}$ states. The neutral ones, also do not fit in the quark model since their masses and properties are in disagreement with the predictions. In the next section, an introduction to several important XYZ observations is given.

1.5.1 Experimental Status of Selected XYZ States

The $X(3872)$ is the first charmonium-like particle that was discovered by BELLE in $B^+ \to K^+X[\to \pi^+\pi^- J/\psi]$ [2] and shortly after confirmed by BaBar. With a mass of 3872 MeV/c^2 and a $J^{PC} = 1^{++}$, the $X(3872)$ cannot be identified as $\chi'_{c1}(2^3P_1)$ due to a predicted 100 MeV mass difference between the two. Since the mass of this state is indistinguishable from the $D^0\bar{D}^{0*}$ mass threshold, one of the most prominent interpretations of the $X(3872)$ is a $D^0\bar{D}^{0*}$ molecule.

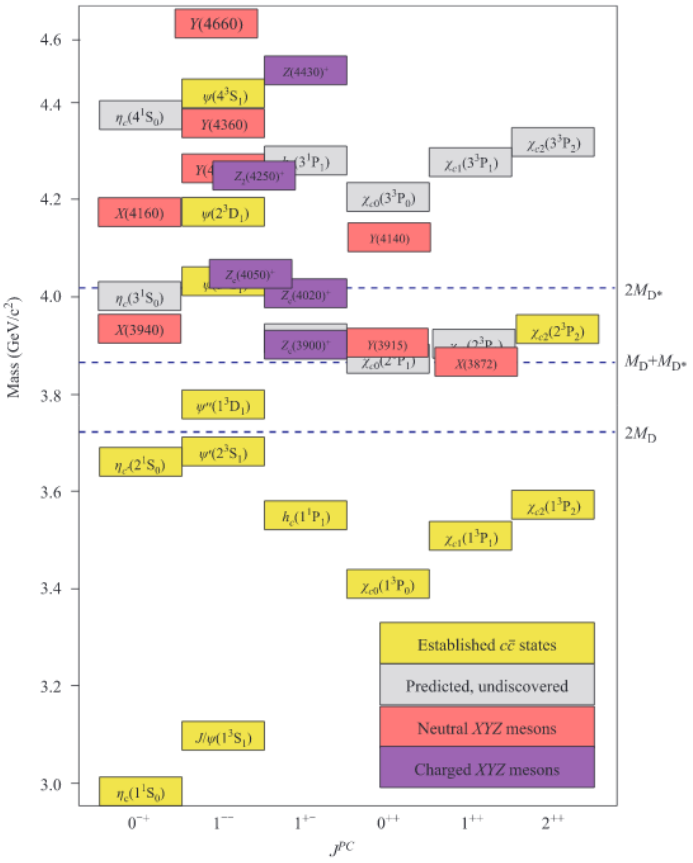

Figure 1.8: The mass spectrum of the predicted and unpredicted charmonium states.[16]

The first charged charmonium-like state experimentally observed is the $Z_c(4430)^{\pm}$. The Belle experiment made this discovery in 2007 in the $\pi^{\pm}\psi(2S)$ produced in B decays [17]. This was followed by another ground-breaking discovery in 2013 by the BESIII experiment. The $Z_c(3900)^{\pm}$ with a mass of 3900 MeV/c^2 and a width of about 30 MeV was observed in the $\pi^{\pm}J/\psi$ system [4] and confirmed by Belle shortly after [18]. The $Z_c(3900)^{\pm}$ main decay channels are $\pi^{\pm}J/\psi$ and $(DD^*)^{\pm}$, which means, it should contain charm-anticharm quarks. If the $Z_c(3900)^{\pm}$ is a higher excited $c\bar{c}$ meson, it can not be charged. The best explanation is that it is an unconventional state composed of four quarks $c\bar{c}q\bar{q}$ $(q = u, d)$. There are different theories and speculations on the nature of this state. The most popular and supported configurations are a molecular state, a hybrid or a compact tetraquark.

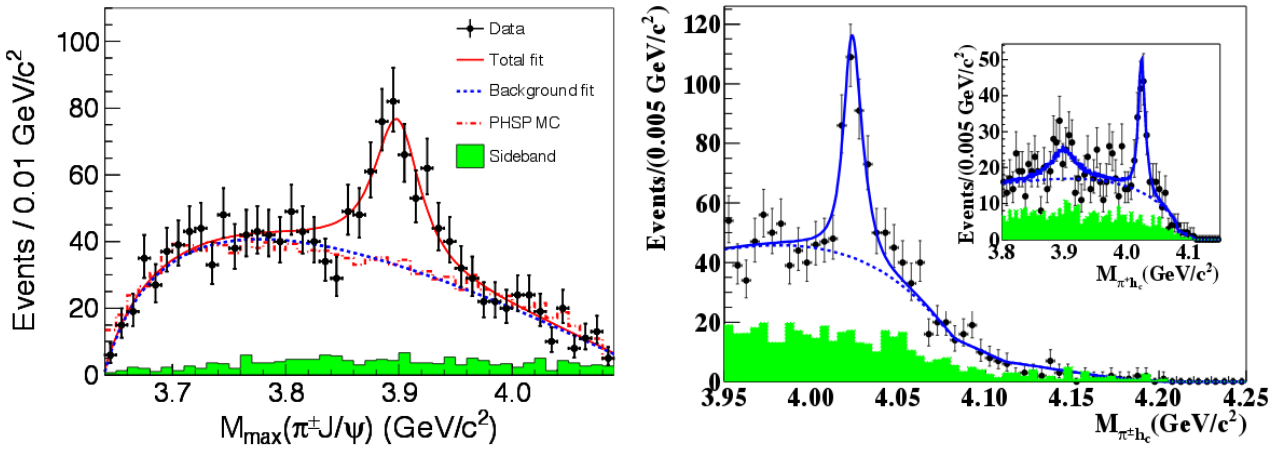

Figure 1.9: Left: The first observation of the $Z(4390)^{\pm}$ in the invariant mass of $(\pi^{\pm}J/\psi)$ at BESIII [4]. Right: the $Z_c(4020)$ signal observed in $e^+e \to \pi^{\pm}h_c$ at BESIII. [19]

In 2013, two vector Y states near 4220 MeV/c^2 and 4390 MeV/c^2 have been reported in $e^+e^- \to h_c\pi^+\pi^-$ by BESIII [20]. These resonances, also known as $Y(4220)$ and $Y(4390)$, have masses of (4216 ± 18) MeV/c^2, (4391.5 ± 6.3) MeV/c^2 and widths of (66 ± 12) MeV, (139 ± 16.2) MeV, respectively. It is worth mentioning that $e^+e^- \to h_c\pi^+\pi^-$ is one of the decay channels investigated inclusively in this analysis. The $Y(4220)$ appears again in multiple decay channels, one of them is $e^+e^- \to \psi(2S)\pi^+\pi^-$. This channel was studied by Belle, BaBar and BESIII [21], $Y(4220)$ along with two other resonant structures, the $Y(4390)$ and the $Y(4660)$, were observed in the energy dependent cross sections. The observations of the $Y(4220)$ and the $Y(4390)$ in the above mentioned decay channels are shown in figure 1.10. The most renowned charmonium-like Y vector state, the $Y(4260)$ is explained in details in the two following subsections.

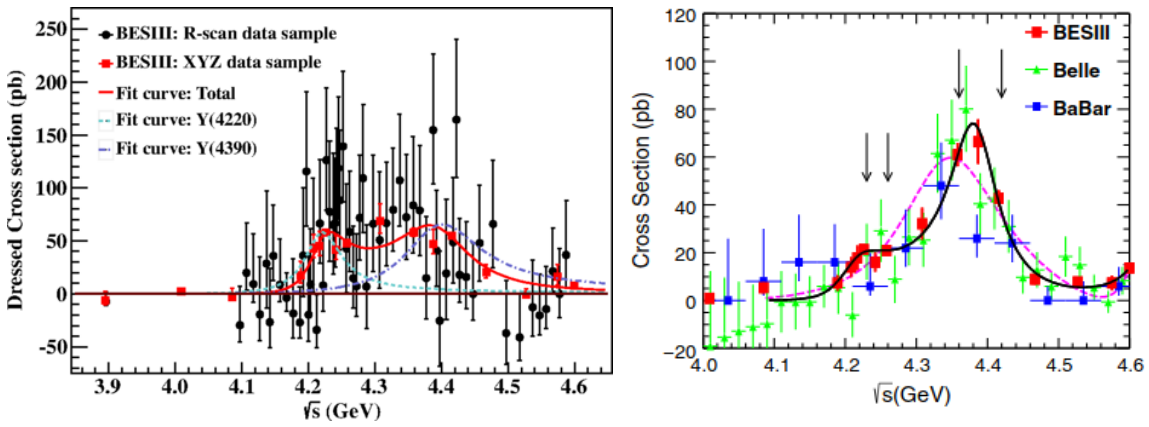

Figure 1.10: Left: The observation of $Y(4220)$ and $Y(4390)$ in the energy dependent cross section of $e^+e^- \to h_c\pi^+\pi^-$ at the BESIII for the XYZ and R-scan data samples [20]. Right: The energy dependent cross section of $e^+e^- \to \psi(2S)\pi^+\pi^-$. The red dots are the results obtained in the BESIII analysis, the green triangles and blue squares are from BELLE and BABAR's analyses, respectively. The black line is a fit to the BESIII data with a coherent sum of three Breit-Wigner functions, describing the $Y(4220)$, $Y(4390)$ and $Y(4660)$, respectively. The arrows mark the locations of four energy points with the largest luminosities [21].

1.5.2 The $Y(4260)$ State

The $Y(4260)$ was discovered in the ISR process $e^+e^- \to J/\psi\pi^-\pi^+$ by BABAR in 2005 [1] as shown in figure 1.11. It was confirmed by Belle in 2007, where an additional structure around 4.008 GeV [22] was observed. This state has a large decay rate to the charmonium state J/ψ with a light meson system. However, it has surprisingly a strong suppression of $D\bar{D}$ decays, even though $Y(4260)$ is only around 300 MeV above the $DD\pi$ threshold.

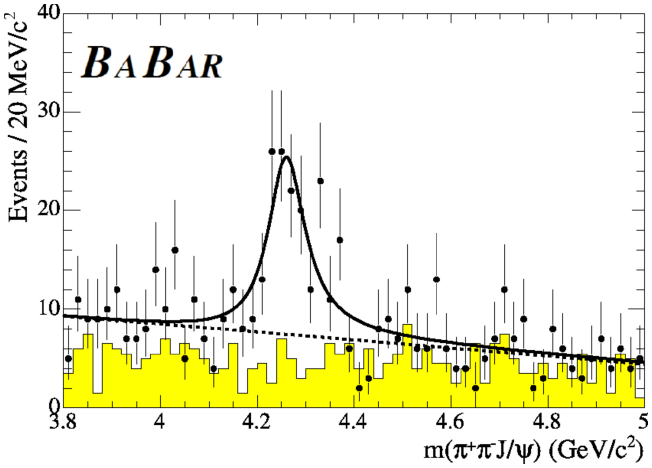

Figure 1.11: The first observation of the $Y(4260)$ in the invariant mass of $\pi^+\pi^- J/\psi$ by BABAR in 2005 [1].

The $Y(4260)$ is very intriguing for many reasons. First, the ratio of the rate of hadron production to that for muon pairs, also known as the R-value.

$$R = \frac{\sigma(e^+e^- \to hadrons)}{\sigma(e^+e^- \to \mu^+\mu^-)}. \tag{1.6}$$

R shows a dip around 4.26 GeV, as seen in Fig 1.12, which implies no resonance or suggests a more complicated interplay of the different apparent resonances in this area.

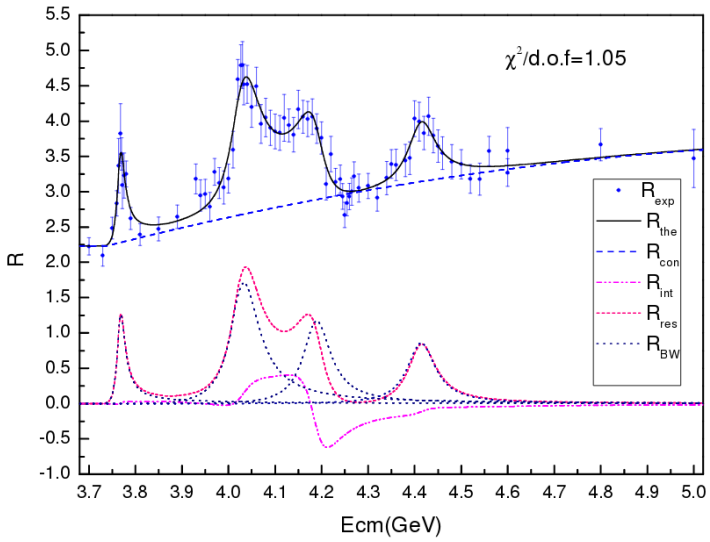

Figure 1.12: The fit to the R-values for the high mass charmonium structure. [23]

Secondly, in attempt to better understand the nature of the $Y(4260)$ state, BESIII investigated $e^+e^- \to J/\psi\pi^+\pi^-$ [24] with much more statistics than the previous studies. Instead of observing one broad structure around 4.26 GeV as observed previously by BABAR, two resonant structures are observed. The first one with a mass of (4222.0 ± 3.4) MeV and width of (44.1 ± 4.7) MeV, and a wider resonance with a mass of (4320.0 ± 13) MeV, width (101 ± 27) MeV and a $J^{PC} = 1^+$.

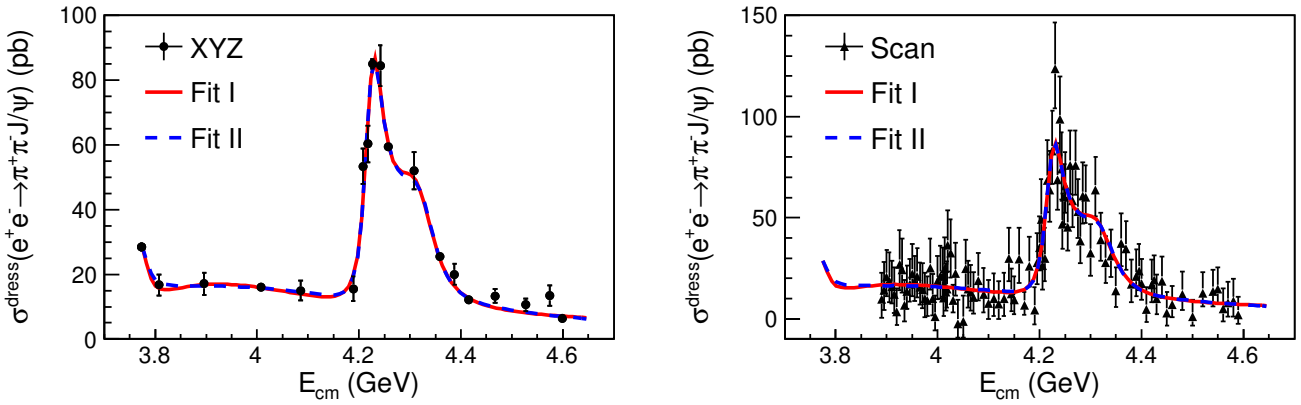

Figure 1.13: Left: The energy dependent cross section of $e^+e^- \to J/\psi\pi^+\pi^-$ for the XYZ data sample at BESIII. Right: The energy dependent cross section of $e^+e^- \to J/\psi\pi^+\pi^-$ for the R-scan data sample at BESIII. [24]

In comparison with the previous average values from 2016 for the $Y(4260)$, the mass of the first resonance is about 30 MeV lower and its width is a factor of 3 narrower. The results of this BESIII study are discussed in details in the analysis results chapter, as $e^+e^- \to J/\psi\pi^+\pi^-$ is one of the main decay channels investigated in this thesis.

Thirdly, the $Y(4260)$ is connected in decays to other intriguing XYZ-charmonium like states. The $Z_c(3900)$ which could be interpreted as a four quark state is observed in the following decay

channel $Y(4260) \rightarrow Z_c(3900)[\rightarrow J/\psi\pi^{\pm}]\pi^{\mp}$. The $X(3872)$ was observed as well at BESIII in $Y(4260) \rightarrow \gamma X(3872)$. This strongly indicates that these three particles share common properties and have a similar internal structure.

1.5.3 Possible Interpretations of the $Y(4260)$

It is very difficult to accommodate the $Y(4260)$ as a conventional charmonium. As shown in Fig 1.8, this state being a spin vector state is far outside the predicted masses of any conventional vector mesons whether it was radial excitations: $\psi(2S), \psi(3S), \psi(4S)$ or D-wave states: $\psi(1^3D_1)$, $\psi(2^3D_1)$, $\psi(3^3D_1)$.
The possibility of $Y(4260)$ being a glueball is very small. The decays of glueballs are expected to be flavor blind. In other words, the $Y(4260)$ should not dominantly decay to $\pi^+\pi^- J/\psi$ but rather decay to multiple light mesons at comparable rates. Also, the $Y(4260)$ is created via initial state radiation and if it was a glueball, this would be impossible since photons do not couple to gluons. Another possible interpretation would be a hadronic molecule. There are multiple open charm thresholds with $J^{PC} = 1^{--}$ below the $Y(4260)$, e.g., $\bar{D}D_1(2420)$, $\bar{D}_s D_{sj}(2317)$, $\bar{D}^* D_1(2420)$. However, $\bar{D}D_1(2420)$ is the only acceptable choice. The others are either far away or too broad to form a hadronic molecule. If the $Y(4260)$ is interpreted as a $\bar{D}D_1(2420)$ molecular state, it would decay as illustrated in figure 1.14 [25]. However, this interpretation is still challenged for one main reason. The width of D_0 and D_1 are as large as 300 MeV, which in turn contradicts the narrow width of the $Y(4260)$.

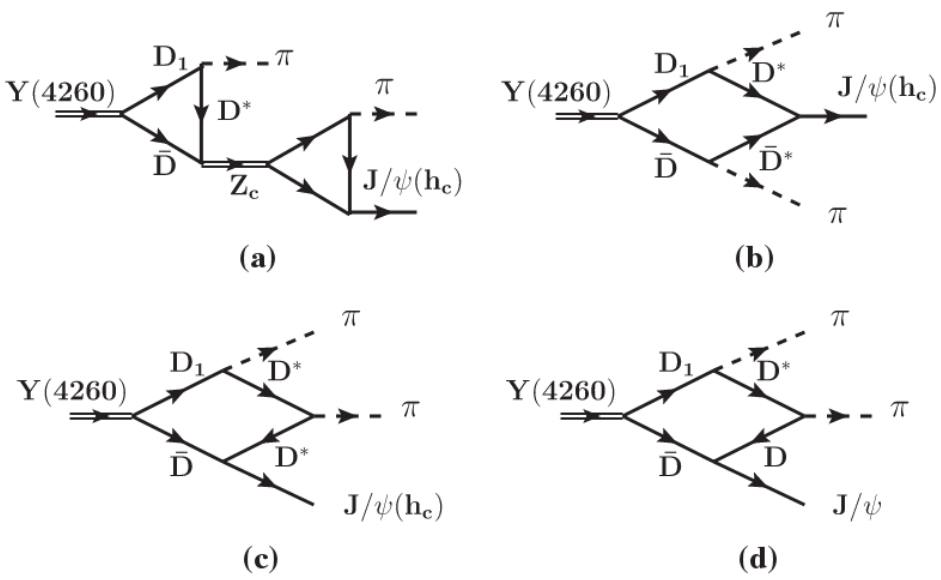

Figure 1.14: The Feynman diagrams fo $Y(4260) \rightarrow \bar{D}D_1 + c.c. \rightarrow J/\psi(h_c)\pi^+\pi^-$[25]

A tetraquark interpretation of the $Y(4260)$ has some interesting aspects. As mentioned in [26], if the $Y(4260)$ is interpreted as a tetraquark with a content of $\frac{1}{\sqrt{2}}(u\bar{u}+d\bar{d})c\bar{c}$, its mass is expected to be between 4.22 and 4.37 GeV, which is covering the experimental value of the $Y(4260)$'s mass.

However, in this scenario, $Y(4260)$ should easily decay to a $D\bar{D}$ finale state. In fact, open charm decays of the $Y(4260)$ shows strong suppression. The observation of an isovector partner $Y'(4260)$ in the decay channel $\pi^0\pi^+\pi^- J/\psi$ could easily confirm the tetraquark hypothesis.
Whether it is a molecular state, a hybrid, a compact tetraquark, or any other exotic configuration, is an ongoing debate among theorists, which is still unclear and undecided. That is one of the reasons why 13 years after the discovery, $Y(4260)$ is still one of the most investigated XYZ states by many experiments.

CHAPTER 2

THE BESIII EXPERIMENT

1 The Physics Goals of the BESIII Experiment

The research program of BESIII [3] covers a wide range of topics including charmonium physics, D-physics, τ physics, light hadron spectroscopy, hadronic fragmentation, R-value measurements and precision tests of the Standard Model.
The BESIII experiment has collected the world largest data sample of J/ψ events ($> 10^{10}$ events) as well as the largest data samples of $\psi(2S)$ ($0.6 \cdot 10^9$ events), $\psi(3770)$ and in the $Y(4260)$ region. This offers the unique opportunity to answer crucial questions that past experiments were not able to answer due to low statistics. The results and activities of BESIII in different sectors and topics are summarized below.

1.1 The Charmonium Meson Sector

BESIII invested a lot of effort in investigating and understanding the XYZ charmonium-like states. The directly accessed vector states $Y(4260)$ and $Y(4360)$ are studied more preciously which led to the ground-breaking discoveries of the four-quark hadrons $Z_c(3900)$ [4], $Z_c(4020)$ [19] and new decay modes of the $X(3872)$. In addition, the decay properties of the J/ψ, $\psi(2S)$ and $\psi(3370)$ could be studied. The total decay widths of J/ψ and $\psi(2S)$ are supposed to be measured with a precision of 1%. Moreover, due to the huge data samples, Cabibbo-suppressed J/ψ decay channels and new physics beyond the standard model could be detected. The analysis performed for this thesis falls in this sector.

1.2 The Light Meson Sector

BESIII searches for the QCD predicted glueballs via J/ψ radiative decays. Charm and anti-charm quarks annihilate into gluons and with the existing 10^{10} J/ψ sample, BESIII is regarded

as the ideal gluon factory. Additionally, lots of studies will focus on understanding properties of certain light scalars with gluonic contents such as $f(1500)$ and $f(1700)$.
The XYZ states are studied as well in the light sector, $X(1835)$ was seen as a near threshold enhancement in the $p\bar{p}$ system by BESII [27] and was confirmed later by BESIII [28] along with two other resonances $X(2120)$ and $X(2370)$ in the $\pi^+\pi^-\eta$ system [29].

1.3 The τ Physics Sector

The study of the hadronic τ decays allows us not only to precisely measure both of the strange quark mass and the CKM matrix element V_{us} but also to search for signs of CP-violation.
Another important measurement to be made is that of the τ mass. It was previously measured at BESI for the first time but with more statistics it can be measured at BESIII with a factor of 3 improvement on the previous result.

1.4 The Open Charm Physics Sector

D-meson pairs are studied at BESIII via $\psi(3370)$ decays while D_s mesons could be produced from e^+e^- annihilation. Through semi-leptonic D-meson decays, theoretical predictions could be tested and the CKM matrix elements V_{cs} and V_{cd} are measured. Furthermore, $D - \bar{D}$ mixing and CP violation will be studied intensively in this sector.

2 The BESIII Detector at BEPCII

The Beijing Electron Positron Collider (BECPII) is a particle accelerator located in Beijing, China, operating since 2009. It is designed to accelerate and collide e^+e^- and it replaced its predecessor (BEPC) which was operating for 12 years. BEPCII (shown in figure 2.1) consists of three main subsystems : The injector LINAC, the storage ring and the Beijing Spectrometer (BESII). The electrons are created through an electron gun system and then some of them are diverted and converted to positrons. The resulting electrons and positrons are symmetrically accelerated in the injector to the storage ring at energies between $1 - 2.3$ GeV. The LINAC which includes the electron gun and positron converter is 202 m long.
The beam is transported through a 210 m transport line from the LINAC to the storage ring (shown in figure 2.2) running in the tau-charm energy region $E_{cm} = 2.0 - 4.63$ GeV with a design luminosity of 10^{33} cm^{-2}s^{-1} [30]. It is composed of two identical rings, each with a circumference of 237.5 m. The beams collide at the south crossing where the BESIII detector is built around the interaction point

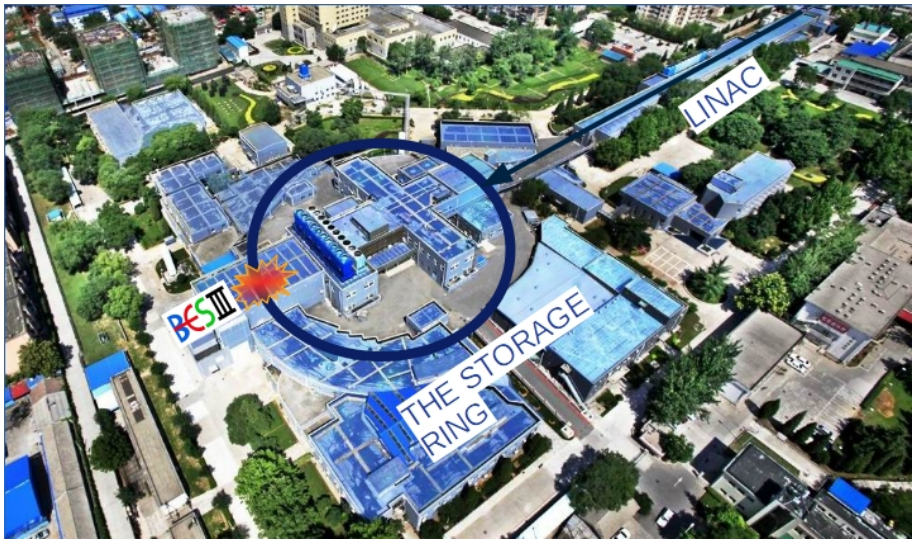

Figure 2.1: Areal view of BEPCII showing the three subsystems : LINAC, the storage ring and the BESIII detector.

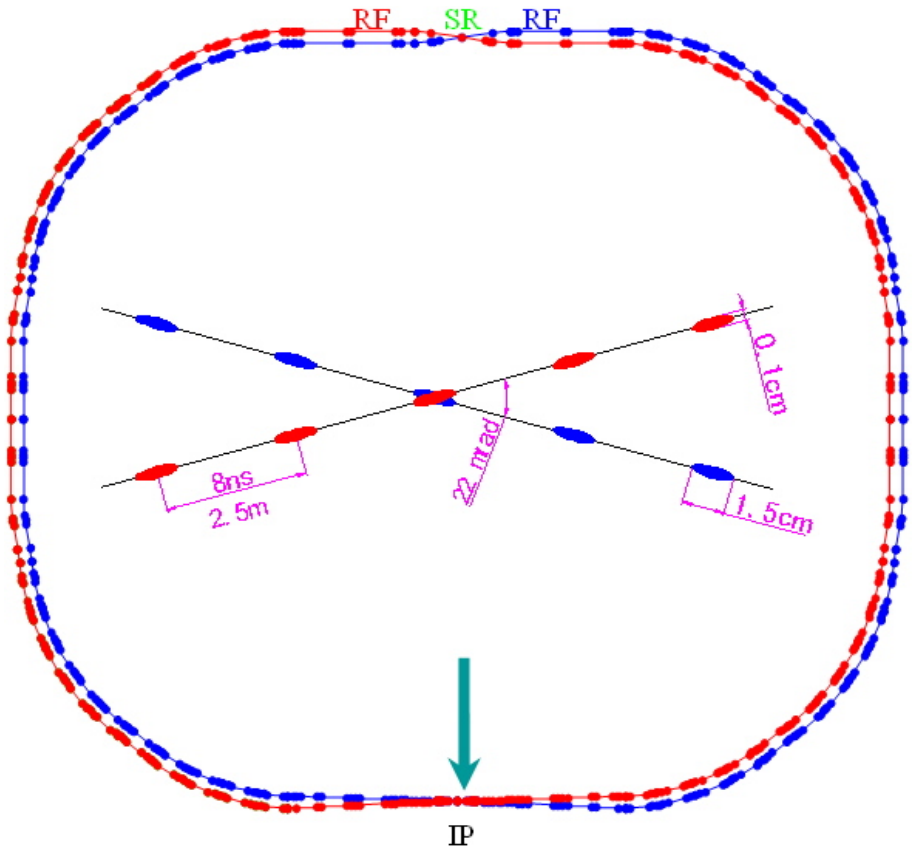

Figure 2.2: Layout of the BEPCII double ring accelerator at IHEP

Table 2.1: Main parameters of the BEPCII collider

Parameter	value
Linac length	220 m
Circumference	237.53 m
Beam Energy	$1.0 - 2.3$ GeV
Peak luminosity	1×10^{33} cm^{-2} s^{-2}
Ratio-frequency amplifier frequency	499.8 MHz
Collision cycle	8 ns
Number of bunch	93
Bunch spacing	2.4 m
Bunch current I_b	9.8 mA
Bunch length σ_1	$<$1.5 cm
Beam current at collisions	910 mA
Beam current in synchrotron radiation	250 mA
Beam lifetime	2.7 hours
Crossing angle	11×2 mrad
(Positron) Electron injection rate	(50)200 mA/min

The Beijing Spectrometer III (BESIII) (shown in figure 2.3) is the only and main detector at BECPII. The BESIII detector is a general purpose detector with an onion-like structure. It is designed to capture both charged and neutral particles with a geometric acceptance of 93% of 4π. This detector is comprised of five sub-detectors with different tasks which will be described in details in the next subsections.

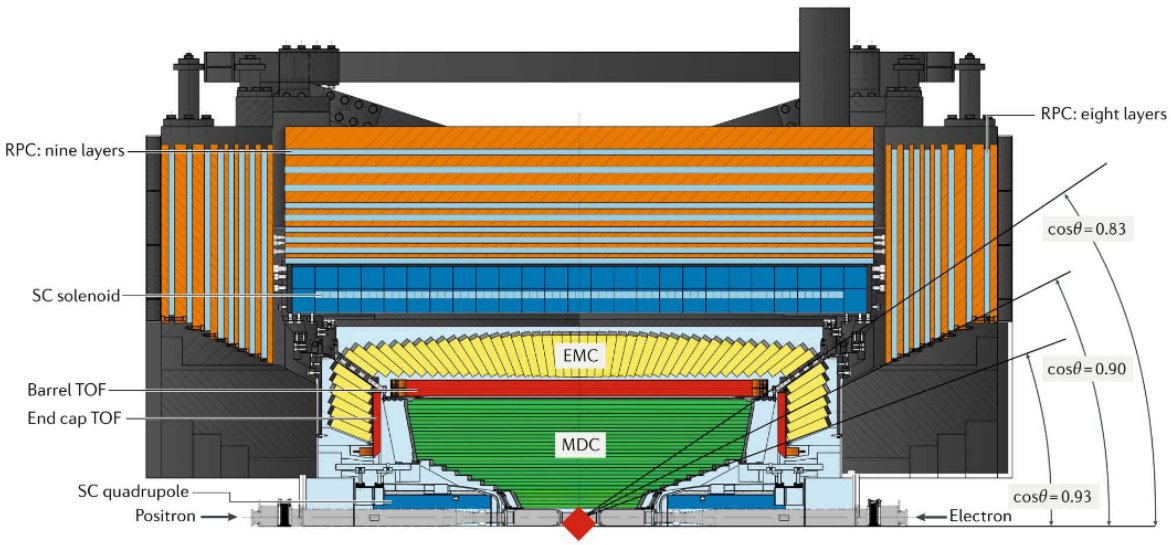

Figure 2.3: A schematic view of the upper half of the BESIII detector

2.1 Multilayer Drift Chamber

The Multilayer Drift Chamber (MDC) shown in figure 2.4 is the closest sub-detector to the interaction point. It measures precisely the momentum of all charged particles by their curvature in the presence of a magnetic field. It can determine the particle's type based on the energy deposit (dE/dx) of passing particles in the chamber as well. The MDC covers the polar angle region where $\cos(\theta) < 0.93$, with an inner radius of 59 mm and outer radius of 810 mm. The chamber is made of 43 layers of drift cells in total. The inner chamber consists of 8 layers, while the remaining 35 layers form the outer chamber. Each drift cell consists of one gold plated tungsten sense wire surrounded by eight thick aluminum field wires. The MDC is filled with a helium based gas mixture (He-C_3H_8 60%:40%). The mixture was chosen to minimize multiple scattering. It will be ionized by the passing of charged particles, then the trail of ionized gas are collected onto field and sense wires. The MDC has a spatial resolution of 135 μm, a transverse momentum resolution of $\delta p/p = 0.5\%$ at 1.0 GeV/c and an energy loss resolution for particles of 6% leading to a 3σ π/K separation up to 0.7 GeV/c [31].

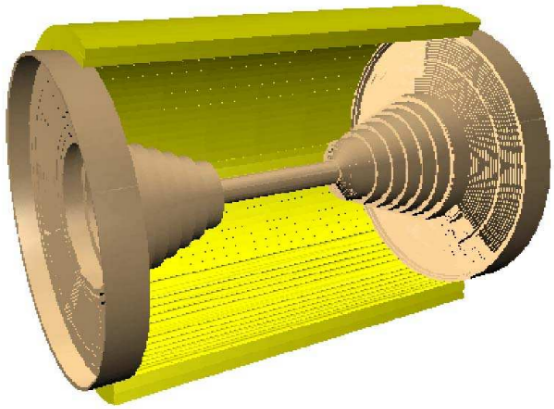

Figure 2.4: An overview of the BESIII Main Drift Chamber

2.2 Time of Flight Detector

The Time-of-Flight sub-detector (ToF) shown in figure 2.5 is located around MDC. It provides particle identification by measuring the flight duration of particles. It consists of two main parts : A barrel with a polar angle coverage of $|\cos\theta| < 0.82$, a radius of 81 to 92.5 cm, a total length of 2.3 m and end caps covering the region where $0.85 < |\cos\theta| < 0.95$.
The ToF system is based on plastic scintillators. In total it consists of 88 scintillators in the barrel and 44 in the end caps. The ionizing passing particles excite molecules in the scintillator, then they emit scintillation light which can be read by the photomultiplier tubes. Timing resolutions of 90 ps in the barrel and 70 ps in the end caps are achieved. This allows a 3σ π/K separation up to momenta of 0.7 GeV/c.

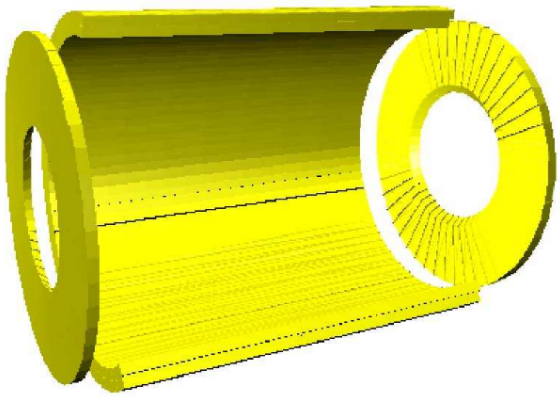

Figure 2.5: The BESIII Time Of Flight System

2.3 Electromagnetic Calorimeter

While charged particles are mainly identified by the MDC, neutral particles do not leave any trace in the latter. Hence, neutral particle identification is mainly achieved by the electromagnetic calorimeter (EMC) where the energy and hit position of photons are preciously measured. The EMC is shown in figure 2.6. Electrons, positrons and photons produce electromagnetic showers that are absorbed in the material after depositing their full energy.
The EMC is located between the ToF and the superconducting solenoid magnet. It consists of 6272 CsI(TI) crystals with a total weight of about 24 tons and an inner radius of 940 mm. The EMC consists of two main components, the barrel part covering $|\cos\theta| < 0.82$ and the two end caps covering $0.83 < |\cos\theta| < 0.93$. In the barrel, there are a total of 44 rings of crystals along the z direction. In each end cap there are 6 rings with 120 crystals, each. The crystal length is 28.5 cm and is read out by two photo diodes. The energy resolution of the EMC is $\sigma_e/E = 2.5\%$ at 1 GeV and the position resolution for showers is 0.6 cm/$\sqrt{E}[GeV]$.

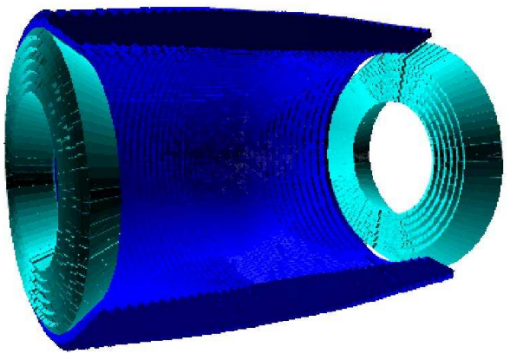

Figure 2.6: The BESIII Electromagnetic Calorimeter

2.4 Superconducting Solenoid Magnet

The Superconducting Solenoid Magnet (SSM) provides a uniform axial magnetic field with a strength of 1 Tesla to measure the accurate momentum of particles. Particle momentum is determined from the measured curvature of these tracks in the field. The solenoid has a mean radius of 1.482 m and a length of 3.52 m. [31]

2.5 Muon System

Muons are highly energetic minimally ionizing particles. After passing all of the previous sub-detectors almost undisturbed, they cross all the layers of the muon chamber leaving hits in each of its layers. The main goal of the muon system is to discriminate between muons and hadrons based on their hit patterns in the detector.
The muon system is a gaseous detector ($Ar/C_2F_4H_2/C_4H_{10}$ 50%:42%:8%) based on Resistive Plates Chambers (RCPs). Just like the previous sub-detectors, the muon chamber consists of two parts. The barrel part ($|cos\theta| < 0.75$) consists of 9 resistive plate layers and the end caps ($0.75 < |cos\theta| < 0.89$) consisting of 8 RPC layers each. The total amount of RPC units is 978 covering an area up to 1272 m^2.

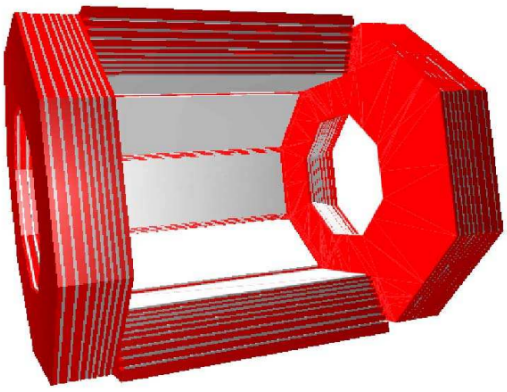

Figure 2.7: The BESIII Muon System

2.6 Trigger System

The aim of the trigger system is to select the interesting physics events while suppressing background events efficiently. The BESIII data acquisition (DAQ) is responsible for data collection, filtering, event building and recording. DAQ is designed for a maximum throughput of 4000 good events per second (4000 Hz). The trigger system must therefore reduce the rate of various backgrounds and bhabha events down to 2000 Hz while keeping high efficiency of the signal decays. As seen in table 2.2, the estimated trigger efficiencies of different J/ψ decays are well above 90%, while the background efficiency is reduced to 10%. The BESIII trigger system is staged in a two level scheme, level-1 (L1) for hardware trigger and level-3 (L3)for software event filter. The signals

from different sub-detectors are split into two data streams, one is digitized and stored in the pipeline buffer in front-end electronics (FEE), the other is used in the level-1 hardware trigger to be processed to make a trigger decision. The results of (L3) trigger are ultimately saved on disk. The data can be later analyzed using the reconstruction software.

Table 2.2: Estimated trigger efficiencies for different types of events.

Events	Number of events simulated	Efficiency (%)
$J/\psi \to e^+e^-$	50000	100
$J/\psi \to \mu^+\mu^-$	50000	99.9
$J/\psi \to$ Anything	10000	97.7
$\psi' \to$ Anything	10000	99.5
$\psi'' \to D\bar{D}$ Anything	10000	99.9
$J/\psi \to \omega\eta \to 5\gamma$	10000	97.9
$J/\psi \to \gamma\eta \to 3\gamma$	10000	92.8
$J/\psi \to K^+K^-\pi^0$	10000	97.4
$J/\psi \to \pi^0 p\bar{p}$	10000	97.9
$J/\psi \to \pi^0 p\bar{p}$	10000	95.8
Beam background	1000000	0.005
Cosmic-ray background	100000	9.4

3 The BESIII Offline Software System

The BESIII Offline Software System (BOSS) [32] is developed using the C++ language and object-oriented techniques. It is used for offline data analysis and MC simulations. The software utilizes some external HEP libraries (ROOT, Geant4, CERNLib) and also re-utilizes parts of code from other experiments (ATLAS, Belle, BABAR and GLAST) [33]. The geometry of the detector is described in the geometry design markup language (GDML). The raw data can be reconstructed and converted to ROOT files for further analysis by the data summary tape (DST) Service. The simulation of the BESIII detector is based on GEANT4 [34]. The KKMC [35] or CONEXC [36] generators are used to simulate $c\bar{c}$ production via e^+e^- annihilation with initial state radiation (ISR) effects as illustrated in figure 2.8. The BesEvtGen [37] generator which is based on the EvtGen [38] designed by the B-physics experiments is used to simulate the subsequent charmonium meson decays.

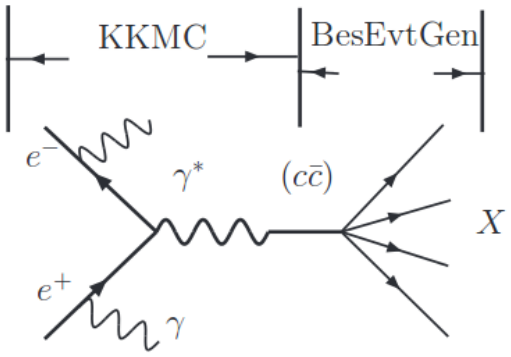

Figure 2.8: Illustration of the BESIII events generator framework.

CHAPTER 3

ANALYSIS OVERVIEW

1 The Missing Mass Technique

The missing mass technique has been used by various experiments in the last two decades and it led to many new interesting results. It can be applied in some cases, when the full reconstruction of the final state is not possible. One of the most renowned discoveries was made in 2013 by the BELLE collaboration when they were able to observe for the first time the singlet P states of bottonium $h_b(1P)$ and $h_b(2P)$ in the spectrum of the missing mass recoiling against two pions [39], see figure 3.1.

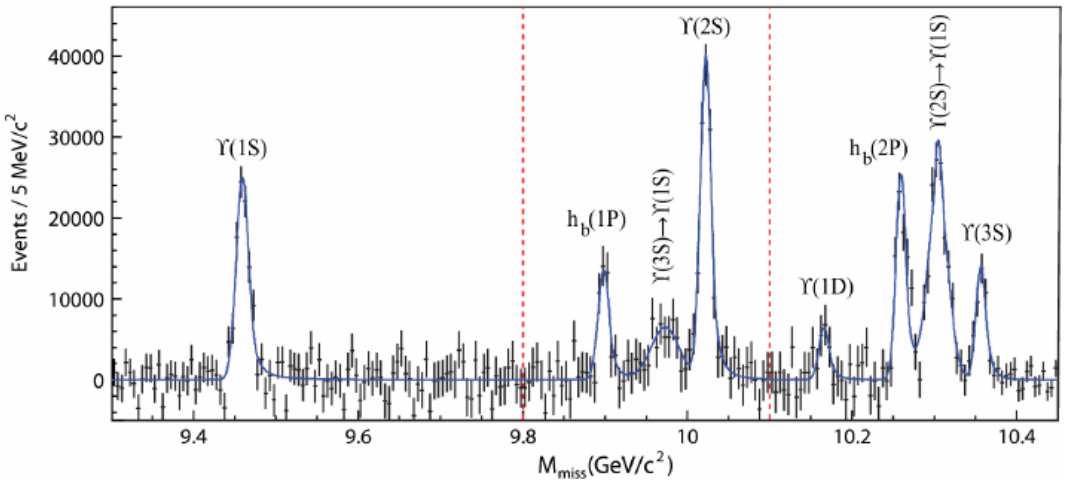

Figure 3.1: The background subtracted missing mass spectrum. The vertical lines indicate boundaries of the fit regions. The overlaid smooth curve is the resulting fit function [39].

In another inclusive study, Belle reported the observation of a new charmonium-like state, the X(3940) produced in the process $e^+e^- \to J/\psi X(3940)$ [40], where $X(3940)$ along with other conventional charmonium states have been observed in the missing mass recoiling against a J/ψ, see figure 3.2.

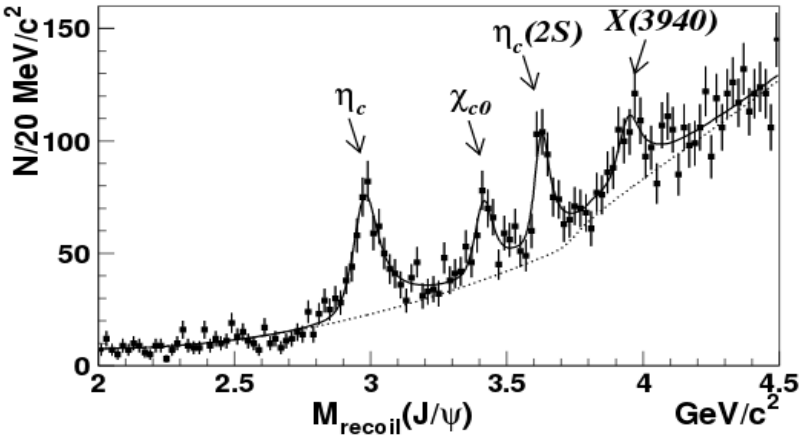

Figure 3.2: The missing mass distribution recoiling against the reconstructed J/ψ in inclusive $e^+e^- \to J/\psi X$ events, where the X(3940) has been observed in the Belle data [40].

The Belle results are partly a great motivation for this thesis. While the Belle study shown in figure 3.1 targeted the bottonium region, we would be able to use the BESIII data samples to explore the charmonium region through an inclusive approach. We assume the following process in order to describe the missing mass technique

$$e^+e^- \to Y \to RX_{c\bar{c}}, \tag{3.1}$$

where Y stands for a charmonium-like state, such as the $Y(4260)$ or $Y(4360)$ and $X_{c\bar{c}}$ stands for conventional charmonium states for example, $J/\psi, h_c$ or $\psi(2S)$. Typically, R is a system of light hadrons such as $(\pi\pi), (KK), (\eta\eta), \pi$, etc. The Feymann diagram of this process is shown in figure 3.3.

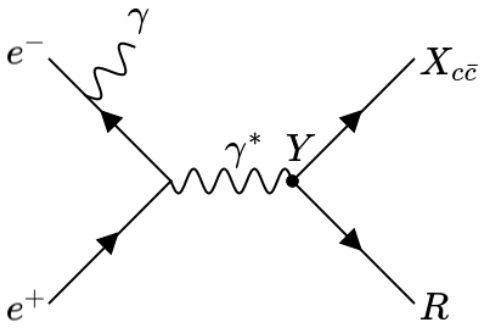

Figure 3.3: The Feymann diagram of $e^+e^- \to Y \to RX_{c\bar{c}}$ at BESIII

We acquire the missing mass recoiling against the recoil system R, by using the 4-momentum of the recoils P_R and the initial e^+e^- pair 4-momentum P_{beam}.
If both P_R and P_{beam} are known, $P_{X_{c\bar{c}}}$ the missing 4-momentum representing the $X_{c\bar{c}}$ can be written

as:

$$P_{X_{c\bar{c}}} = P_{beam} - P_R. \tag{3.2}$$

Therefore the missing mass is given by:

$$M_{X_{c\bar{c}}} = \sqrt{(P_{beam} - P_R)^2}. \tag{3.3}$$

The signals should appear as peaks in the missing mass distribution recoiling against the recoil system R over a smooth background. To better grasp the idea of the missing mass technique, multiple charmonium decay channels were simulated for roughly 30000 events each using the BESIII event generators. The simulated missing mass spectrum recoiling against the $(\pi^+\pi^-)$ system is illustrated in figure 3.4 .

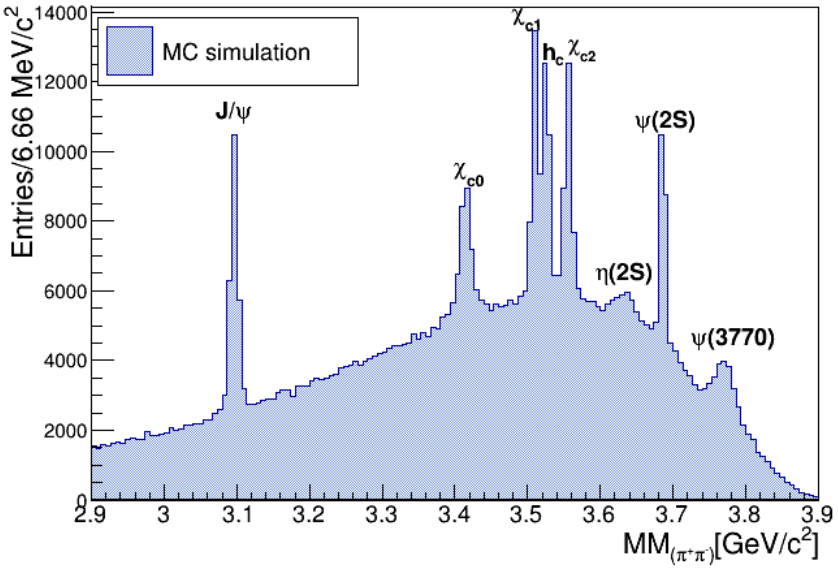

Figure 3.4: Monte-Carlo simulation at BESIII of the missing mass spectrum recoiling against $(\pi^+\pi^-)$ at $E_{CM} = 4.23$ GeV

Every peak in this distribution represents a charmonium state. If we take for example the first peak appearing around 3.1 GeV, it represents the events where the decay channel $e^+e^- \to J/\psi\pi^+\pi^-$ occurred. It is important to point out that the simulations did not include any background decay channels. When applying the method to the BESIII data samples, we expect to see a greater amount of background and only some of these peaks appearing on top of it.
Since our main goal in this work is to investigate the $Y(4260)$ and its decays, we chose recoil systems that allow us to study both, the observed and non-observed $Y(4260)$ decays mentioned by the PDG [41]. Hence, we limited our choice for the following recoiling systems: $\pi^+\pi^-$, K^+K^- and $K^\pm\pi^\mp$.

Even though the exclusive reconstruction approach is used more often in experimental particle physics, inclusive analyses are known to have some advantages. If we take for example the decay channel $e^+e^- \to J/\psi\pi^+\pi^-$, in an exclusive analysis the J/ψ would usually be reconstructed from

two leptons (e^+e^-, $\mu^+\mu^-$) with a branching ratio of 12%. In an inclusive analysis using the missing mass technique, we are able to observe the J/ψ in the missing mass recoiling against the charged pions system from all possible decay channels and without the loss in efficiency by the acceptance for those leptons. Therefore we not only get more statistics with the inclusive approach, but we also avoid the branching ratio and kinematic fit related systematic uncertainties that arise usually in an exclusive analysis. Most importantly, the missing mass technique has a strong discovery potential. An inclusive analysis could target more than one decay channel and end up with new discoveries as many studies showed. The largest drawback is the large background statistics, which cannot be reduced as much as in the case of an exclusive analysis.

2 Measuring e^+e^- Cross Sections and Resonances

In particle physics, cross sections are measured to determine the probability that a specific process will take place in particle collisions. The greater the cross section is, the more likely it is for a process to occur. The cross section is a function depending on the total energy of the reaction. Usually, if one peak appears in the energy dependent cross section, this could be an evidence of a particle that is produced as an intermediate state in the collision, also known as a resonance. Resonance particles are extremely short lived subatomic particles with a lifetime of the order of 10^{-23} s. Due to their short lifetime, they do not leave any traces in the detector. So the best way to measure a resonance is indirectly via measuring its decay products. The decay of a resonance is statistically described by an exponential law

$$|\psi(t)|^2 = |\psi(0)^2|e^{-\Gamma t}, \tag{3.4}$$

where $\tau = 1/\Gamma$ is called the lifetime of the state. Thus, the time dependence of $\psi(t)$ for an unstable state must include the decay factor $\Gamma/2$

$$|\psi(t)|^2 = e^{-iMt}e^{-\Gamma t/2}. \tag{3.5}$$

Under the condition that the width of the intermediate state is not too large ($\Gamma << M$), the cross-section for the process is given by the Breit-Wigner formula.

$$\sigma = \frac{\pi}{k^2}\frac{\Gamma_i\Gamma_f}{(E-M)^2+\Gamma^2/4}, \tag{3.6}$$

Where Γ_i and Γ_f are the partial widths of the resonance decaying to the initial and the final states respectively. Γ is the full width at half maximum of the resonance. E is the center of mass energy. M is the rest mass energy of the resonance and k is the wave number of the incoming projectile in the center of mass frame.

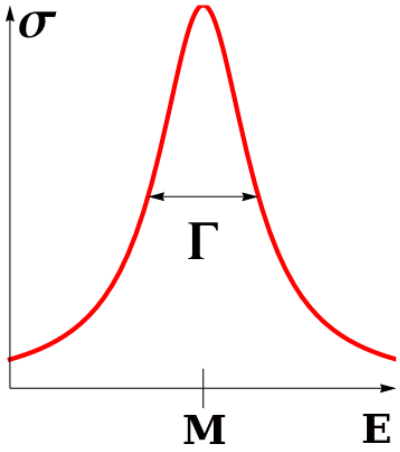

Figure 3.5: A resonance line shape described by a Breit-Wigner

It is demonstrated in figure 3.5 that the cross section has a sharp peak for energies near the rest mass energy M of the resonance. The longer resonances live, the smaller width Γ and hence sharper peaks, they have. So basically by measuring the energy dependent cross section for a specific decay channel, an intermediate state contributing to the decay might be observed. Most importantly, the parameters of the resonance (mass and lifetime) can be precisely measured.

2.1 Experimental Cross Section

Experimentally at BESIII, particles and decay channels are reconstructed in discrete time slices called events. The total number of events in a period of time for a certain decay channel (N_S) is proportional to the cross section (σ) and the integrated luminosity (L_{in}). The observed cross section is given by:

$$\sigma_{Obs} = \frac{N_S}{L_{in}}. \tag{3.7}$$

The integrated luminosity is calculated using the luminosity of a given accelerator (L) which depends on the properties of the beam.

$$L_{int} = \int L dt, \tag{3.8}$$

where L is given by:

$$L = \frac{N_1 N_2 f}{4\pi\sigma_x\sigma_y}, \tag{3.9}$$

N_1,N_2 are the number of particles per bunch. σ_x, σ_y are the spatial dimensions of the bunch and f is the frequency of bunch collisions of the accelerator.
In e^+e^- annihilations, initial state radiation (ISR) may occur, radiating photons before e^+e^- collisions. To deal with the energy loss caused by the ISR effect, the observed cross section is corrected by a correction factor $(1 + f_{ISR})$. The cross section is corrected as well for vacuum polarization effects $(1 + f_{VP})$. Vacuum polarization refers to the process where a virtual electron-positron pair produced by a background electromagnetic field changes the distribution of charges

and currents that generated the original electromagnetic field. If the decay involves intermediate states, then the branching ratio Br_i of their decays must be taken into consideration. The Born cross section is given by:

$$\sigma_{Born} = \frac{N_S}{L\epsilon(1+f_{ISR})(1+f_{VP})\Pi Br_i}. \tag{3.10}$$

The reconstruction efficiency ϵ and the correction factors $(1+f_{ISR}), (1+f_{VP})$ are estimated with the signal Monte-Carlo, which is discussed in subsection 4.1.

3 The BESIII Data-sets

This analysis is based on 27 data samples at center of mass energies between 4.13 and 4.6 GeV collected by the BESIII experiment. Each data sample is characterized by two attributes. The first one is the integrated luminosity which classifies the amount of data collected during a specific time in the experiment. The second attribute is the center of mass energy of the collision to which the data was collected. All the data samples used in this analysis belong to the so called "XYZ data", a high luminosity data-sets containing more than 40 pb^{-1} at each center of mass energy and collected specially with the aim to investigate the XYZ states. These energy points are listed along with their corresponding luminosities in table 3.1 and are shown in figure 3.6. The majority of data-sets (20 out 27) have luminosities above 400 pb^{-1} which could be very beneficial when using the missing mass technique. This analysis was performed within the BOSS framework version 7.04, which was explained in chapter 2.

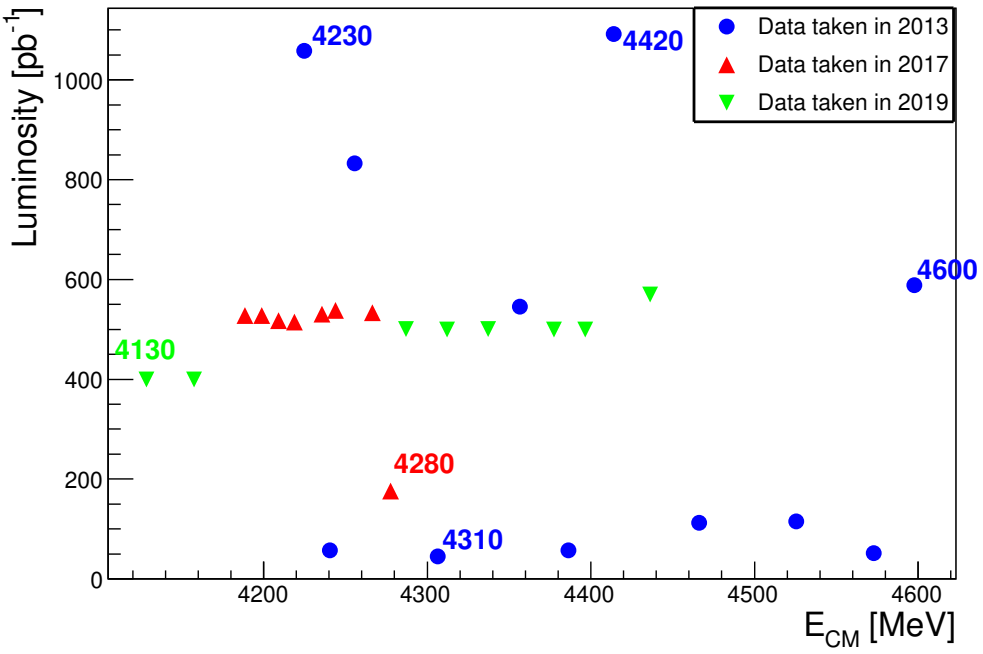

Figure 3.6: The luminosities of the 27 XYZ BESIII data samples used in this analysis. The green energy points are the latest data-samples collected in 2019. The red energy points are collected in 2017 and the blue ones in 2013.

Table 3.1: The luminosities and center of mass energies of the 27 XYZ BESIII data samples used in this analysis.

DATAset ID	E_{CM} [MeV]	Luminosity [pb^{-1}]
4130	4128.48	400
4160	4157.44	400
4190	4188.8	526.7
4200	4198.9	526.0
4210	4209.2	517.1
4220	4218.7	514.6
4230	4225.54	1091.74
4237	4235.7	530.3
4245	4241.66	55.88
4246	4243.8	538.1
4260	4257.43	825.67
4270	4266.8	531.1
4280	4277.7	175.7
4290	4287.88	500
4310	4307.89	45.08
4315	4312.05	500
4340	4337.39	500
4360	4358.26	539.84
4380	4377.37	500
4390	4387.40	55.57
4400	4396.45	500
4420	4415.58	1043.9
4440	4436.24	570
4470	4467.06	111.09
4530	4527.14	112.12
4575	4574.50	48.93
4600	4599.53	586.9

4 Monte-Carlo Simulations

Monte-Carlo simulation is an essential component of experimental particle physics in all the phases of its life-cycle: the investigation of the physics reach of detector concepts, the design of facilities and detectors, the development and optimization of data reconstruction software and the

data analysis for the production of physics results [42]. In this analysis, Monte-Carlo simulations are used to study and optimize selection criteria and to extract the reconstruction efficiency (ϵ), the vacuum polarization and the initial state radiation correction factors. The states and decays under study have been simulated as signal Monte-Carlo with 30000 events at all 27 energy points using the CONEXC and BesEvtGen event generators. The decay channels simulated in this analysis are listed in table 3.2. All these channels are simulated using the ConExc model, the phase space model "PHSP" is used to simulate the $\bar{D}^0$ decays to $K^+\pi^-$ in the open charm decay channels. In table 3.2, the references of the used initial input cross sections are listed. These simulation inputs are needed to extract the initial state radiation and vacuum polarization factors.

Table 3.2: The decay channels simulated in this analysis for each recoil system along with the simulation settings including the simulation model and the reference for the used initial input cross section.

Recoil System	decay channels	Events simulated	Simulation Model	Input Cross Section
$\pi^+\pi^-$	$J/\psi\pi^+\pi^-$	30000	ConExc	[24]
	$h_c\pi^+\pi^-$	30000	ConExc	[20]
	$\psi(2S)\pi^+\pi^-$	30000	ConExc	[43]
K^+K^-	$J/\psi K^+K^-$	30000	ConExc	[44]
$K^\pm\pi^\mp$	$D^0\bar{D}^0[\to K^+\pi^-]$	30000	ConExc, PHSP	[45]
	$D^{*0}\bar{D}^0[\to K^+\pi^-]$	30000	ConExc, PHSP	[45]

As an example, the Monte-Carlo simulated and fitted missing mass distributions for six decay channels are presented in figure 3.7. The signal parameters are estimated with a maximum-likelihood fit. The fit model is composed of a Gaussian function to describe the signal and a polynomial Chebyshev function of the first or second order for the background. As a result of the fit, the number of the reconstructed signal events is estimated and subsequently, the efficiency (ϵ) is calculated. Under each fitted missing mass distribution, a pull histogram is shown that represents the difference between the fit model curve and the data. Ideally for a successful fit, the pull histogram should fluctuate around zero.

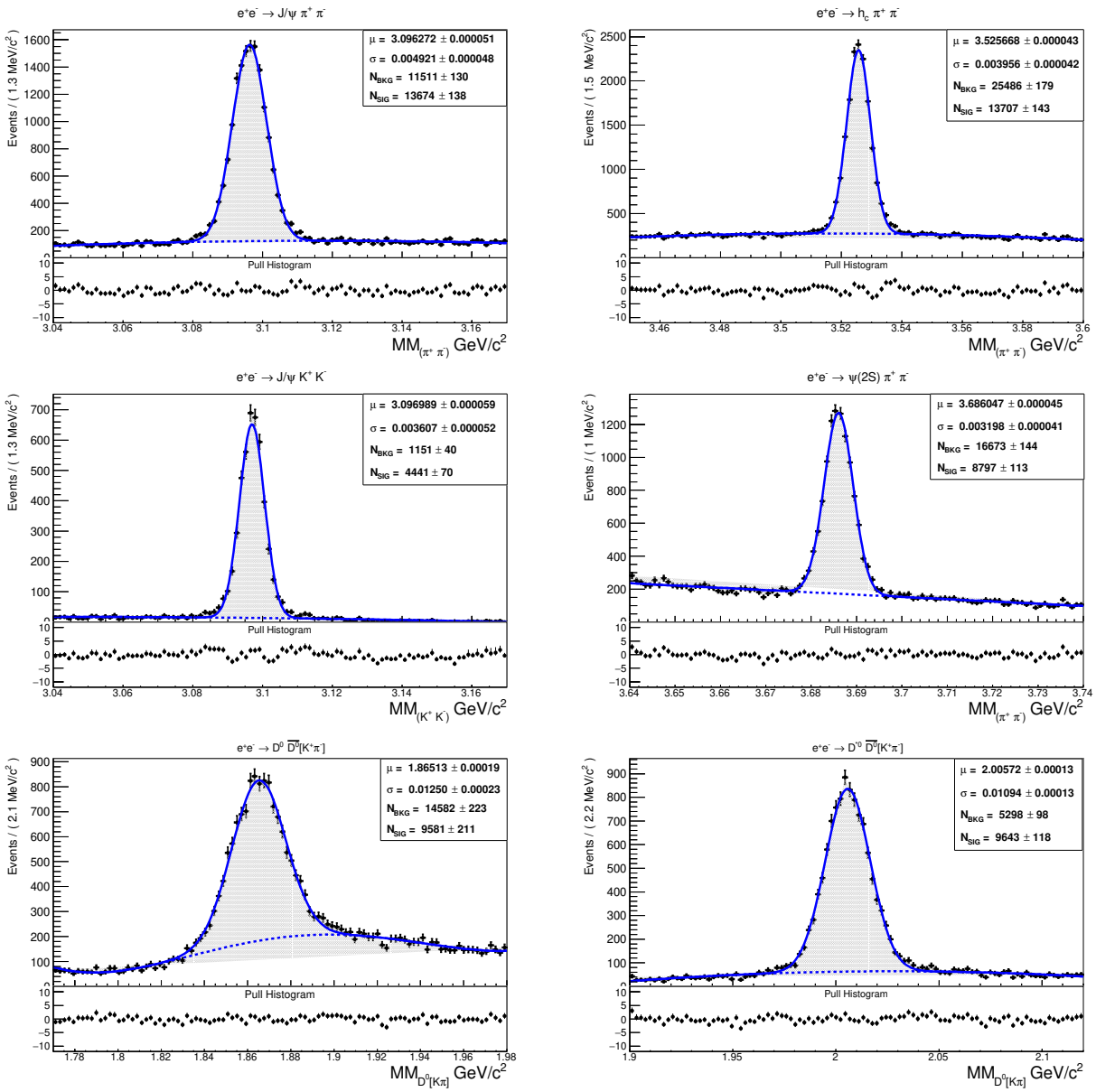

Figure 3.7: The Monte-Carlo simulated missing mass distributions. Top Left: The distribution of $e^+e^- \to J/\psi\pi^+\pi^-$. Top Right: The distribution $e^+e^- \to h_c\pi^+\pi^-$. Middle left: The distribution of $e^+e^- \to J/\psi K^+K^-$. Middle Right: The distribution of $e^+e^- \to \psi(2S)\pi^+\pi^-$. Bottom Right: The distribution of $e^+e^- \to D^0\bar{D}^0$. Bottom Left: The distribution of $e^+e^- \to D^{*0}\bar{D}^0$.

4.1 The ISR & VP Correction Factors

Event generators for e^+e^- scan experiments, such as CONEXC and KKMC, are constructed by taking into consideration the initial sate radiation (ISR). If we take the two following processes of $e^+e^- \to X_i$ and $e^+e^- \to \gamma_{ISR}X_i$, where the photon γ_{ISR} comes from the ISR effects and X_i is a system of hadrons. In CONEXC, the cross section for the ISR process $\sigma(e^+e^- \to \gamma X_i)$ is determined with the relation:

$$\sigma_{e^+e^-\to\gamma X_i}(s) = \int dm \frac{2m}{s} W(s,x) \frac{\sigma_0(m)}{[1+\prod(m)]^2}, \tag{3.11}$$

where σ_0 is the experimental Born cross section of $(e^+e^- \to X_i)$, m is the invariant mass of the final states with $m = \sqrt{s(1-x)}$, and $x = \frac{2E_\gamma}{\sqrt{s}} = 1 - \frac{m^2}{s}$, $\prod(m)$ is the vacuum polarization, which includes contribution from leptons and quarks, and $W(s,x)$ is the so called radiator function [36].

$$W(s,x) = \Delta \cdot \beta x^{\beta-1} - \frac{\beta}{2}(2-x) + \frac{\beta^2}{8}[(2-x)[3\ln(1-x) - 4\ln(x)] - 4\frac{\ln(1-x)}{x} - 6 + x], \quad (3.12)$$

where

$$L = 2\ln\frac{\sqrt{(s)}}{m_e}, \quad (3.13)$$

$$\Delta = 1 + \frac{\alpha}{\pi}(\frac{3}{2}L + \frac{1}{3}\pi^2 - 2) + (\frac{\alpha}{\pi})^2\delta_2, \quad (3.14)$$

$$\delta_2 = (\frac{9}{8} - 2\xi_2)L^2 - (\frac{45}{16} - \frac{11}{2}\xi_2 - 3\xi_3)L - \frac{6}{5}\xi_2^2 - \frac{9}{2}\xi_3, \quad (3.15)$$

$$\beta = \frac{2\alpha}{\pi}(L-1), \xi_2 = 1.64, \xi_3 = 1.20. \quad (3.16)$$

The initial Born cross sections used for the simulation are taken from BESIII and BABAR's measurements. These cross sections are fitted with multi-Gaussian functions and then the fitted results are used as an input in the generator.[36]
Finally, the ISR and VP correction factors are calculated within the generator as follow:

$$(1 + f_{ISR})(1 + f_{VP}) = \frac{\sigma_{e^+e^- \to \gamma X_i}(s)}{\sigma_{Born}} \quad (3.17)$$

For this analysis, table 3.2 shows the references of every initial cross section measurement used for the simulations of different decay channels, e.g. for the $e^+e^- \to J/\psi\pi^+\pi^-$ simulation, the initial input cross section is taken from [24]. Figure 3.8 illustrates the iterative procedure and the stages of the Monte-Carlo simulation and Born cross section calculations.
The detection efficiency and the two correction factors are computed for the six main decay channels of this analysis at every energy point. The energy dependent efficiencies (ϵ) and the corrected efficiencies ($\epsilon(1 + f_{ISR})(1 + f_{VP})$) are shown in figure 3.9.

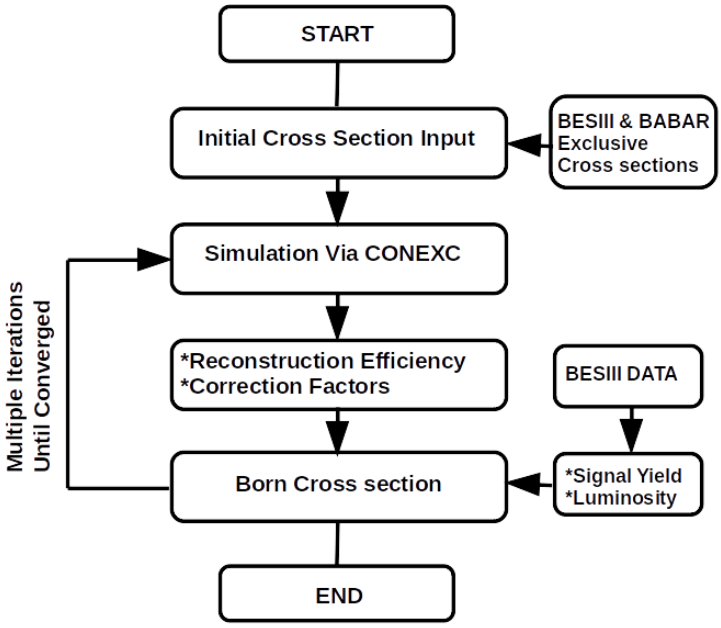

Figure 3.8: Scheme of Born cross section computation

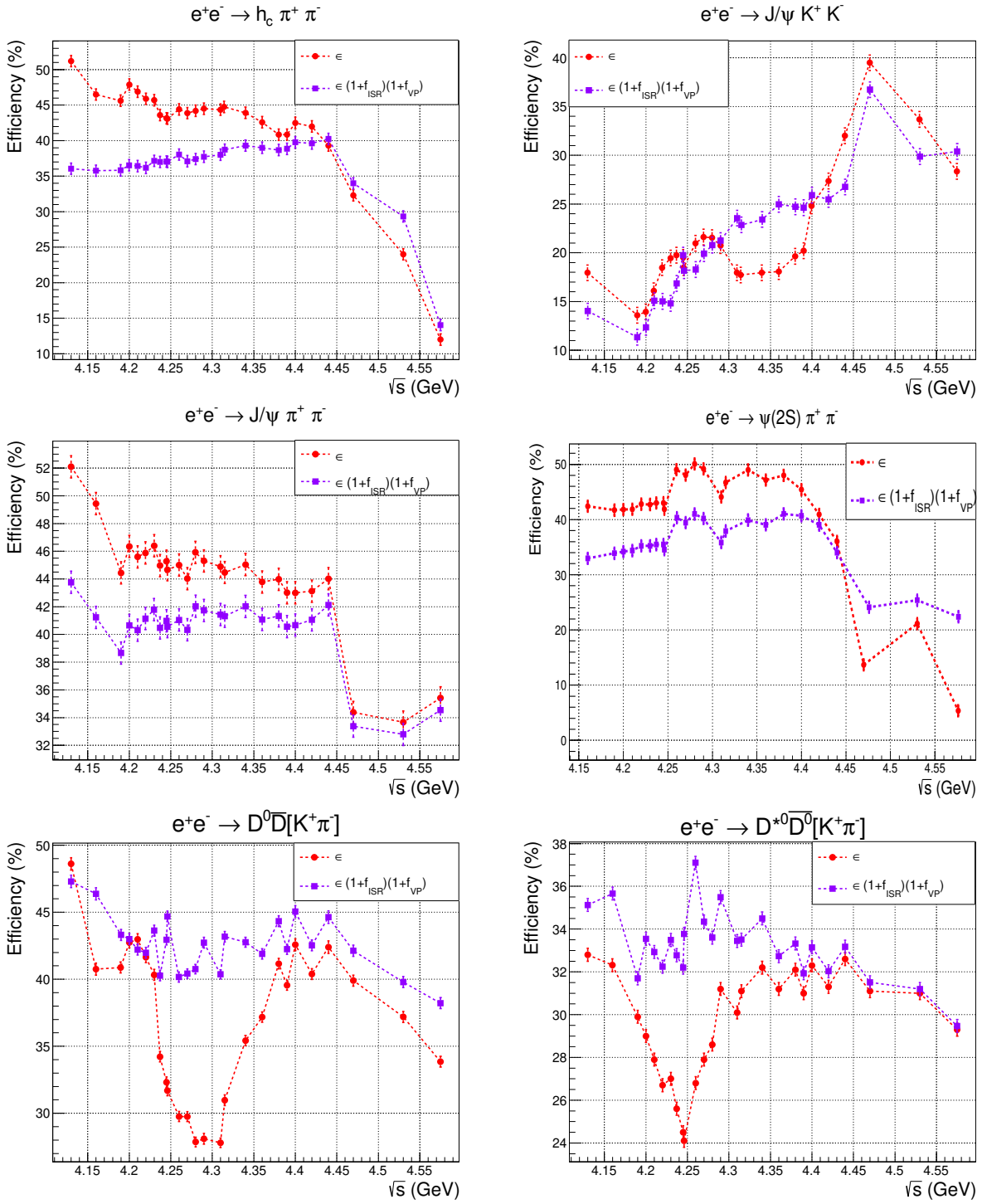

Figure 3.9: The energy dependent efficiencies ϵ in red and the corrected efficiencies $\epsilon(1+f_{ISR})(1+f_{VP})$ in purple. Left: $e^+e^- \to h_c\pi^+\pi^-$, $J/\psi\pi^+\pi^-$, $D^0D^0[\bar{K}^+\pi^-]$. Right: $e^+e^- \to J/\psi K^+K^-$, $\psi(2S)\pi^+\pi^-$ and $D^0D^0[\bar{K}^+\pi^-]$.

5 Event Selection

As mentioned before, one of the advantages of an inclusive analysis is that we do not require as many selection cuts as in an exclusive analysis. The event selection procedure for this analysis consists mainly of the standard BESIII selection cuts, which are presented below.

In an inclusive analysis, the largest background for the $\pi^+\pi^-$ recoil system is coming from the

continuum background, i.e. the process $e^+e^- \to u\bar{u}, d\bar{d}, s\bar{s}$. Event shape variables, in particular the second order Fox-Wolfram moment are used usually in B-factories (e.g. Belle) to suppress the background. The underlying idea is that charmonium or bottonium annihilation generates particles that are uniformly distributed in all the directions, while $q\bar{q}$ events give origin to a two-jet topology, with the final state particles preferentially produced along a symmetry axis (the so-called thrust axis). Unfortunately, cuts on event shape variables are more efficient for higher energies (for which the quarks are strongly boosted) and higher multiplicities. So, they are expected to be less powerful at BESIII's low energies. Due to their inefficiency, event-shape variable cuts will no be used in this analysis. We will focus instead on reducing the combinatorial background.
The selection procedure will be done on multiple stages. First of all, the candidates for good charged tracks are selected from the tracks reconstructed in the MDC. Then good photon candidates are reconstructed from the clusters in the EMC. In the last step, the surviving events are selected using the particle identification criteria (if they contain charged tracks) and veto cuts on invariant masses are applied. The following event selection criteria are applied to both the Monte-Carlo simulation and the BESIII data samples. The variables involved in the different stages of the selections are shown in figures 3.10 to 3.13.

Good Charged Track Selection

- Charged tracks are reconstructed in regions where their angles with respect to the beam direction satisfy $|\cos(\theta)| < 0.93$. The main drift chamber MDC cannot measure tracks outside of this polar angle region at sufficient quality.

- The point of closest approach (POCA) must be within ± 10 cm in the beam direction and within 1 cm in the plane perpendicular to the beam direction. Tracks forming K_s candidates should pass within ± 20 cm.

- Tracks with momenta above 2 GeV/c are rejected in order to suppress the background from Bahaha scattering and pion production without a heavy recoil.

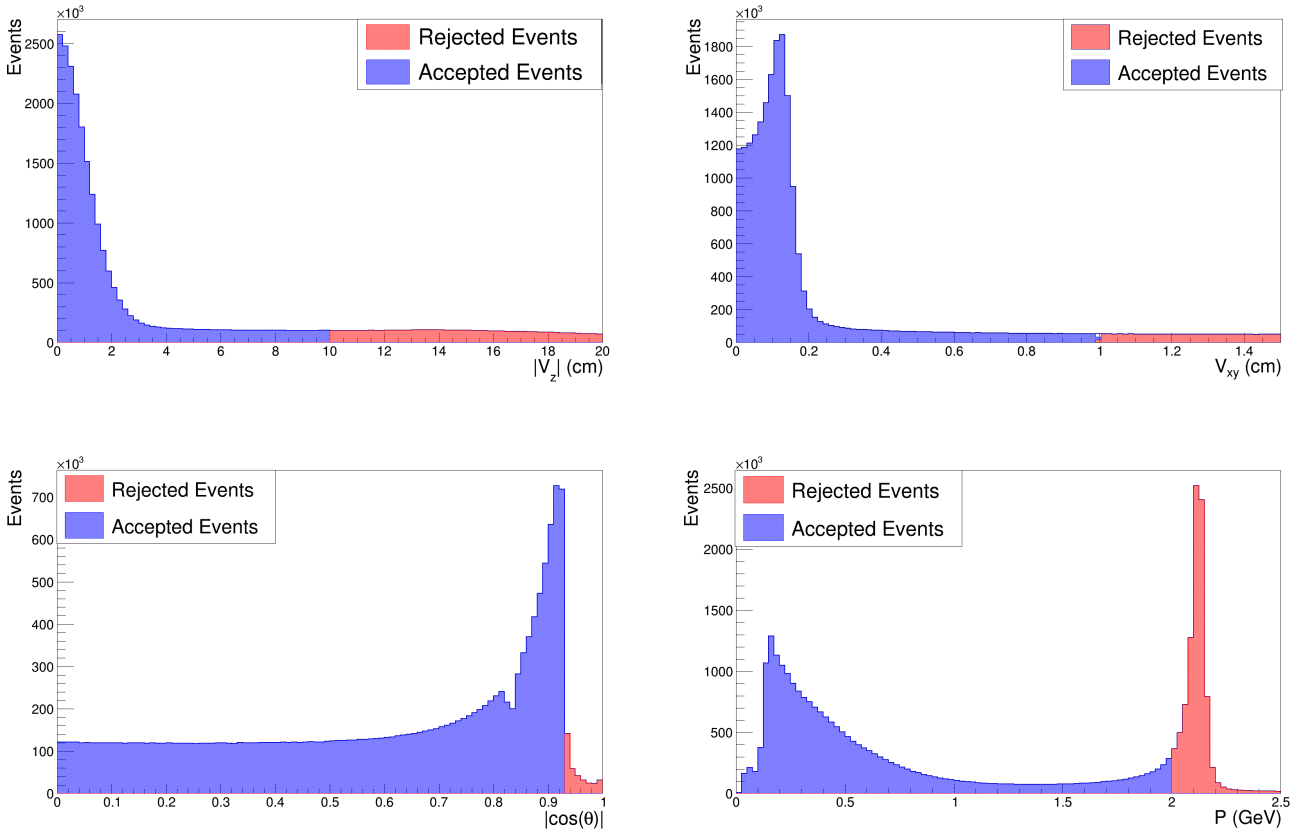

Figure 3.10: Good charged track selection. The rejected events are shown in red while the accepted events are shown in blue. Top Left: POCA V_z. Bottom Left: Cosine of the polar angle. Top Right: POCA V_{xy}. Bottom Right: Momentum.

Good Photon Selection

- The reconstructed energy should be at least $E_\gamma > 25MeV$ in the EMC barrel region defined by $|\cos(\theta)| < 0.8$ and $E_\gamma > 50MeV$ in the EMC end caps defined by $0.84 < |\cos(\theta)| < 0.92$.
- The time difference between the event trigger and the EMC timing information should be 0 ns $\geq t_{EMC} \geq$ 700 ns. It is used to reduce electronic noise and background from unrelated events.
- The angle between neutral clusters and the closest charged track extrapolated to the EMC, refereed to as dAngle, has to be a least 10^o.

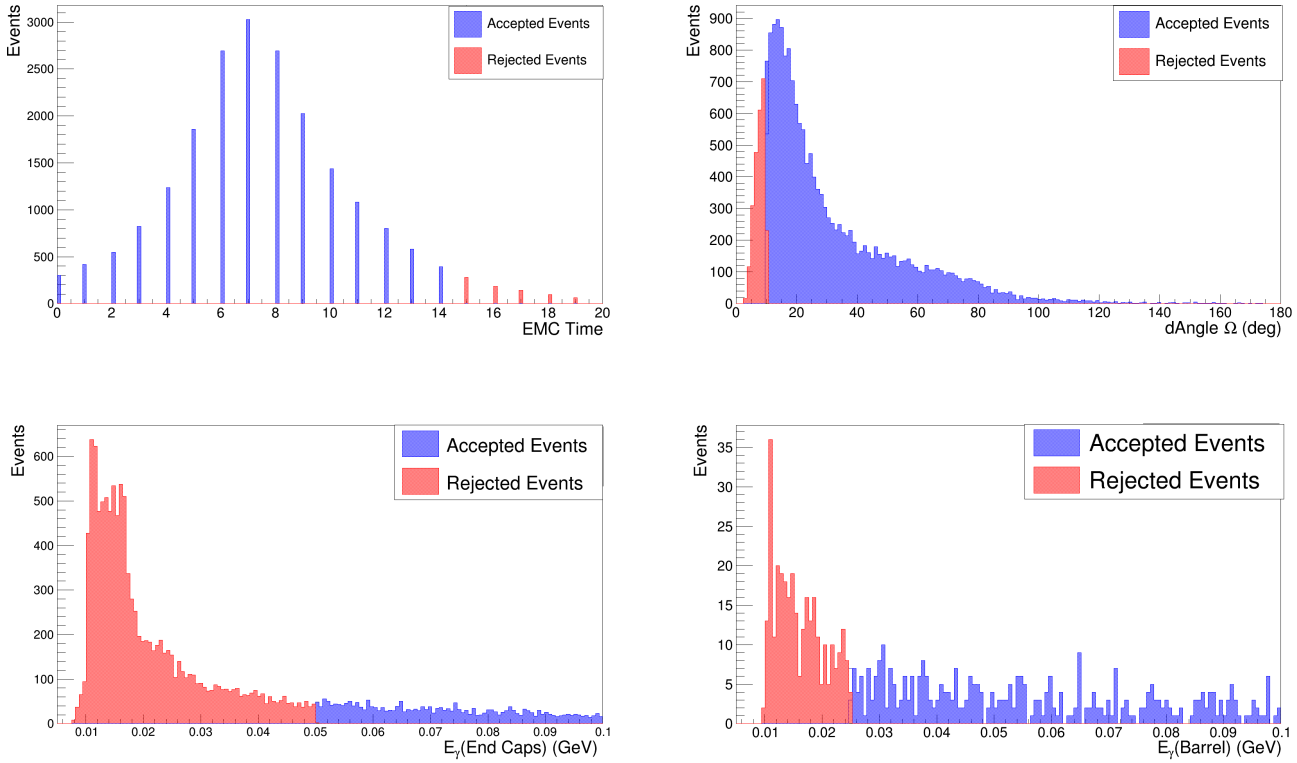

Figure 3.11: Good Photon Selection. The rejected events are shown in red while the accepted events are shown in blue. Top Left: EMC time. Bottom Left: The photon energy deposited in the EMC end caps. Top Right: DAngle Ω. Bottom Right: The photon energy deposited in the EMC barrel.

Particle Identification Selection

- For each reconstructed track, particle identification probabilities PID(π) and PID(K) are calculated based on pion and kaon hypotheses. For pion recoil systems PID(π) of the pions is required to be larger than PID(K) and PID(p). For the charged kaon recoil system, PID(K) is required to be larger than the PID(p) and PID(π).

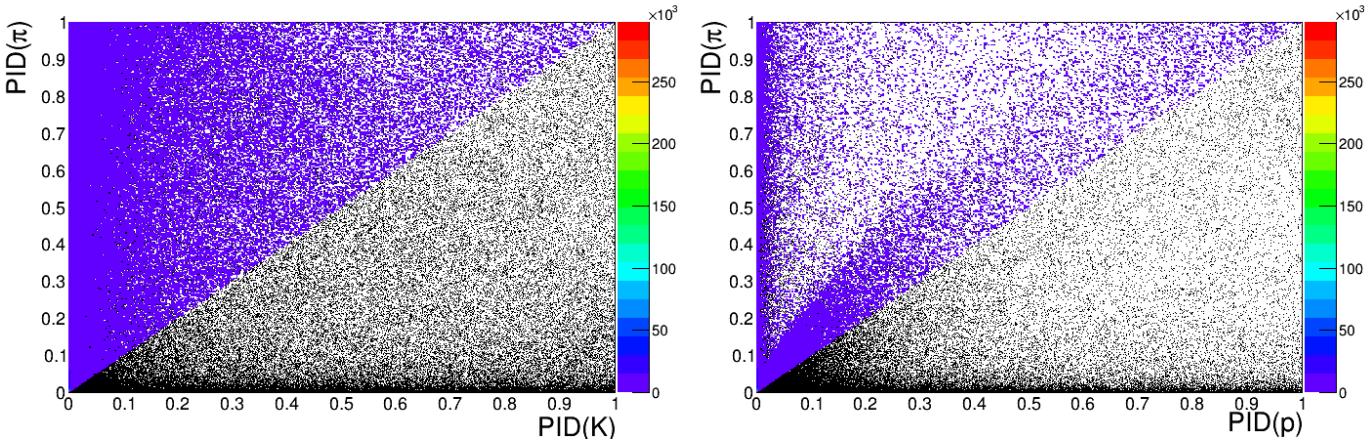

Figure 3.12: Scatter plots of the particle identifications variables for the pions. The colored events are the accepted events. Left: PID($\pi^{\pm}$) Vs PID(K). Right: PID($\pi^{\pm}$) Vs PID(p)

Invariant Mass Selection

- Veto cuts of K_s in the invariant mass of $\pi^+\pi^-$, $\phi(1020)$ and D^0 in the invariant mass of K^+K^-, D^0 in the invariant mass of $K^\pm\pi^\mp$. To reduce the combinatorial background, along side with the BESIII standard cuts a K_s veto is implemented when investigating the following decay channels $e^+e^- \to X_{c\bar{c}}\pi^+\pi^-$ where ($X_{c\bar{c}} = J/\psi, h_c$ and $\psi(2S)$). The main role of this cut is to remove the pions, that combining with another pion, have an invariant mass compatible with the K_s mass. A $\phi(1020)$ and D^0 vetoes are applied when investigating the K^+K^- recoil system. A cut on the invariant mass of $K^\pm\pi^\mp$ in the D^0 region is applied in order to investigate the open charm decay channels.
  Table 3.3 summarizes the different stages of the event selection procedure.

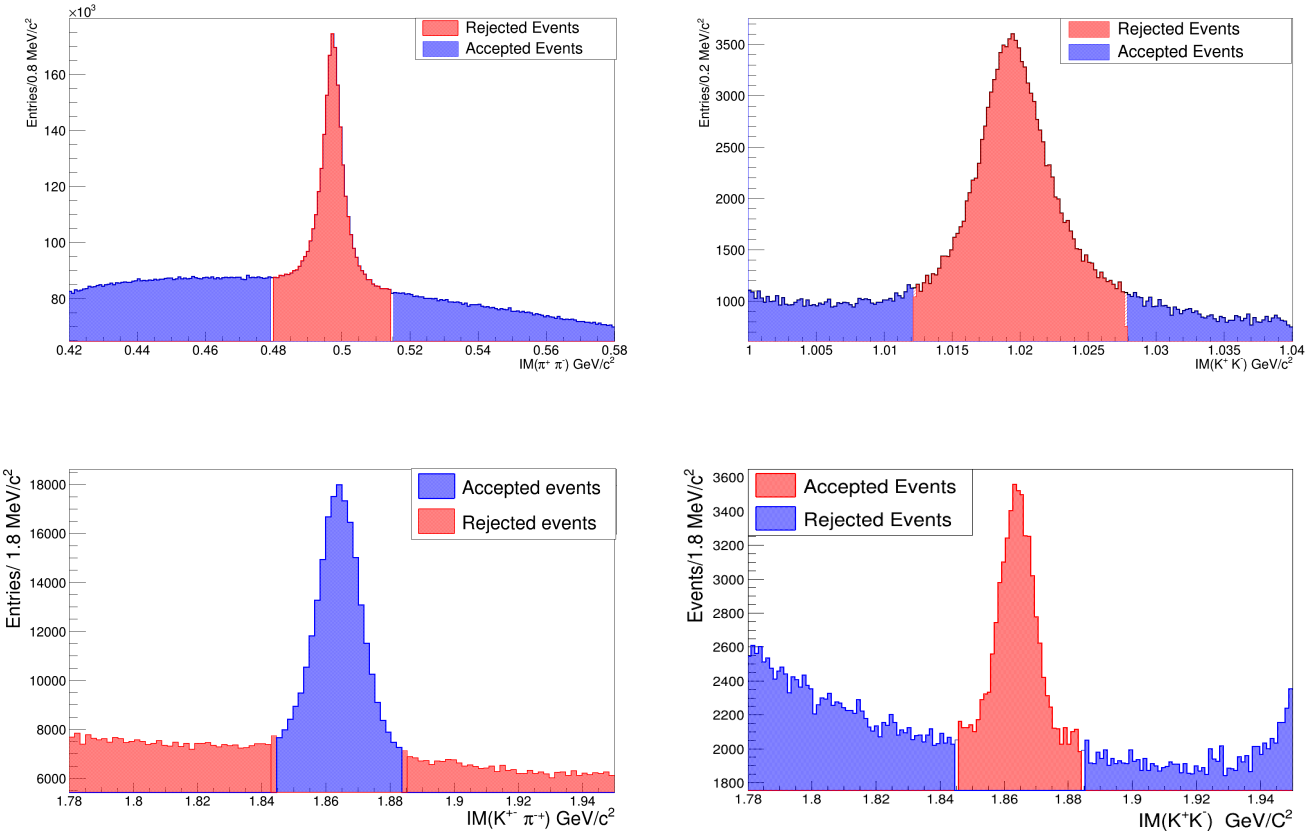

Figure 3.13: The invariant mass distributions cuts. The rejected events are shown in red while the accepted events are shown in blue. Top Left: Veto cut on the invariant mass of K_s candidates. Bottom Left: Veto cut on the invariant mass of $D^0[K^+\pi^-]$ candidates. Top Right: Invariant mass of $\phi(1020)$ candidates. Bottom Right: Invariant mass of $D^0[K^+K^-]$ candidates.

Table 3.3: Summary of the cuts applied for the analyses presented.

Cut	Values
Charged track selection	$\lvert\cos(\theta)\rvert < 0.93$
	$\lvert V_z\rvert < 10$ cm & $\lvert V_{xy}\rvert < 1$ cm
Photon selection	Barrel: $E_\gamma > 25$ MeV
	End caps: $E_\gamma > 50$ MeV
	0 ns <EMC time< 700 ns
	dAngle $\Omega \geq 10^0$
PID selection	For $\pi^\pm$: PID($\pi^\pm$)>PID($K^\pm$) & PID($\pi^\pm$)>PID(p)
	For $K^\pm$: PID($K^\pm$)>PID($\pi^\pm$) & PID($K^\pm$)>PID(p)
Invariant masses selection	
For the ($\pi^+\pi^-$) system	Veto of K_s in IM($\pi^+\pi^-$)
For the (K^+K^-) system	Veto of $\phi(1020)$ and D^0 in IM(K^+K^-)
For the ($K^\pm\pi^\mp$) system	$1.84 <$ IM($K^\pm\pi^\mp$) < 1.885 GeV/c^2.

CHAPTER 4

ANALYSIS RESULTS

1 Analysis of $e^+e^- \to X_{c\bar{c}}\pi^+\pi^-$

Using the event selection described in the previous section, the BESIII XYZ data samples are analyzed. The missing mass distributions for the 4230 and 4360 data samples are shown in figures 4.1 and 4.2. The distributions and fits for additional data samples are shown in the appendix. As described earlier, the signals appear as bumps on top of a huge amount of background. The vertical red lines represent the mass regions of J/ψ, h_c and $\psi(2S)$ respectively. The Gaussian fits of each region are shown separately on the next page. The observations of these three conventional charmonium states are different for each energy point, e.g., at 4.23 GeV, the J/ψ and h_c peaks are clearly visible and there is no observation of the $\psi(2S)$. That is in contrast to the 4.36 GeV mass distribution, where the $\psi(2S)$ appears strongly in the third mass region and the J/ψ barely appears as a small bump in the first region.

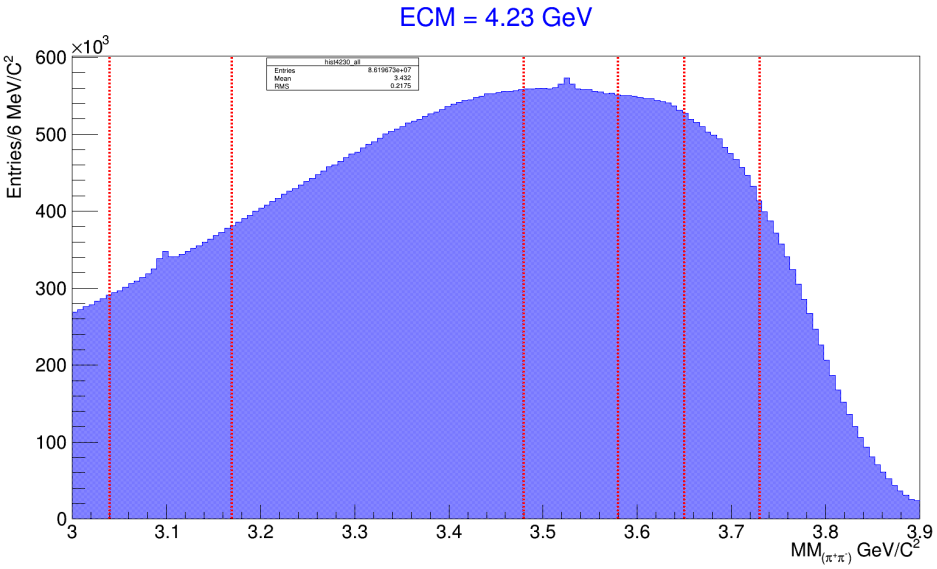

Figure 4.1: The missing mass spectrum recoiling against $\pi^+\pi^-$ for the BESIII 4230 data sample.

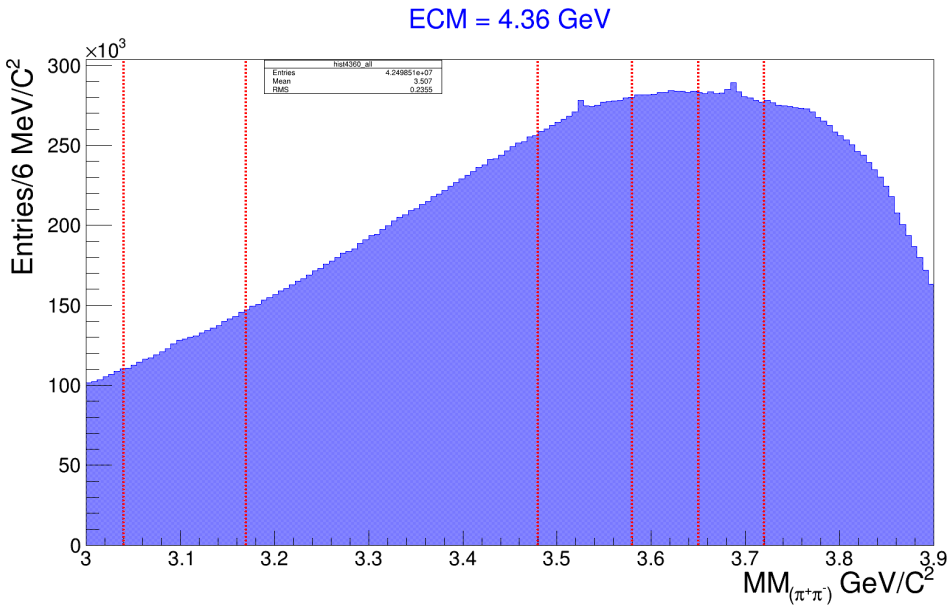

Figure 4.2: The missing mass spectrum recoiling against $\pi^+\pi^-$ for the BESIII 4360 data sample.

The data in the three regions for each energy point are described and fitted with a Gaussian (signal) and a Chebyshev polynomial of the first or second order (background). The Gaussian takes into consideration both the physical width of the particle and the dominating detector resolution. The J/ψ appears around 3.097 GeV/c^2 with a Gaussian width of $\sigma = 5$ MeV/c^2. The h_c appears in the second region with a mass of 3.523 GeV/c^2 and a $\sigma = 4$ MeV/c^2. Finally the $\psi(2S)$ is situated around 3.686 GeV/c^2 with a $\sigma = 9$ MeV/c^2. The individual fits of these three charmonium states are presented in figures 4.3, 4.4 and 4.5.

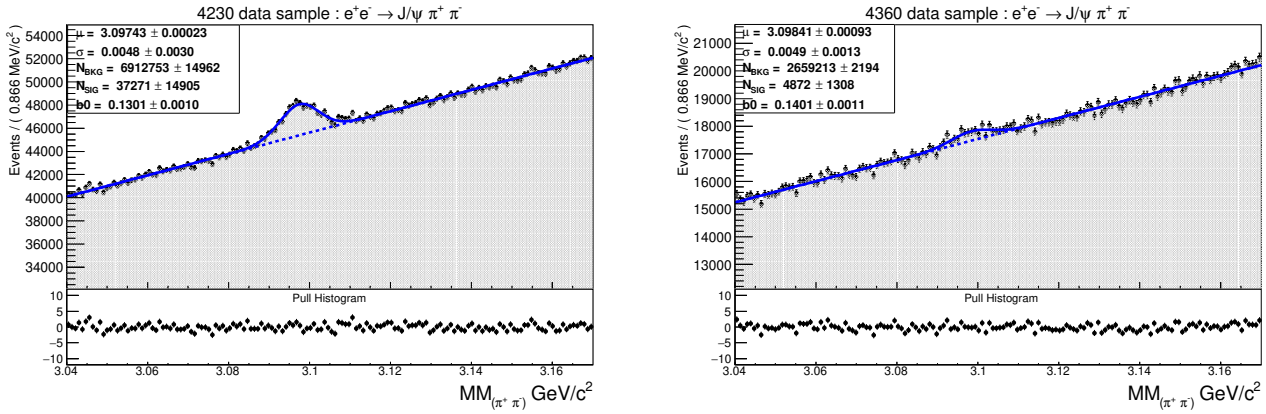

Figure 4.3: Left: The fitted missing mass spectrum recoiling against $\pi^+\pi^-$ for the BESIII 4230 data sample in the J/ψ mass region. Right: The fitted J/ψ mass region for the 4360 data sample.

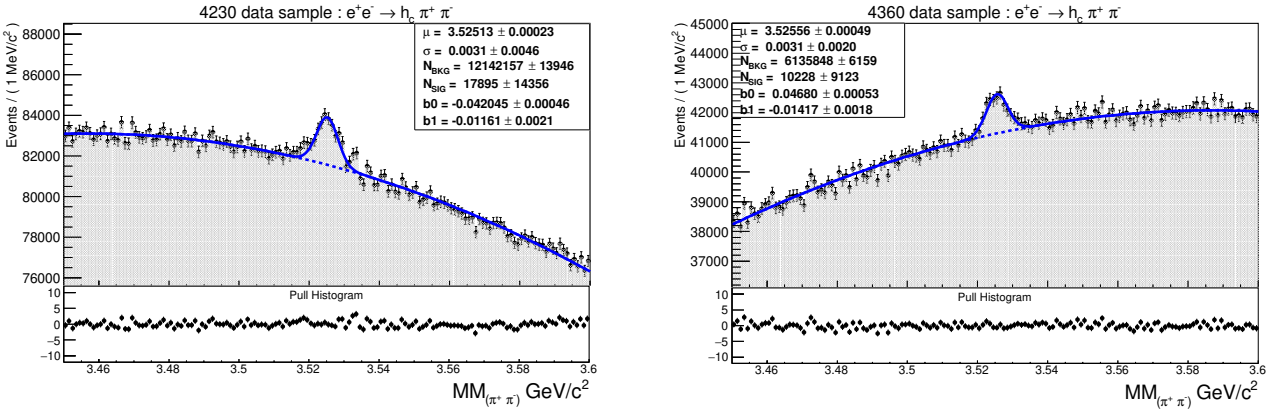

Figure 4.4: Left: The fitted missing mass spectrum recoiling against $\pi^+\pi^-$for the BESIII 4230 data sample in the h_c mass region. Right: The fitted h_c mass region for the 4360 data sample.

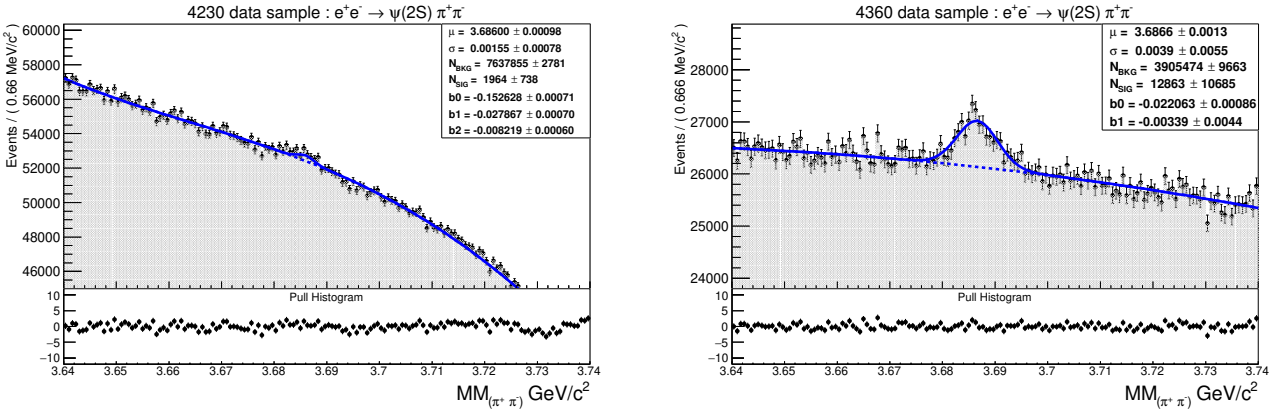

Figure 4.5: Left: The fitted missing mass spectrum recoiling against $\pi^+\pi^-$ for the BESIII 4230 data sample in the $\psi(2S)$ mass region. Right: The fitted $\psi(2S)$ mass region for the 4360 data sample.

Out of the 27 data samples, $\psi(2S)$ recoiling against $\pi^+\pi^-$ appear in only 9 data samples. The inclusive Born cross sections for this decay channel are listed in table 4.1 and the fitted missing mass distributions are presented in the appendix. Because of the lack of the $\psi(2S)$ observations, we are not able to produce an accurate description of the energy dependent cross section of $e^+e^- \rightarrow \psi(2S)\pi^+\pi^-$ above 4 GeV. On the other hand, J/ψ and h_c are observed in the majority of the data samples, their cross sections are studied and presented in subsections 1.2 and 1.3.

Table 4.1: The measured inclusive Born cross section $[\sigma(e^+e^- \to \psi(2S)\pi^+\pi^-)]$ of the XYZ BESIII data. N_{sig} the number of signal events, along with the detection efficiency ϵ, the radiative and vacuum polarization correction factors $(1 + f_{\rm ISR}) \times (1 + f_{\rm VP})$, the luminosity L and the center of mass energy $\sqrt{s}$.

DATAset	$\sqrt{s}$ MeV	$L(pb^{-1})$	$\epsilon(\%)$	N_{sig}	$(1 + f_{ISR}) \times (1 + f_{VP})$	$\sigma^{Born}(pb)$
4237	4235.70	530.30 ± 0.10	43.00	2700 ± 641	0.82 ± 0.85	14.37 ± 0.30
4280	4277.70	175.10 ± 0.10	50.00	2261 ± 751	0.82 ± 0.85	31.49 ± 0.67
4290	4287.88	500.00 ± 0.04	49.00	5447 ± 905	0.82 ± 0.85	27.12 ± 0.65
4315	4312.05	500.00 ± 0.14	47.00	7716 ± 1093	0.81 ± 0.86	40.70 ± 0.95
4340	433.739	500.00 ± 0.04	49.00	9776 ± 1039	0.81 ± 0.87	49.02 ± 1.09
4360	435.826	539.84 ± 0.04	47.00	13793 ± 1355	0.83 ± 0.89	65.52 ± 1.32
4380	437.737	500.00 ± 0.03	48.00	12113 ± 1247	0.85 ± 0.92	59.10 ± 1.39
4400	439.645	500.00 ± 0.11	45.00	11065 ± 1121	0.90 ± 0.95	54.46 ± 1.33
4420	441.558	1043.90 ± 0.11	41.00	17467 ± 1949	0.95 ± 0.95	42.89 ± 0.95

1.1 The Signal Shape of J/ψ & h_c

The large amount of background that we face in this analysis makes the task of finding a good signal description for all energy points quite challenging. With a bad signal fit, which happens occasionally for all fit parameters being free floating, we could risk a huge increase in the systematic uncertainties, especially for the polynomial and fit window related systematics. In order to avoid such problems, we chose two different approaches. The background subtraction approach and the exclusive approach.

The background subtraction approach

This approach allows us to measure the signal parameters in the background subtracted distribution and then fix the signal shape in the original missing mass distribution and fit again.

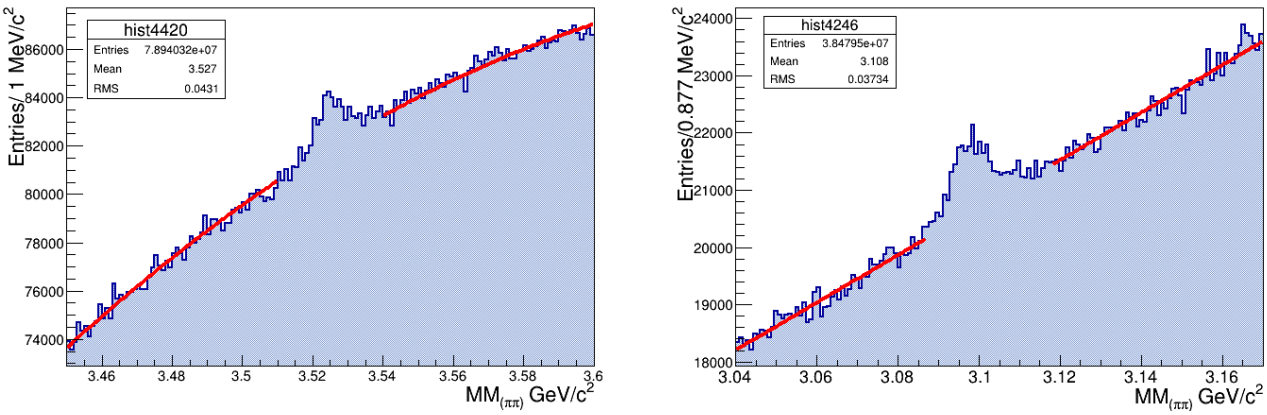

Figure 4.6: Left: Fit of the background in the J/ψ sideband regions. Right: Fit of the background in the h_c sideband regions.

The background shape is extracted by fitting the sidebands of J/ψ and h_c as shown in figure 4.6. Then the background fit function is subtracted from the actual missing mass distribution. The resulting background subtracted missing mass distributions are shown for four data samples

in the h_c region in figure 4.7 and in the J/ψ region in figure 4.8. While the fitted missing mass distributions with the signal shape fixed using this approach are shown in figures 4.9 and 4.10.

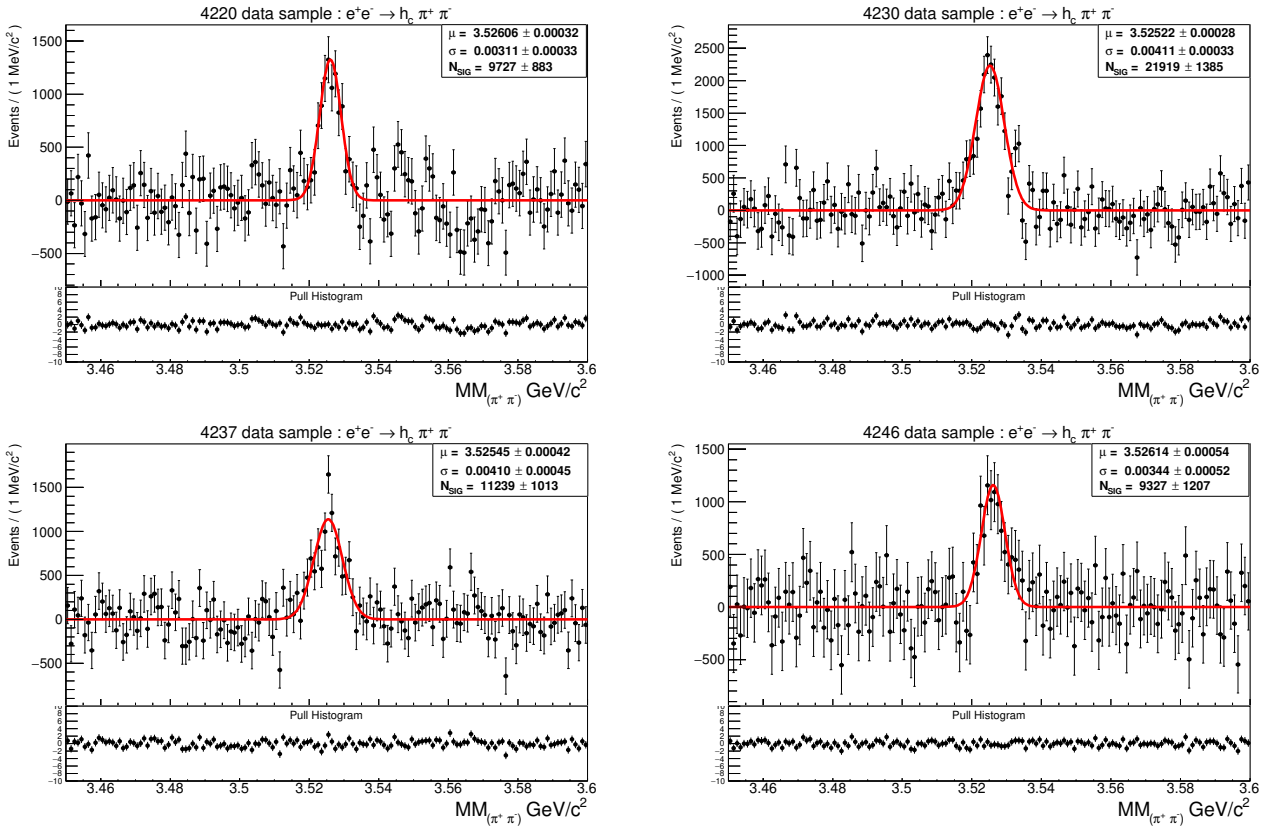

Figure 4.7: The background subtracted missing mass in the h_c region for the 4220, 4230, 4237 and 4246 data samples.

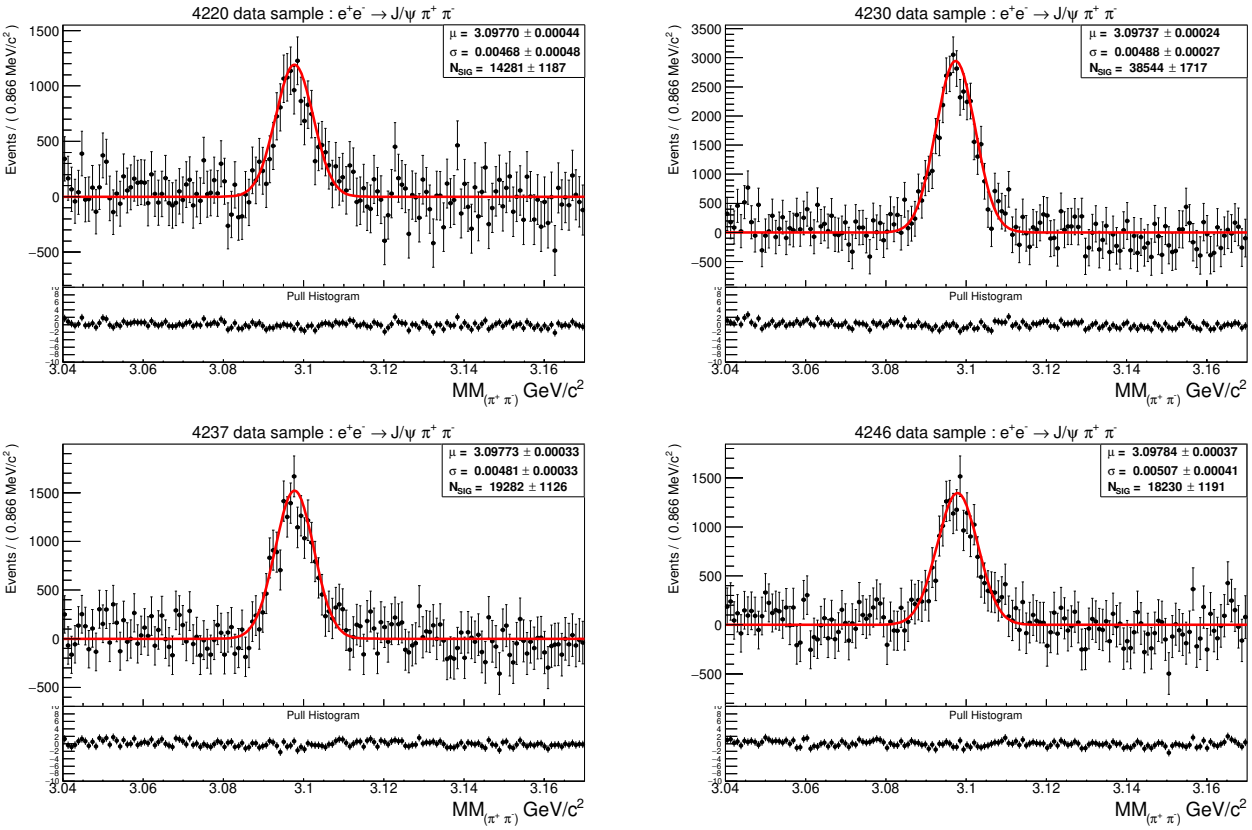

Figure 4.8: The background subtracted missing mass distributions in the J/ψ region for the 4220, 4230, 4237 and 4246 data samples

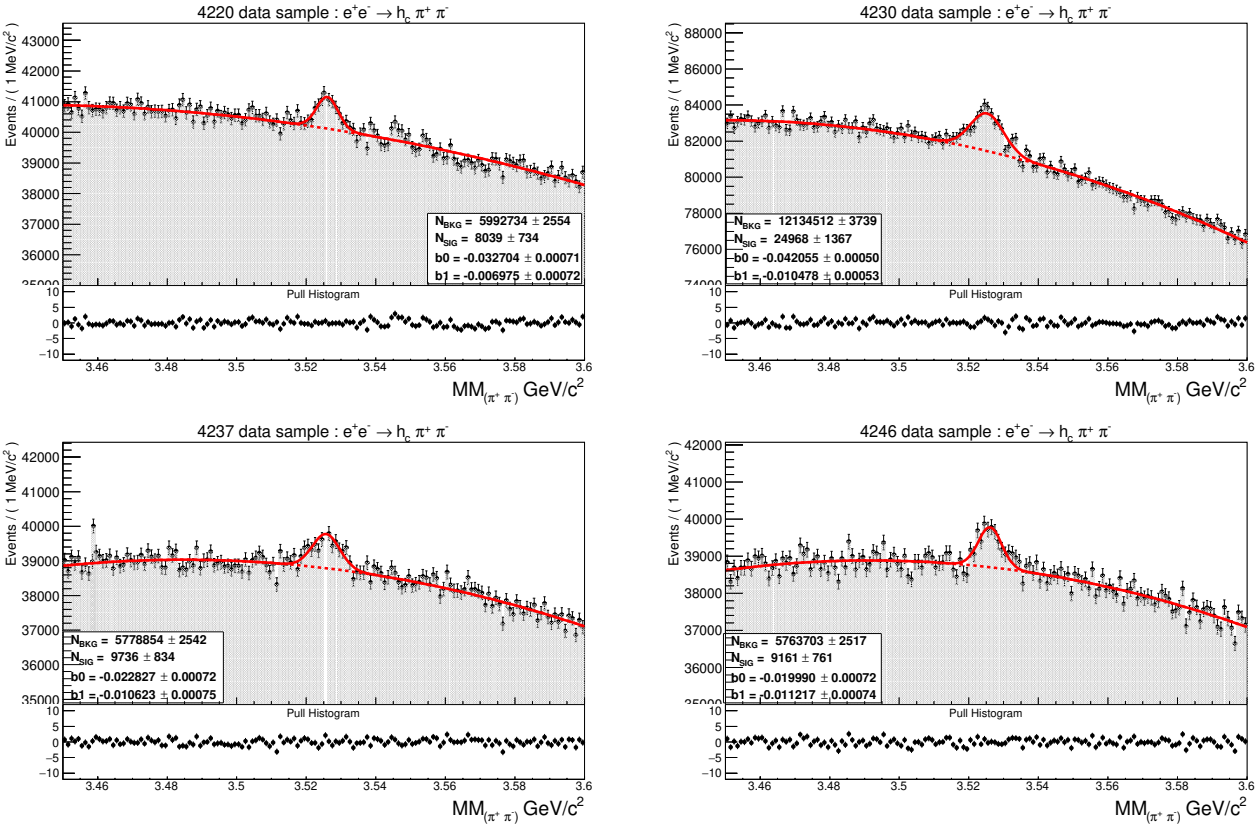

Figure 4.9: The fitted missing mass distributions with the signal shape fixed using the background subtraction approach in the h_c region for the 4220, 4230, 4237 and 4246 data samples.

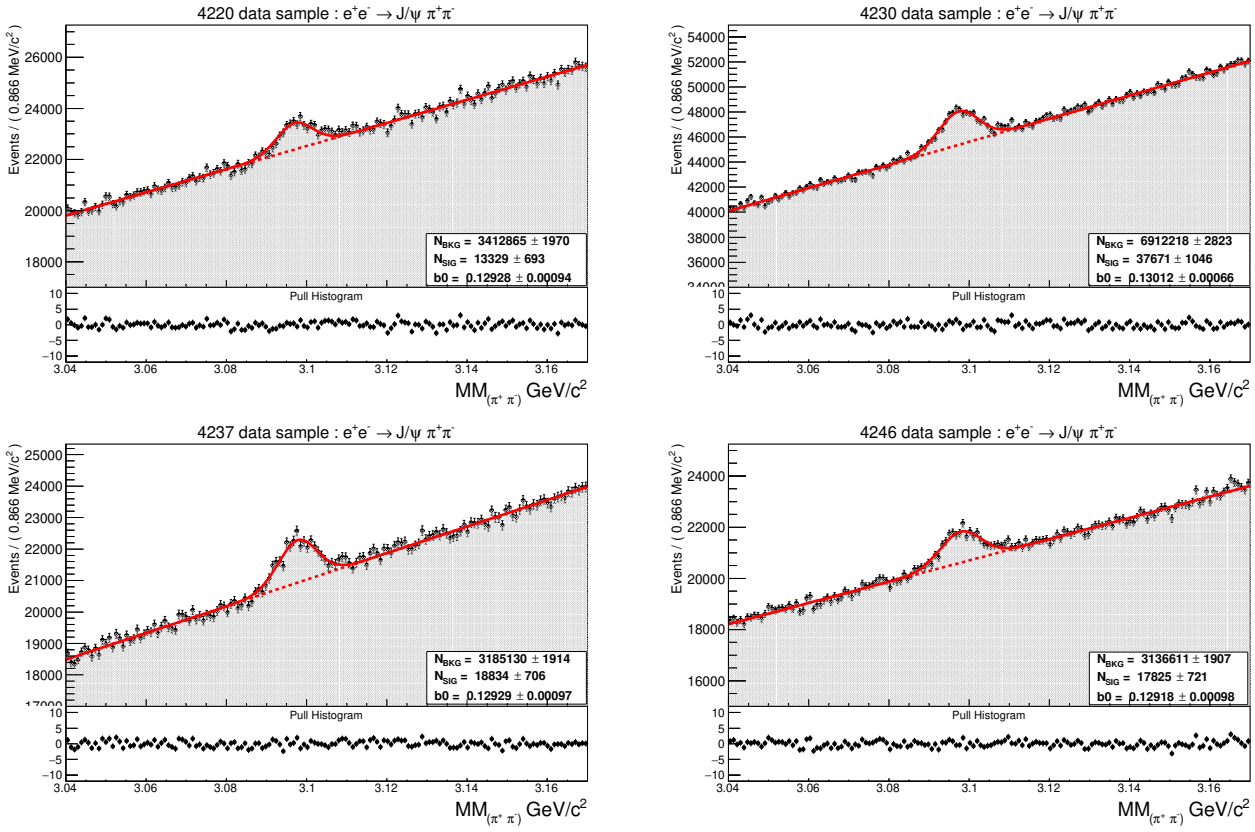

Figure 4.10: The fitted missing mass distributions with the signal shape fixed using the background subtraction approach in the J/ψ region for the 4220, 4230, 4237 and 4246 data samples.

The exclusive approach

This approach is only applicable for the $e^+e^- \to J/\psi\pi^+\pi^-$ decay channel. The signal parameters could be extracted from the missing mass distribution in an exclusive study where J/ψ is reconstructed from two leptons (e^+e^- or $\mu^+\mu^-$). In addition to the selection cuts discussed in subsection 5, a four constraint (4C) kinematic fit is applied which constrains the total four momentum of the final state particles ($\pi^+\pi^-e^+e^-$) to that of the initial beam. The chi-square χ^2 of the kinematic fit is required to be less than 60 as shown in figure 4.11. The fitted invariant mass distributions of e^+e^- after the selection cuts for two data samples 4230 and 4237 are shown in figure 4.12 while the missing mass distributions for this approach are displayed in figure 4.13.

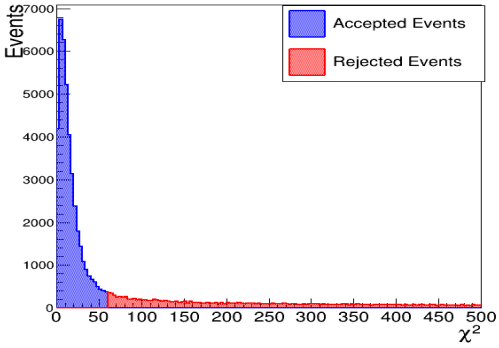

Figure 4.11: The chi-square of the 4C fit constraining the total four momentum of ($\pi^+\pi^-e^+e^-$) to that of the initial beam. The rejected events are shown in red while the accepted events are shown in blue.

The invariant and exclusive missing mass distributions in this approach are not described correctly with a Gaussian function as in the distributions of the fully inclusive analysis. A maximum likelihood fit was performed to extract the parameters of the signal, where the fit model consists of a polynomial of the first order and a reversed Crystal Ball function, which is a Gaussian function with an exponential tail on the right-hand side.

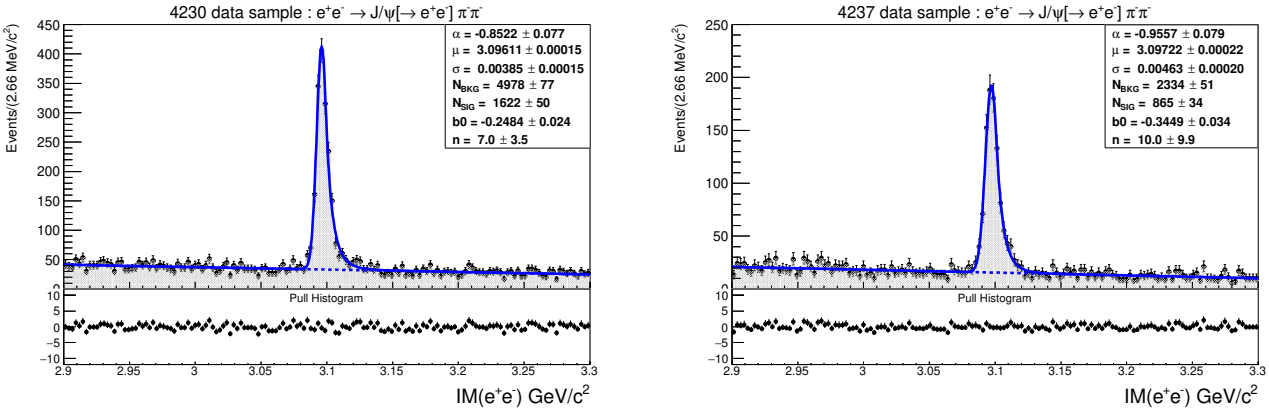

Figure 4.12: Invariant mass of two electrons in the J/ψ mass region in the exclusive approach for the 4230 and 4237 data samples

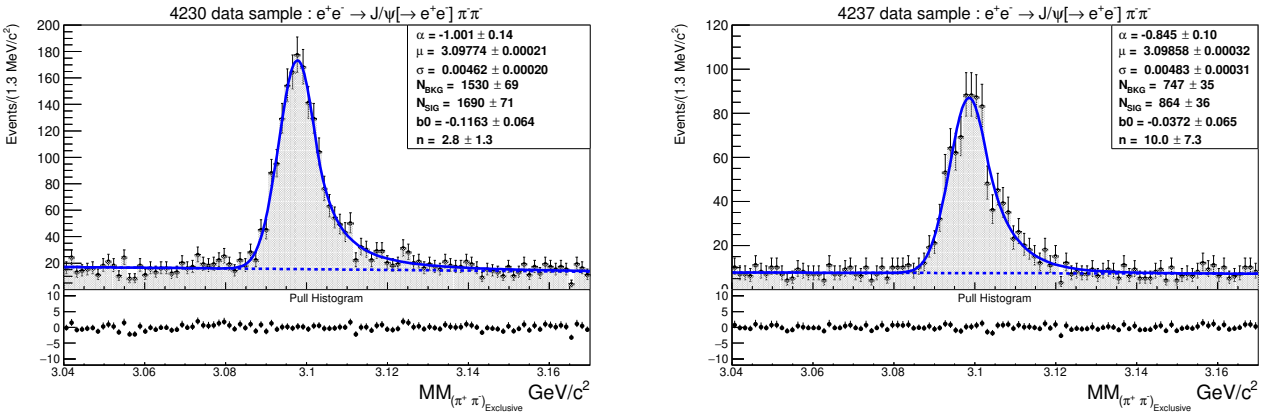

Figure 4.13: missing mass recoiling against two pions with an exclusive reconstructed J/ψ for the 4230 and 4237 data samples

The signal parameters extracted from the fits shown in figure 4.13 are used to fix the signal shape in the missing mass distributions from the fully inclusive analysis. However, based on the fits performed on a couple of data samples using this signal description approach, it was shown that the signal was not described correctly in the inclusive missing mass distributions. These failed fits and the exclusive missing mass distributions for the other data samples are shown in the appendix A.I.1. The failure of this approach could be directly related to the fact that the 4C fit corrects the lost energy of the tracks and produces artificially higher masses to match the initial momentum. This produces the radiative tail to the right-hand side which does not appear in the inclusive missing mass distributions.

Figure 4.14 shows the signal parameters from the Monte-Carlo simulation compared to the exclusive and the background subtraction approaches.

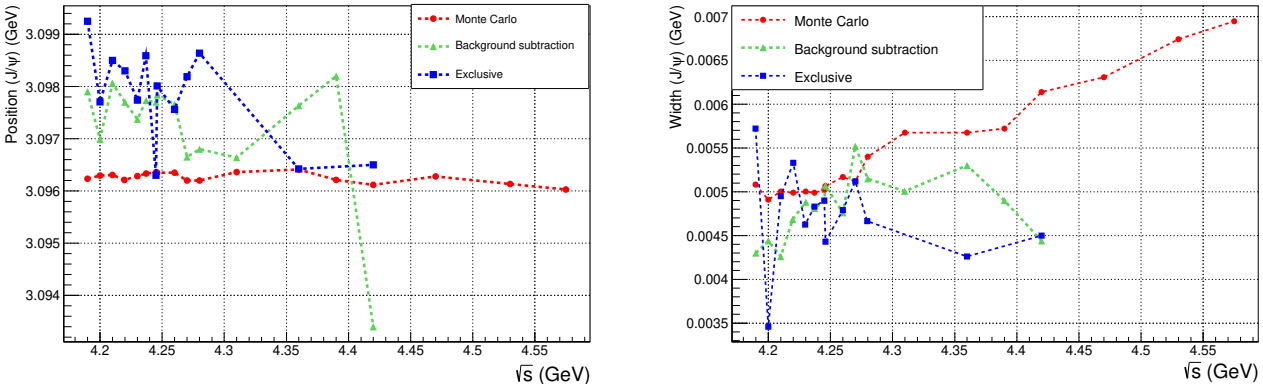

Figure 4.14: The extracted J/ψ signal parameters extracted from the fits of the Monte-Carlo simulations and the data using two approaches for different energy points. Left: The position of J/ψ for different center of mass energies. Right: The Gaussian width of the J/ψ for different center of mass energies.

Finally, we can conclude that the background subtraction approach is able to provide a more reliable description of the signal. Thus, it is used to fix the signal shape in the inclusive original missing mass distributions for the data samples where J/ψ and h_c were observed. For the samples without observation, e.g: 4530, 4575 and 4600, the signal parameters are extracted from the Monte-Carlo simulations.

1.2 Energy dependent cross sections of $e^+e^- \to J/\psi\pi^+\pi^-$

Using the background subtraction approach, the number of signal of events (N_s) is estimated. The cross section is computed using the Born cross section's formula 3.10. In table 4.2, the calculated Born cross section values for 25 data samples are presented. The 4130 and 4600 data samples are both excluded from the table. J/ψ was not observed in the missing mass of these two data samples, excluding them from the energy dependent cross section only improves the fit quality without jeopardizing the overall accuracy of the extracted parameters. The systematic uncertainties on the cross sections are explained thoroughly in chapter 5.

Table 4.2: The measured inclusive Born cross section $[\sigma(e^+e^- \to J/\psi\pi^+\pi^-)]$ of the XYZ BESIII data. N_{sig} the number of signal events, along with the detection efficiency ϵ, the radiative and vacuum polarization correction factors $(1+f_{\rm ISR})\times(1+f_{\rm VP})$, the luminosity L and the center of mass energy $\sqrt{s}$. The first uncertainty on the Born cross section is statistical, the second one is the systematic uncertainty.

DATAset	$\sqrt{s}$ MeV	$L(pb^{-1})$	$\epsilon(\%)$	N_{sig}	$(1+f_{\rm ISR})\times(1+f_{\rm VP})$	$\sigma^{Born}(pb)$
4160	4157.44	400.00 ± 0.1	49.44	2996 ± 971	0.843 ± 0.002	17.96 ± 5.82 ± 3.05
4190	4188.8	526.70 ± 0.1	44.44	1613 ± 367	0.870 ± 0.002	7.91 ± 1.80 ± 0.42
4200	4198.9	526.0 ± 0.1	46.35	5565 ± 730	0.877 ± 0.001	26.00 ± 3.42 ± 2.33
4210	4209.2	517.10 ± 0.1	45.60	9892 ± 710	0.884 ± 0.001	47.54 ± 3.44 ± 1.76
4220	4218.7	514.60 ± 0.1	45.86	13329 ± 693	0.889 ± 0.001	63.51 ±3.37 ± 2.11
4230	4226.26	1100.94 ± 0.1	46.40	37671 ± 1046	0.897 ± 0.001	83.26 ± 2.49 ± 2.60
4237	4235.7	530.30 ± 0.1	44.97	18834 ± 706	0.90 ± 0.001	88.02 ± 3.44 ± 2.74
4245	4241.66	55.88 ± 0.37	45.28	1951 ± 228	0.90 ± 0.001	85.58 ± 10.05 ± 3.75
4246	4243.8	538.10 ± 0.1	44.67	17825 ± 721	0.905 ± 0.001	82.30 ± 3.45 ± 2.97
4260	4257.97	828.40 ± 0.1	45.01	20744 ± 840	0.908 ± 0.001	61.63 ± 2.59 ± 2.05
4270	4266.8	531.10 ± 0.1	44.03	12706 ± 726	0.912 ± 0.0008	59.78 ± 3.48 ± 2.21
4280	4277.7	175.70 ± 0.1	45.89	3355 ± 395	0.916 ± 0.0007	45.60 ± 5.39 ± 2.35
4290	4287.88	500.00 ± 0.1	45.31	10159 ± 672	0.916 ± 0.0007	48.93 ± 3.28 ± 2.29
4310	4307.89	45.01 ± 0.03	44.89	330 ± 206	0.921 ± 0.0007	17.69 ±11.04 ± 3.19
4315	4312.05	500.00 ± 0.1	44.47	8454 ± 666	0.923 ± 0.0006	41.16 ± 3.27 ± 2.20
4340	4337.39	500.00 ± 0.1	45.04	5600 ± 539	0.929 ± 0.0006	26.75 ± 2.59 ± 2.05
4360	4358.26	543.90 ± 0.1	43.79	5149 ± 671	0.933 ± 0.0006	23.32 ± 3.50 ± 4.13
4380	4377.37	500.00 ± 0.1	43.98	2902 ± 645	0.938 ± 0.0005	14.05 ±3.12 ± 5.95
4390	4387.40	55.57 ± 0.003	43.01	153 ± 222	0.940 ± 0.0004	6.80 ± 9.87 ± 1.44
4400	4396.45	500.00 ± 0.1	43.00	1679 ± 379	0.943 ± 0.0007	8.27 ± 1.87 ± 1.40
4420	4415.58	1090.7 ± 0.1	31.22	1983 ± 825	0.946 ± 0.0005	6.42 ± 2.67 ± 2.68
4440	4436.24	570.00 ± 0.1	44.02	2586 ± 864	0.952 ± 0.0005	10.82 ± 3.61 ± 0.99
4470	4467.06	111.09 ± 0.04	34.38	1008 ± 353	0.957 ± 0.0004	15.39 ± 6.7 ± 1.733
4530	4527.14	112.2 ± 0.04	33.67	277 ± 287	0.971 ± 0.0003	7.59 ± 7.87 ± 12.39
4575	4572.53	48.93 ± 0.03	35.42	329 ± 182	0.974 ± 0.0002	19.53 ± 10.80 ± 5.67

inclusive energy dependent cross section of $e^+e^- \to J/\psi\pi^+\pi^-$ is shown in Figure 4.15. The red points and curve represent the inclusive measurements and fit. The black points represent the BESIII exclusive measurements and fit from [24]. In the exclusive analysis the cross section line shape was well explained by three coherent Breit-Wigner functions or the coherent sum of an exponential and two Breit-Wigner functions. In both fit solutions, two resonant structures were observed $Y(4220)$ and $Y(4320)$ above 4 GeV. In this inclusive analysis, the energy dependent cross section is fitted as well with a coherent sum of an exponential and two Breit-Wigner functions. The resonances parameters in both studies are summarized in table 4.3.
The fit PDF is written as:

$$\sigma_{fit}^{Born} = |BW_1(s) + BW_2(s)e^{i\phi_1} + e^{c\sqrt{s}}|^2. \tag{4.1}$$

In the above expression, BW_i are the Breit-Wigner functions which take the form:

$$BW(s, m, \Gamma) = \frac{1}{m^2c^4 - s - i\sqrt{s}\Gamma}, \tag{4.2}$$

where m and Γ are the mass and width of the resonance, respectively. $BW_1(s)$ represent the first Breit-Wigner around 4.22 GeV, $BW_2(s)$ represents the second peak near 4.32 GeV, and ϕ is the relative phase between $BW_1(s)$ and $BW_2(s)$. The two resonances in both studies seem to appear in almost the same positions. The most obvious difference is the width of the second Breit-Wigner. The so called $Y(4320)$ is 35 MeV wider in the inclusive analysis. This slight inconsistency between the two studies could be contributed to the additional data points investigated in this study, which could provide a more accurate description of the energy dependent cross section. The quality of the fit is tested with the reduced chi-square method (χ^2/ndf), where ndf is the number of degree of freedom. This method is usually used to test probability of a hypothesis or the validity of a certain model. The higher this value is, the lower is the probability that the hypothesis is correct. In our case, $\chi^2/\text{ndf} = 35.29/17$ with a probability, referred to as the p-value $p = 0.005$, meaning that if we were to repeat the test multiple times we would have about 0.5% chance of finding a χ^2 for the new measurement set larger than 35.29.

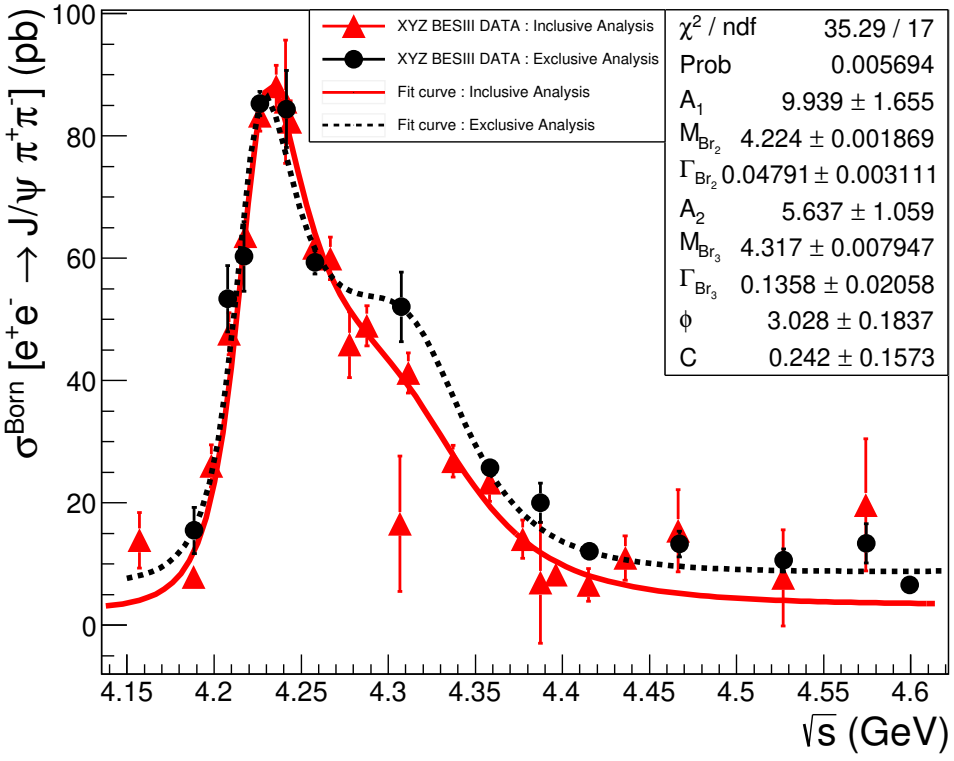

Figure 4.15: The energy dependent cross section of $e^+e^- \to J/\psi\pi^+\pi^-$ for the XYZ BESIII data samples. The exclusive BESIII previous measurements in black [24]. The inclusive measurements of this study are shown in red.

Table 4.3: Results of the fit to the $e^+e^- \to \pi^+\pi^- J/\psi$ cross section for both the inclusive and exclusive studies. $M(R_1)$ and $\Gamma(R_1)$ represent the mass and width of the first resonance below 4 GeV only fitted in the exclusive analysis. While R_2 and R_3 are the resonances above 4 GeV. The parameter ϕ is the relative phase between the two resonances.

Parameters	Inclusive Fit Results	Exclusive Fit Results
$M(R_1)(\mathrm{MeV/c^2})$	-	$3812.6^{+61.9}_{-96.6}$
$\Gamma(R_1)(\mathrm{MeV})$	-	$476.9^{+78.4}_{-64.8}$
$M(R_2)(\mathrm{MeV})$	4224.0 ± 1.8	4222.0 ± 3.1
$\Gamma(R_2)(\mathrm{MeV/c^2})$	47.91 ± 2.33	44.1 ± 4.3
$M(R_3)(\mathrm{MeV})$	4317.0 ± 7.9	4320.0 ± 10.4
$\Gamma(R_3)(\mathrm{MeV/c^2})$	135 ± 20.5	$101.1^{+25.3}_{-19.7}$
ϕ (rad)	3.03 ± 0.19	2.9 ± 0.02

1.3 Energy dependent cross sections of $e^+e^- \to h_c\pi^+\pi^-$

The measured inclusive energy dependent cross section of $e^+e^- \to h_c\pi^+\pi^-$ is shown in figure 4.16 and table 4.4. The red points and curve represent the inclusive measurements and fit. The black points represent the BESIII exclusive measurements and fit from [20]. In both the exclusive and inclusive analyses, two resonant structures were observed in the same center of mass energy regions. Due to time constraints, the newest XYZ energy points collected in 2019 are not included in the inclusive analysis of this decay channel.

Table 4.4: The measured inclusive Born cross section $[\sigma(e^+e^- \to h_c\pi^+\pi^-)]$ of the XYZ BESIII data. N_{sig} the number of signal events, along with the detection efficiency ϵ, the radiative and vacuum polarization correction factors $(1+f_{\rm ISR})\times(1+f_{\rm VP})$, the luminosity L and the center of mass energy $\sqrt{s}$. The first uncertainty on the Born cross section is statistical, the second one is the systematic uncertainty.

DATAset	$\sqrt{s}$ MeV	$L(pb^{-1})$	$\epsilon(\%)$	N_{sig}	$(1+f_{\rm ISR})\times(1+f_{\rm VP})$	$\sigma^{Born}(pb)$
4160	4157.44	400.00 ± 0.10	47.38	1000 ± 340	0.77 ± 0.002	6.91 ± 0.07 ± 6.92
4190	4188.80	526.70 ± 0.10	46.12	3729 ± 887	0.78 ± 0.003	19.80 ± 0.20 ± 1.42
4200	4198.90	526.00 ± 0.10	48.01	6101 ± 887	0.76 ± 0.003	31.74 ± 0.39 ± 3.32
4210	4209.20	517.10 ± 0.10	47.23	5271 ± 699	0.78 ± 0.003	27.98 ± 0.27 ± 0.93
4220	4218.70	514.60 ± 0.10	46.72	7950 ± 731	0.79 ± 0.005	42.63 ± 0.42 ± 1.98
4230	4226.26	1091.74 ± 0.15	46.83	22762 ± 1242	0.81 ± 0.007	56.00 ± 0.53 ± 2.55
4237	4235.70	530.30 ± 0.10	44.07	9928 ± 881	0.85 ± 0.007	50.59 ± 0.51 ± 1.75
4245	4241.66	55.88 ± 0.10	43.56	960 ± 234	0.86 ± 0.007	46.35 ± 0.66 ± 2.70
4246	4243.80	538.10 ± 0.13	43.19	9161 ± 761	0.86 ± 0.008	45.99 ± 0.51 ± 1.46
4260	4257.97	825.67 ± 0.10	44.81	11673 ± 945	0.86 ± 0.008	37.08 ± 0.38 ± 1.39
4270	4266.80	531.10 ± 0.03	43.13	6756 ± 652	0.85 ± 0.009	35.03 ± 0.37 ± 2.45
4280	4277.70	175.10 ± 0.10	44.25	2617 ± 520	0.85 ± 0.009	39.94 ± 0.43 ± 8.76
4310	4307.89	45.08 ± 0.04	44.17	856 ± 336	0.86 ± 0.008	49.94 ± 0.50 ± 12.94
4360	4358.26	539.84 ± 0.04	43.07	11025 ± 816	0.92 ± 0.009	52.31 ± 0.58 ± 11.75
4390	4387.40	55.70 ± 0.11	41.12	1110 ± 319	0.95 ± 0.008	51.30 ± 0.62 ± 6.48
4420	4415.58	1043.90 ± 0.00	41.17	20655 ± 854	0.94 ± 0.010	51.11 ± 0.61 ± 1.59
4470	4467.06	111.09 ± 0.00	39.06	602 ± 329	1.25 ± 0.020	11.15 ± 0.14 ± 0.86
4530	4527.14	112.12 ± 0.00	39.54	227 ± 389	1.05 ± 0.010	4.94 ± 4.94 ± 4.08
4575	4572.53	48.93 ± 0.00	39.04	142 ± 242	1.15 ± 0.010	6.42 ± 6.42 ± 3.65

The inclusive energy dependent cross section is fitted with two coherent Breit-Wigner functions and an exponential.

The first Breit-Wigner $BW_1(s)$ appears around 4.23 GeV, the second Breit-Wigner $BW_2(s)$ near 4.37 GeV, the inclusive results are consistent with the exclusive measurements. The difference in positions between the two studies is around 15 MeV for the first resonance and 4 MeV for the second resonance. The width of the first resonance in this study is found to be around 5 MeV wider than the values reported in the previous study, while the second one is around 30 MeV narrower in the inclusive energy dependent cross section. The fit quality was tested using a chi-square method. The used fit function gives $\chi^2/\text{ndf} = 19.27/12$, with a probability of 0.082, which implies a good quality of fit. The resonances parameters in both studies are summarized in table 4.5.

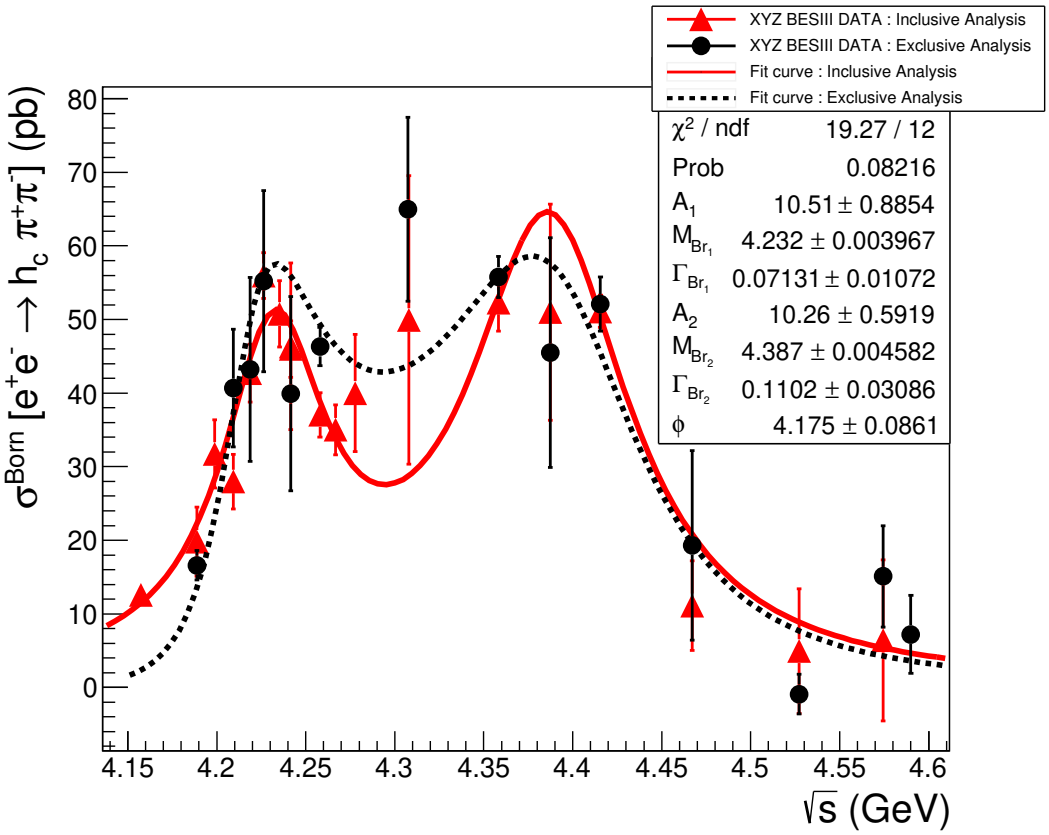

Figure 4.16: The energy dependent cross section of $e^+e^- \to h_c\pi^+\pi^-$ for the XYZ BESIII data samples. The exclusive BESIII previous measurements are shown in black [20]. The inclusive measurements of this study are shown in red.

Table 4.5: Results of the fit to the $e^+e^- \to h_c\pi^+\pi^-$ cross section for both the inclusive and exclusive studies. $M(R_i)$ and $\Gamma(R_i)$ represent the masses and widths of the two resonances R_1 and R_2. The parameter ϕ is the relative phase between the two resonances.

Parameters	Inclusive Fit Results	Exclusive Fit Results
$M(R_1)(\mathrm{MeV/c^2})$	4232 ± 3.96	$4218.4^{+5.5}_{-4.5} \pm 0.9$
$\Gamma(R_1)(\mathrm{MeV})$	71.31 ± 10.72	$66.0^{+12.3}_{-8.3} \pm 0.4$
$M(R_2)$ $(\mathrm{MeV/c^2})$	4387 ± 4.58	$4391.5^{+6.3}_{-6.8} \pm 1.0$
$\Gamma(R_2)(\mathrm{MeV})$	110.2 ± 30.86	$139.5^{+16.2}_{-20.6} \pm 0.6$
ϕ (rad)	4.175 ± 0.08	$3.1^{+0.7}_{-0.9} \pm 0.2$

2 Analysis of $e^+e^- \to X_{c\bar{c}}K^+K^-$

Similar to the $\pi^+\pi^-$, investigating the K^+K^- recoil system could offer more insight about the Y states. The $Y(4260)$ in particular was observed to decay to $J/\psi K^+K^-$ and had some unobserved decay modes involving also the K^+K^- system, e.g. $\pi^0 K^- K^+$. As already stated in subsection, beside the standard BESIII selection cuts, veto cuts are applied to the invariant mass of the recoil system. In the K^+K^- case, the events where the two kaons are combined to form $\phi(1020)$ and D^0 are rejected. As shown in figure 4.17, $\phi(1020)$ appear in the first region, D^0 in the second region of IM(K^+K^-). The peak around 1.9 GeV arise from misidentified kaons so it is not taken into consideration. The fitted distributions of the invariant masses of $\phi(1020)$ and D^0 are shown in figure 4.18. The signal fit model consists of a Breit-Wigner function in the case of $\phi(1020)$ and a Gaussian function in the case of D^0.

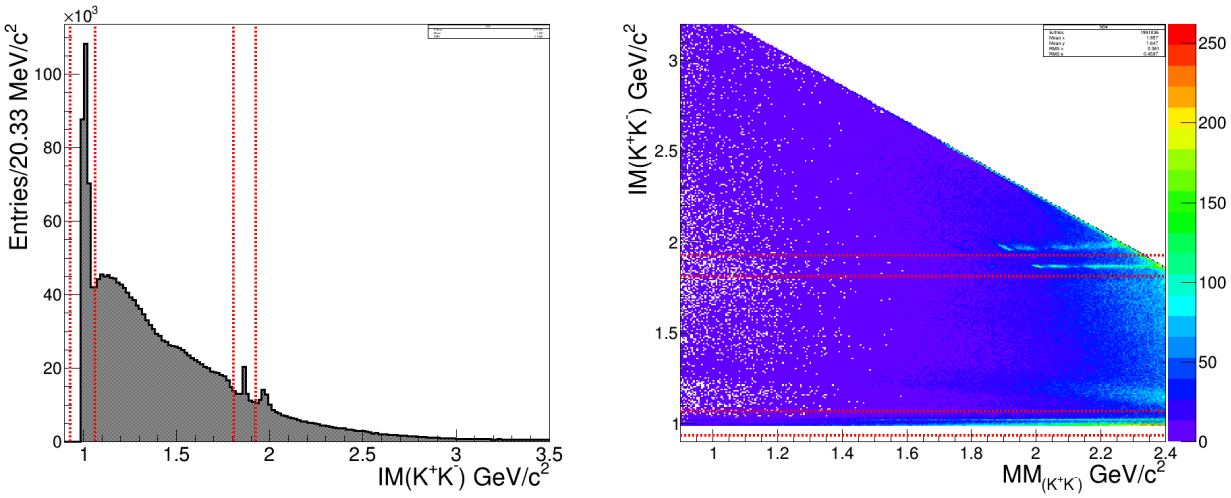

Figure 4.17: Left: The invariant mass of $[K^+K^-]$ for the 4230 data sample. Right: The scattering plot of the invariant mass and missing mass recoiling against $[K^+K^-]$.

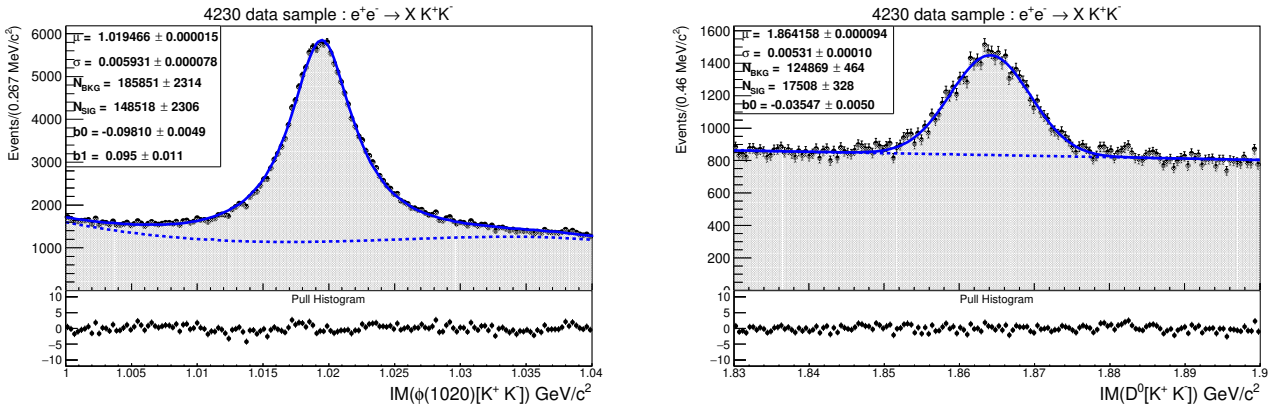

Figure 4.18: Left: The fitted invariant mass of $\phi(1020)$. Right: The fitted invariant mass of D^0.

Figure 4.19 shows the missing mass recoiling against K^+K^- after the different stages of the event selection procedure. As it is evident, the applied PID and veto cuts are very efficient in

eliminating a high percentage of the combinatorial background. Mainly three states J/ψ, $\phi(1020)$ and $\omega(782)$ are observed to be recoiling against K^+K^-.

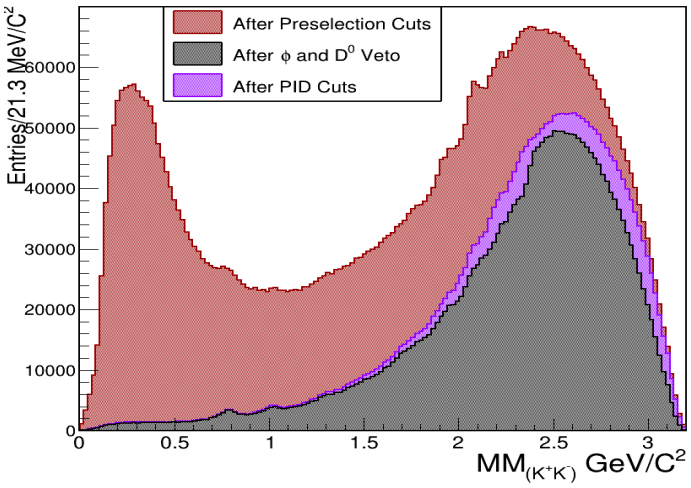

Figure 4.19: The missing mass recoiling against(K^+K^-) after different stages of the selection procedure.

The observation of J/ψ is displayed for two different BESIII data samples in figure 4.20. Similarly to the $(\pi^+\pi^-)$ recoil system, the J/ψ mass distribution is fitted with a Gaussian and a polynomial function. Its mass as expected lies around 3097 MeV with a width of 3 MeV. The main difference between the two recoil systems is that the $e^+e^- \to J/\psi K^+K^-$ is not as dominant as its counter partner in $\pi^+\pi^-$. Out of 27 data samples, J/ψ is only observed in 5, the cross sections of these data samples are shown in table 4.6. Moreover, the amount of background seen for this part of the analysis is less intense than in the charged pions case. The kaon system is more than three times heavier than the pion system (279.14 MeV), which could explain the difference between the two modes.

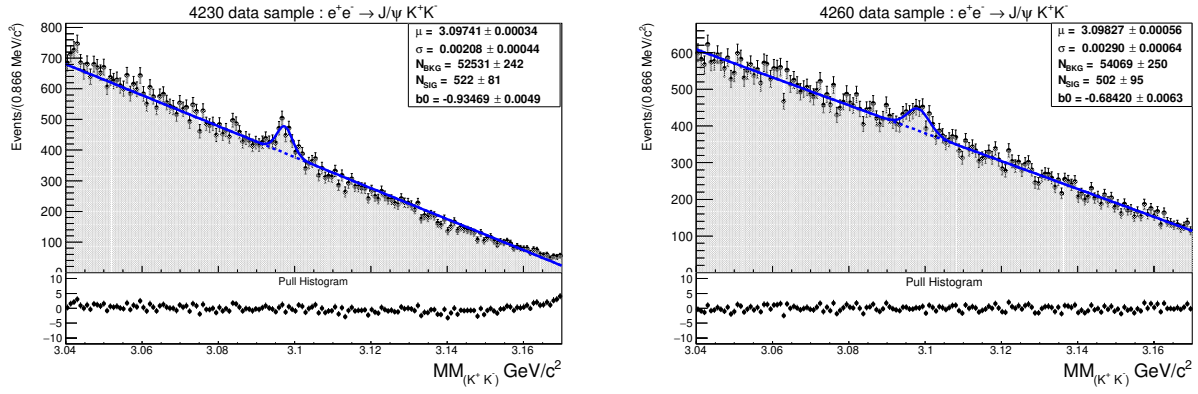

Figure 4.20: Left: J/ψ in the missing mass recoiling against (K^+K^-) for the 4230 data sample. Right: J/ψ in the missing mass recoiling against (K^+K^-) for the 4260 data sample.

Table 4.6: The measured inclusive cross section $[\sigma^{Born}(e^+e^- \to J/\psi K^+K^-)]$ of the XYZ BESIII data. N_{sig} the number of signal events, along with the detection efficiency ϵ, the radiative and vacuum polarization correction factors $(1+f_{\rm ISR})\times(1+f_{\rm VP})$ and the luminosity L.

DATAset	$L(pb^{-1})$	$\epsilon(\%)$	N_{sig}	$(1+f_{\rm ISR})\times(1+f_{\rm VP})$	$\sigma^{Born}(pb)$
4230	1091.74	17.41	522 ± 81	0.76 ± 0.14	3.61 ± 0.86
4237	530.3	17.65	542 ± 92	0.79 ± 0.17	7.33 ± 1.34
4246	538.1	16.81	469 ± 98	0.96 ± 0.13	5.40 ± 1.30
4260	825.67	19.67	502 ± 95	0.87 ± 0.21	3.55 ± 1.09
4270	531.1	19.49	232 ± 60	0.76 ± 0.23	2.94 ± 1.17

The energy dependent cross section of $e^+e^- \to J/\psi K^+K^-$ was studied exclusively in the BESIII collaboration [44]. Because of the lack of J/ψ observations in our data samples, it is not possible to produce a competitive inclusive energy dependent cross section as in the case of the $(\pi^+\pi^-)$ system.

3 Analysis of $e^+e^- \to X_{c\bar{c}}K^\pm\pi^\mp$

In the case of $K^\pm\pi^\mp$, as shown in figure 4.21, two particles appear in the invariant mass distribution, K^* in the first region around 0.9 GeV and D^0 in the second region around 1.85 GeV. As mentioned before, the $Y(4260)$ shows a suppression in open charm decays. Thus, for this recoil system, it would be more beneficial to focus on the open charm decay channels. Instead of applying a D^0 veto cut, a cut is applied to keep the events in the D^0 region and filter out all the rest of the events.

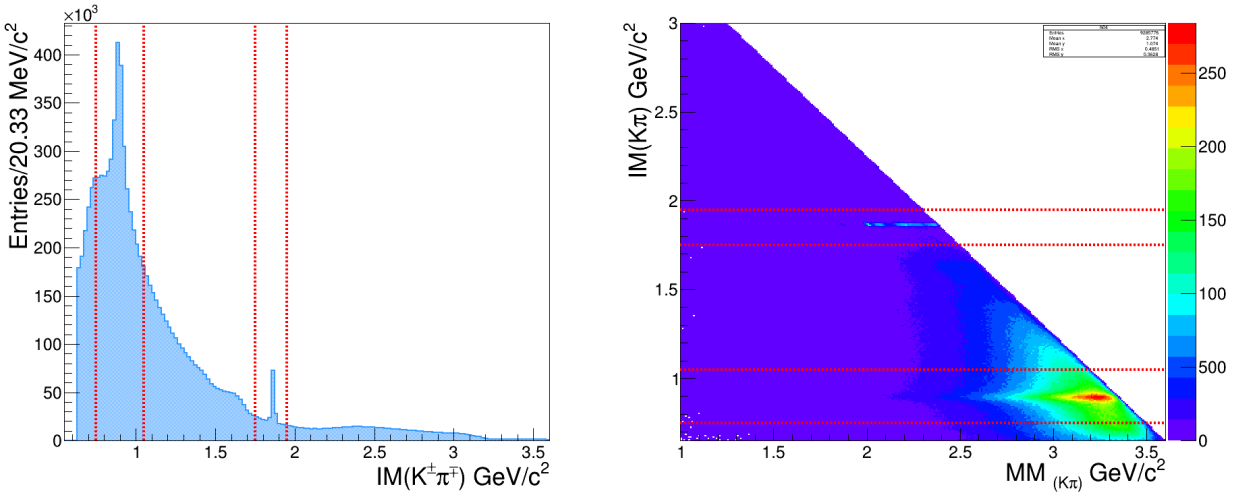

Figure 4.21: Left: The invariant mass of $[K^\pm\pi^\mp]$ for the 4246 data sample. Right: The scattering plot of the invariant mass and missing mass recoiling against $[K^\pm\pi^\mp]$.

Using the above mentioned selection cuts, the missing mass as shown in 4.22 is investigated. On the left, the missing mass distribution is shown where the D^0 events in the invariant mass were

filtered in. While on the right, the missing mass where the D^0 events are filtered out. On the left side, two physical peaks appear, in the first region, D^0 around 1.85 GeV and in the second region $D^*(2007)^0$ around 2.1 GeV. The other peaks appearing around 2, 2.2 and 2.4 GeV most likely arise from misidentified pions as kaons. On the left side, recoiling against $(K^{\pm}\pi^{\mp})$ in the first mass region are two strange mesons $K^{\pm}$ and a $K^*(892)$.

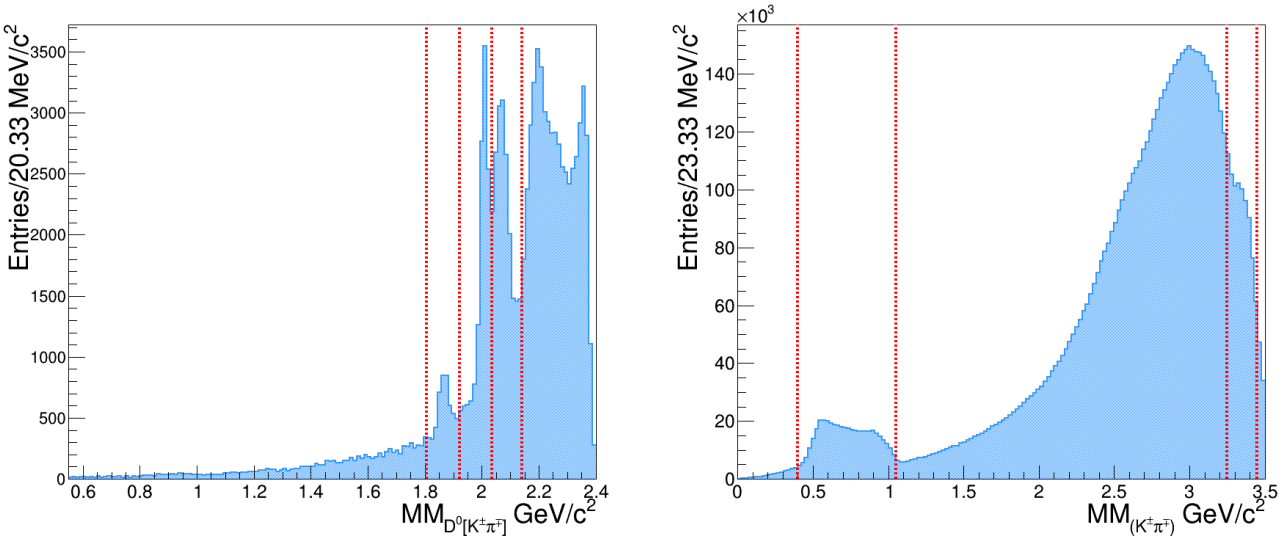

Figure 4.22: Missing mass recoiling against $D^0[K^{\pm}\pi\mp]$ after the cut on the D^0-meson mass for the 4246 data sample.

The two decay channels $e^+e^- \to D^0\bar{D}^0[K^{\pm}\pi^{\mp}]$ and $D^*(2007)^0\bar{D}^0[K^{\pm}\pi^{\mp}]$ are observed in all 27 energy data samples. The fitted D^0 and $D^*(2007)^0$ peaks for two different data samples 4246 and 4420 are displayed in figures 4.23, 4.24.

The signal parameters are extracted using a chi-square fit with a model consisting of a Gaussian function and a Chebyshev polynomial function. The fitted distributions for all data samples are presented in Appendices A.I and A.I.

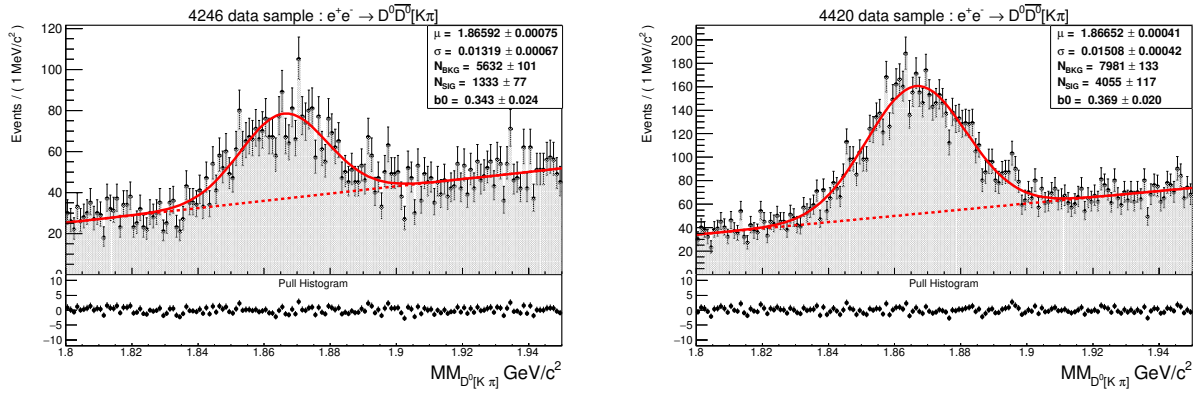

Figure 4.23: The D^0-meson in the missing mass recoiling against a $\bar{D}^0[K^{\pm}\pi\mp]$. Left: The 4246 data sample. Right: The 4420 data sample.

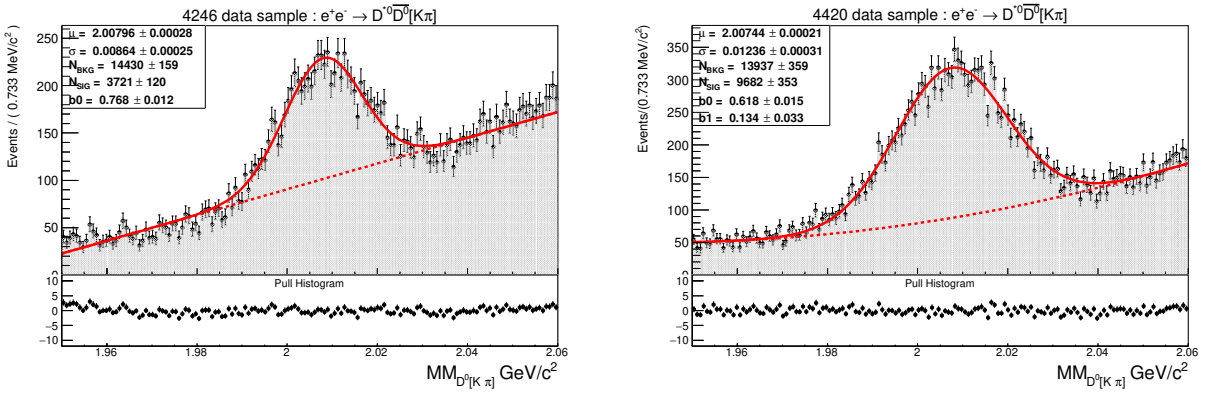

Figure 4.24: The D^{*0}-meson in missing mass recoiling against a D-meson $[K^{\pm}\pi\mp]$. Left: The 4246 data sample. Right: The 4420 data sample.

After extracting the signal yield of D^0 and $D^*(2007)^0$ from the fit, the Born cross sections are measured similarly to the other decay channels using the Born cross section formula 3.10. However, in this case, we have an intermediate decay channel $D^0 \to K^-\pi^+$. Thus, its branching ratio $Br(D^0 \to K^-\pi^+) = (3.93 \pm 0.04)\%$ [7] should be taken into consideration. The detailed values of the Born cross sections for both decay channels are presented in tables 4.7, 4.8. The energy dependent cross sections are shown in figures 4.25, 4.26.

Table 4.7: The measured inclusive cross section $[\sigma^{Born}(e^+e^- \to D^0\bar{D}^0)]$ of the XYZ BESIII data. N_{sig} the number of signal events, along with the detection efficiency ϵ, the radiative and vacuum polarization correction factors $(1 + f_{\rm ISR}) \times (1 + f_{\rm VP})$ and the luminosity L. The first uncertainty on the Born cross section is statistical, the second one is the systematic uncertainty.

DATAset	$\sqrt{s}$ MeV	$L(pb^{-1})$	$\epsilon(\%)$	N_{sig}	$(1+\delta_{ISR}) \times (1+\delta_{VP})$	$\sigma^{Born}(nb)$
4130	412.848	400.0 ± 0.10	48.6	3969 ± 97	0.973 ± 0.011	0.534 ± 0.010 ± 0.018
4160	415.744	400.0 ± 0.10	40.7	2453 ± 87	1.138 ± 0.007	0.336 ± 0.006 ± 0.034
4190	418.880	526.7 ± 0.10	40.8	3113 ± 95	1.060 ± 0.013	0.347 ± 0.006 ± 0.044
4200	419.890	526.0 ± 0.10	42.7	3227 ± 96	1.006 ± 0.002	0.363 ± 0.005 ± 0.035
4210	420.920	517.1 ± 0.10	43.0	3104 ± 94	0.982 ± 0.014	0.362 ± 0.007 ± 0.015
4220	421.870	514.6 ± 0.15	41.6	2568 ± 90	1.008 ± 0.028	0.303 ± 0.009 ± 0.020
4230	422.626	1091.7 ± 0.10	40.3	4445 ± 122	1.082 ± 0.041	0.237 ± 0.010 ± 0.013
4237	423.570	530.3 ± 0.10	34.2	1372 ± 75	1.177 ± 0.043	0.163 ± 0.006 ± 0.006
4245	424.166	55.8 ± 0.13	32.3	101 ± 20	1.329 ± 0.028	0.107 ± 0.003 ± 0.013
4246	424.380	538.1 ± 0.10	31.7	1333 ± 77	1.410 ± 0.035	0.141 ± 0.004 ± 0.018
4260	425.797	825.6 ± 0.03	29.8	1719 ± 87	1.349 ± 0.029	0.132 ± 0.004 ± 0.007
4270	426.680	531.1 ± 0.10	29.8	1142 ± 74	1.358 ± 0.029	0.135 ± 0.004 ± 0.026
4280	427.770	175.1 ± 0.04	27.8	403 ± 46	1.463 ± 0.021	0.144 ± 0.003 ± 0.020
4290	428.788	500.0 ± 0.04	28.1	803 ± 66	1.521 ± 0.004	0.096 ± 0.002 ± 0.010
4310	430.789	45.0 ± 0.14	27.8	75 ± 17	1.452 ± 0.020	0.105 ± 0.002 ± 0.053
4315	431.205	500.0 ± 0.04	31.0	823 ± 67	1.394 ± 0.023	0.097 ± 0.002 ± 0.010
4340	433.739	500.0 ± 0.04	35.4	789 ± 72	1.207 ± 0.015	0.094 ± 0.002 ± 0.006
4360	435.826	539.8 ± 0.03	37.2	1225 ± 75	1.127 ± 0.001	0.138 ± 0.002 ± 0.007
4380	437.737	500.0 ± 0.11	41.2	1287 ± 76	1.077 ± 0.003	0.148 ± 0.002 ± 0.027
4390	438.740	55.7 ± 0.11	39.6	159 ± 21	1.068 ± 0.001	0.172 ± 0.002 ± 0.008
4400	439.645	500.0 ± 0.04	42.6	2023 ± 82	1.058 ± 0.000	0.229 ± 0.003 ± 0.019
4420	441.558	1043.9 ± 0.04	40.4	4055 ± 117	1.053 ± 0.000	0.232 ± 0.003 ± 0.010
4440	443.624	570.0 ± 0.03	42.4	2160 ± 92	1.053 ± 0.001	0.216 ± 0.003 ± 0.012
4470	446.706	111.0 ± 0.01	39.9	358 ± 30	1.056 ± 0.002	0.195 ± 0.003 ± 0.008
4530	452.714	112.1 ± 0.01	37.2	250 ± 27	1.070 ± 0.004	0.143 ± 0.002 ± 0.028
4575	457.450	48.9 ± 0.01	33.8	38 ± 12	1.129 ± 0.000	0.052 ± 0.001 ± 0.004

Table 4.8: The measured inclusive cross section $[\sigma^{Born}(e^+e^- \to D^{*0}\bar{D}^0)]$ of the XYZ BESIII data. N_{sig} the number of signal events, along with the detection efficiency ϵ, the radiative and vacuum polarization correction factors $(1 + f_{\rm ISR}) \times (1 + f_{\rm VP})$ and the luminosity L. The first uncertainty on the Born cross section is statistical, the second one is the systematic uncertainty.

DATAset	$\sqrt{s}$ MeV	$L(pb^{-1})$	$\epsilon(\%)$	N_{sig}	$(1+\delta_{ISR}) \times (1+\delta_{VP})$	$\sigma^{Born}(nb)$
4130	412.848	400.0 ± 0.10	32.8	6513 ± 241	1.071 ± 0.011	1.179 ± 0.029 ± 0.222
4160	415.744	400.0 ± 0.10	32.3	6024 ± 230	1.104 ± 0.007	1.074 ± 0.016 ± 0.126
4190	418.880	526.7 ± 0.10	29.9	6675 ± 259	1.060 ± 0.013	1.017 ± 0.019 ± 0.092
4200	419.890	526.0 ± 0.10	29.0	6175 ± 246	1.157 ± 0.002	0.891 ± 0.013 ± 0.074
4210	420.920	517.1 ± 0.10	27.9	5093 ± 233	1.180 ± 0.014	0.761 ± 0.014 ± 0.084
4220	421.870	514.6 ± 0.15	26.7	4783 ± 204	1.207 ± 0.028	0.734 ± 0.020 ± 0.033
4230	422.626	1091.7 ± 0.10	27.0	9643 ± 279	1.240 ± 0.041	0.671 ± 0.025 ± 0.022
4237	423.570	530.3 ± 0.10	25.6	4489 ± 187	1.280 ± 0.043	0.657 ± 0.024 ± 0.025
4245	424.166	55.8 ± 0.13	24.5	571 ± 64	1.314 ± 0.028	0.808 ± 0.022 ± 0.048
4246	424.380	538.1 ± 0.10	24.1	3721 ± 120	1.402 ± 0.035	0.521 ± 0.016 ± 0.174
4260	425.797	825.6 ± 0.03	26.8	8024 ± 268	1.384 ± 0.029	0.667 ± 0.017 ± 0.038
4270	426.680	531.1 ± 0.10	27.9	5015 ± 205	1.231 ± 0.029	0.699 ± 0.019 ± 0.049
4280	427.770	175.1 ± 0.04	28.6	1516 ± 122	1.175 ± 0.021	0.656 ± 0.015 ± 0.059
4290	428.788	500.0 ± 0.040	31.2	4192 ± 81	1.138 ± 0.004	0.601 ± 0.009 ± 0.045
4310	430.789	45.1 ± 0.14	30.1	408 ± 230	1.111 ± 0.020	0.689 ± 0.016 ± 0.126
4315	431.205	500.0 ± 0.10	31.1	4352 ± 232	1.077 ± 0.023	0.661 ± 0.017 ± 0.046
4340	433.739	500.0 ± 0.04	32.2	4174 ± 264	1.071 ± 0.015	0.616 ± 0.012 ± 0.60
4360	435.826	539.8 ± 0.03	31.2	5273 ± 198	1.049 ± 0.001	0.759 ± 0.011 ± 0.060
4380	437.737	500.0 ± 0.10	32.1	4622 ± 88	1.038 ± 0.003	0.706 ± 0.010 ± 0.183
4390	438.740	55.7 ± 0.11	31.0	560 ± 176	1.030 ± 0.001	0.801 ± 0.011 ± 0.064
4400	439.645	500.0 ± 0.04	32.3	4271 ± 353	1.026 ± 0.000	0.656 ± 0.009 ± 0.084
4420	441.558	1043.9 ± 0.04	31.3	9682 ± 306	1.023 ± 0.000	0.737 ± 0.010 ± 0.049
4440	443.624	570.0 ± 0.03	32.6	5311 ± 127	1.018 ± 0.001	0.715 ± 0.010 ± 0.074
4470	446.706	111.1 ± 0.01	31.1	1015 ± 222	1.013 ± 0.002	0.738 ± 0.010 ± 0.144
4530	452.714	112.1 ± 0.01	31.0	981 ± 84	1.006 ± 0.004	0.714 ± 0.010 ± 0.150
4575	457.450	48.9 ± 0.01	29.3	288 ± 0	1.006 ± 0.000	0.508 ± 0.007 ± 0.195

In the energy dependent cross section of $e^+e^- \to D^0\bar{D}^0$, shown in figure 4.25, two enhancements appear around 4.19 GeV and 4.42 GeV, respectively. The cross section is fitted with a coherent sum of two Breit-Wigner functions. In order to achieve the best fit, the cross section of the first data sample 4130 was excluded from this fit. However, with a cross section equal to $\sigma_{4130}(D\bar{D}) = 0.534 \pm 0.010 \pm 0.018$ nb, there could be a possible interpretation of a third Breit-Wigner function in the range of $[4, 4.14]$ GeV. The extracted fit parameters are displayed in table 4.9.

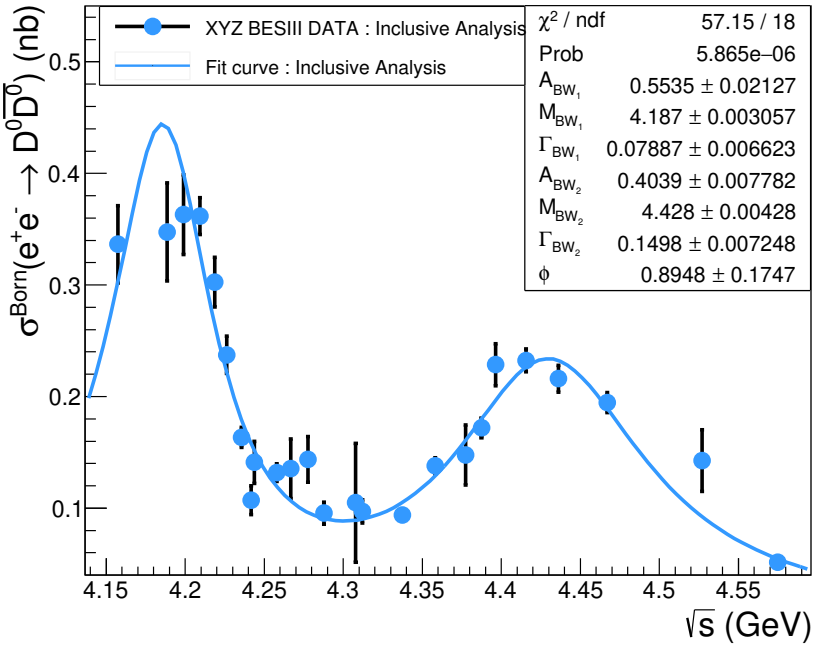

Figure 4.25: Energy dependent cross section of $e^+e^- \to D^0\bar{D}^0$ for energies above 4 GeV. The statistical and systematic uncertainties on the cross sections are both displayed.

Table 4.9: Results of the fit to the $e^+e^- \to D^0\bar{D}^0$ cross section extracted in this inclusive study. $M(R_i)$ and $\Gamma(R_i)$ represent the masses and widths of the two resonances R_1 and R_2. The parameter ϕ is the relative phase between the two resonances.

Parameters	Inclusive Fit Results
$M(R_1)(\mathrm{MeV/c^2})$	4187 ± 3.05
$\Gamma(R_1)(\mathrm{MeV})$	78.87 ± 6.62
$M(R_2)$ $(\mathrm{MeV/c^2})$	4428 ± 4.28
$\Gamma(R_2)(\mathrm{MeV})$	149.8 ± 7.28
ϕ (rad)	0.89 ± 0.17

In the energy dependent cross section of $e^+e^- \to D^*(2007)^0\bar{D}^0$, shown in figure 4.26, at least two possible enhancements appear in the data. Similar to the cross section in the $D\bar{D}$ channel, this could be the case of a three (or two) Breit-Wigner functions fit. If $\sigma_{4130}(D^*\bar{D})$ is excluded from the energy dependent cross section, the first resonance lies around 4.18 GeV and the second one around 4.4 GeV. The fit parameters of the two resonances are listed in table 4.9.

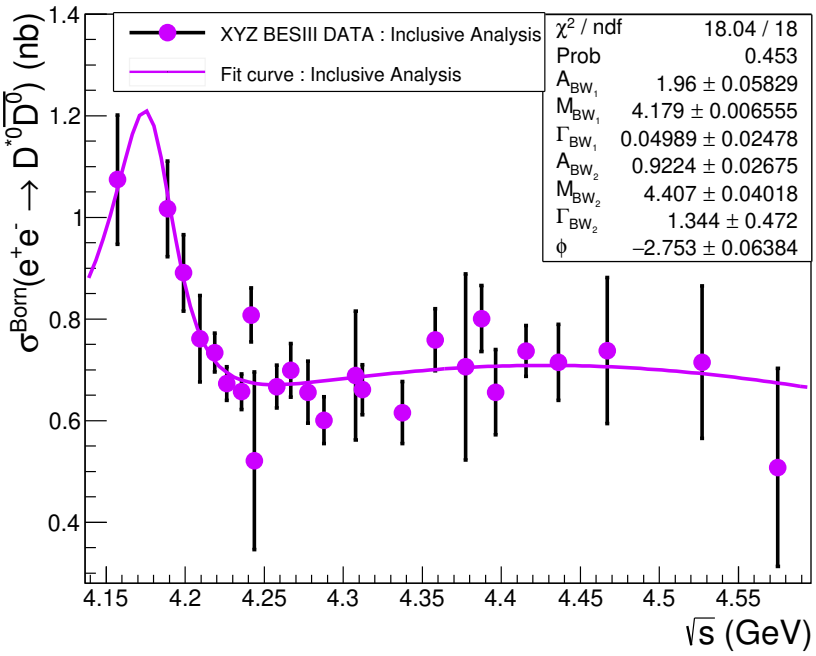

Figure 4.26: Energy dependent cross section of $e^+e^- \to D^{*0}\bar{D}^0$ for energies above 4 GeV. The statistical and systematic uncertainties on the cross sections are both displayed.

Table 4.10: Results of the fit to the $e^+e^- \to D^{*0}\bar{D}^0$ cross section extracted in this inclusive study. $M(R_i)$ and $\Gamma(R_i)$ represent the masses and widths of the two resonances R_1 and R_2. The parameter ϕ is the relative phase between the two resonances.

Parameters	Inclusive Fit Results
$M(R_1)(\mathrm{MeV/c^2})$	4179 ± 6.55
$\Gamma(R_1)(\mathrm{MeV})$	49.89 ± 24.78
$M(R_2)$ $(\mathrm{MeV/c^2})$	4407 ± 40.18
$\Gamma(R_2)(\mathrm{MeV})$	1344 ± 472
ϕ (rad)	-2.75 ± 0.06

These two decay channels were studied exclusively by the Belle collaboration in [45] and by the BaBar collaboration in [46]. Our inclusive cross sections are in the same order of the ones measured in these publications. The mass spectra in the Babar study showed a production of the following 1^{--} states: $\psi(3370)$, $\psi(4040)$, $\psi(4160)$ and $\psi(4415)$. Since we are targeting in this analysis the energy region between $[4.13, 4.6]$ GeV, it is possible that the first enhancement in the cross sections around 4.13 GeV is a sign of the $\psi(4040)$ resonance while the two other fitted resonances R_1 and R_2 are actually the $\psi(4160)$ and the $\psi(4415)$, respectively.

CHAPTER 5

SYSTEMATIC UNCERTAINTIES

In this chapter, the systematic uncertainties relevant for the cross section measurements of $e^+e^- \to J/\psi\pi^+\pi^-$, $e^+e^- \to h_c\pi^+\pi^-$ and $e^+e^- \to D^0(D^{*0})\bar{D}^0[K^\pm\pi^\mp]$ are discussed. The systematic uncertainties for the Born cross sections come mainly from the luminosity measurement, tracking, PID, the fitting range and the background shape.

1 Systematic Contributions

1.1 Luminosity Measurements Uncertainty

The integrated luminosities for the data samples have been measured using Bhabha events ($e^+e^- \to (\gamma)e^+e^-$) and then to verify the results a cross-check with di-gamma events ($e^+e^- \to \gamma\gamma$) is performed. The uncertainty of the measurement is considered to be less than 1% and it is taken as systematic uncertainty for each energy point. [47]

1.2 Tracking Uncertainty

The uncertainty of the MDC tracking efficiency is 1% per a track. For the studied decay channels in this analysis, the recoil systems are composed of two particles: $\pi^+\pi^-$, K^+K^- and $K^\pm\pi^\mp$ which contributes in total a systematic error of 2% for the uncertainty of tracking. [48]

1.3 Particle Identification Uncertainty

Based on the TOF and dE/dx information and the measurements of the particle identification efficiencies of $e^+e^- \to \pi^+\pi^-\pi^0$ and $K^+K^-\pi^0$ channels in [49], the difference between data and MC for the pion and kaon PID efficiencies are about 1%, and 2% is taken as the systematic error for a two pion recoil system.

1.4 Fitting Range & Background Shape Uncertainties

The fitting range and background shape uncertainties are assumed to be correlated. Namely, the fit window and background polynomial order are varied simultaneously and for each variation, the signal yield is extracted. Subsequently, one measurement representing both uncertainties is quoted for each energy point.

For the $e^+e^- \to J/\psi\pi^+\pi^-$ decay channel :

The nominal fitting range of the J/ψ in the missing mass as seen in the previous chapters is selected as W_1: [3.04, 3.17]. In order to extract the fitting range related uncertainty, two other fitting ranges W_2: [3.027, 3.183] and W_3: [3.053,3.157] are chosen with a 20% difference in respect to W_1. The background shape in the missing mass distribution is described with a first order Chebyshev polynomial function ($p1$) in the nominal fit. In order to investigate the background shape description on the signal yield and the cross sections, the background region in the missing mass distributions are fitted with a Chebyshev polynomial function of the second ($p2$) and third order ($p3$). Four out of eight fit variations are shown in figure 5.1 for the 4.237 GeV data sample as an example.

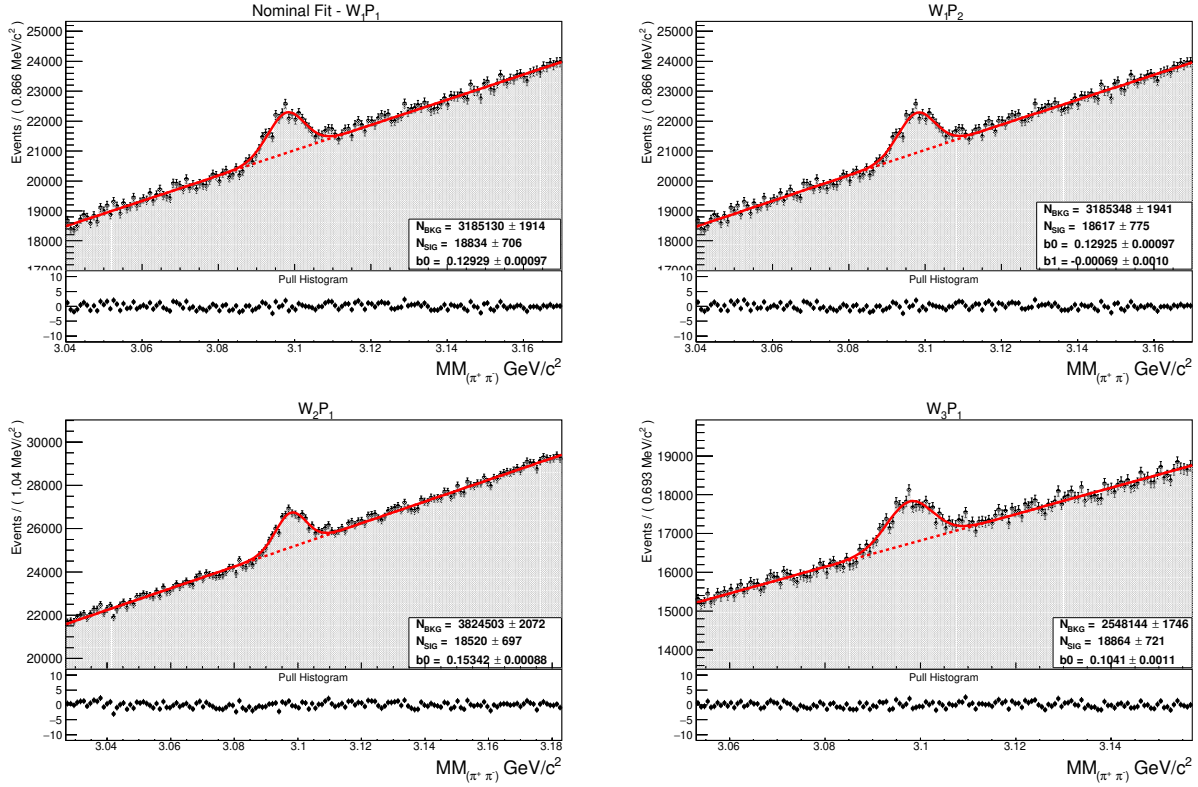

Figure 5.1: Top Left: The nominal fit W_1P_1 of J/ψ in the missing mass recoiling against $\pi^+\pi^-$. Top Right: The fitted J/ψ mass distribution in the fit range W_1 where the background is described with a second order polynomial function P_2. Bottom left: The fitted J/ψ mass distribution in W_2. Bottom Right: J/ψ fitted in W_3.

The signal yields extracted in each variation for all data samples are listed in table 5.1. The combined fitting range and background shape uncertainty could be deduced using the mean devi-

ation and the relative uncertainty equations:

$$\Delta N = \frac{1}{n}\Sigma_{i=1}^{3}|N_{Sig_{W_1P_1}} - N_{Sig_{W_iP_i}}|, \tag{5.1}$$

$$\delta_{WP} = \frac{\Delta N}{N_{Sig_{W_1P_1}}}, \tag{5.2}$$

where n is the number of possible fit variations, $N_{Sig_{W_1P_1}}$ is the signal yield extracted in the nominal fit W_1P_1, δ_{WP} is the combined systematic uncertainty.

Table 5.1: The J/ψ signal yield extracted from the 8 different fit variations with the combined fit range and background shape related systematic uncertainty for different BESIII data samples.

DATAset	$N_{sig_{W1P2}}$	$N_{sig_{W1P3}}$	$N_{sig_{W2P1}}$	$N_{sig_{W3P1}}$	$N_{sig_{W2P2}}$	$N_{sig_{W3P3}}$	$N_{sig_{W3P2}}$	$N_{sig_{W2P3}}$	$\delta_{WP}(\%)$
4160	2997 ± 842	2953 ± 852	2370 ± 744	3010 ± 774	2751 ± 814	2782 ± 913	3010 ± 888	2636 ± 818	21.85
4190	1606 ± 375	1646 ± 376	1619 ± 366	1740 ± 317	1720 ± 373	1759 ± 322	1740 ± 394	1640 ± 373	4.49
4200	5850 ± 796	6312 ± 806	5159 ± 721	6047 ± 745	6094 ± 775	6215 ± 855	6047 ± 829	5743 ± 780	8.44
4210	9467 ± 755	9448 ± 759	9269 ± 686	9071 ± 706	9589 ± 735	9002 ± 796	9071 ± 787	9563 ± 737	2.20
4220	13116 ± 755	13475 ± 765	13303 ± 685	13439 ± 707	13433 ± 735	13527 ± 810	13439 ± 786	13386 ± 739	1.43
4230	37816 ± 1151	37978 ± 1166	37098 ± 1032	37796 ± 1070	38044 ± 1117	37470 ± 1243	37346 ± 1205	38294 ± 1124	0.89
4237	18617 ± 775	18766 ± 784	18520 ± 697	18864 ± 721	18878 ± 753	18940 ± 834	18547 ± 811	19069 ± 757	0.86
4245	1861 ± 251	1844 ± 254	1954 ± 225	1878 ± 233	1903 ± 244	1891 ± 271	1893 ± 263	1891 ± 245	3.20
4246	18264 ± 797	18204 ± 807	17651 ± 711	18190 ± 737	18269 ± 772	17553 ± 862	17549 ± 837	18350 ± 776	2.02
4260	20708 ± 898	20820 ± 908	20733 ± 829	21113 ± 858	21366±895	21372 ± 991	20963 ± 964	21315±900	3.68
4270	12592 ± 811	12895 ± 827	12881 ± 715	12847 ± 746	13041 ± 783	13117 ± 894	12990 ± 855	13278 ± 790	2.18
4280	3575 ± 437	3576 ± 445	3341 ± 389	3412 ± 420	3520 ± 423	3562 ± 419	3390 ± 390	3562 ± 427	4.20
4290	10438 ± 751	10528 ± 755	9785 ± 662	10186 ± 687	10699 ± 725	10432 ± 804	10652 ± 794	10725 ± 726	3.59
4310	361 ± 84	448 ± 84	392 ± 212	376 ± 212	366 ± 244	398 ± 257	341 ± 244	428 ± 257	17.80
4315	8828 ± 744	8820 ± 755	8057 ± 656	8525 ± 683	8945 ± 719	8792 ± 813	8868 ± 786	9004 ± 723	4.44
4340	5979 ± 579	6003 ± 582	5238 ± 534	5792 ± 547	6247 ± 566	6031 ± 608	5929 ± 600	6031 ± 568	7.08
4360	6206 ± 748	6014 ± 756	4699 ± 664	5550 ± 691	6372 ± 691	6121 ± 814	6159 ± 793	6370 ± 730	17.48
4380	4275 ± 714	4355 ± 721	2532 ± 636	3306 ± 659	4142 ± 691	4769 ± 764	4714 ± 753	4198 ± 695	42.28
4390	103 ± 249	179 ± 255	123 ± 218	173 ± 228	123 ± 239	122 ± 278	83 ± 262	154 ± 242	21.08
4400	1957 ± 392	1964 ± 394	1592 ± 377	1859 ± 382	1983 ± 387	2039 ± 402	2074 ± 398	2037 ± 389	16.73
4420	2972 ± 893	2916 ± 919	1458 ± 814	2299 ± 845	2929 ± 871	3282 ± 985	2677 ± 926	2877 ± 884	41.58
4440	1308 ± 585	1307 ± 588	1094 ± 538	1295 ± 552	1542 ± 572	1294 ± 614	1278 ± 606	1294 ± 614	8.71
4470	572 ± 268	466 ± 271	571 ± 242	597 ± 250	540 ± 260	355 ± 288	512 ± 279	504 ± 262	10.86
4530	710 ± 331	714 ± 340	562 ± 353	408 ± 297	799 ± 316	913 ± 380	903 ± 355	813 ± 320	163.68
4575	492 ± 211	382 ± 217	292 ± 178	331 ± 189	500 ± 201	415 ± 243	465 ± 227	438 ± 204	28.76

For the majority of the data samples where J/ψ was observed dominantly in the missing mass, such as, the 4230 and 4237 data samples, the combined systematic errors are sufficiently small. On the other hand, in data samples where there was no observation of a J/ψ, for example the 4530, the systematic error increased tremendously. However, this is expected in cases where the signal shape is not described properly.

For the $e^+e^- \to h_c\pi^+\pi^-$ decay channel :

Similar to the previous decay channel, different fit windows and polynomial orders are introduced in order to extract the systematic error. The nominal fitting range of the h_c meson in the missing mass recoiling against two charged pions is W_1: [3.45, 3.6], the distribution is fitted with two additional ranges W_2: [3.465, 3.585] and W_3: [3.435, 3.615].

The background is described with a Chebyshev polynomial function of the second order($P2$) in the nominal fit. The order of the polynomial is varied to three ($P3$) and four ($P4$). The signal yield for the different variations of the fit window and background polynomial order are shown in table 5.2. As an example, three out of the eight fit variations are shown in figure 5.2 for the 4.246 GeV sample.

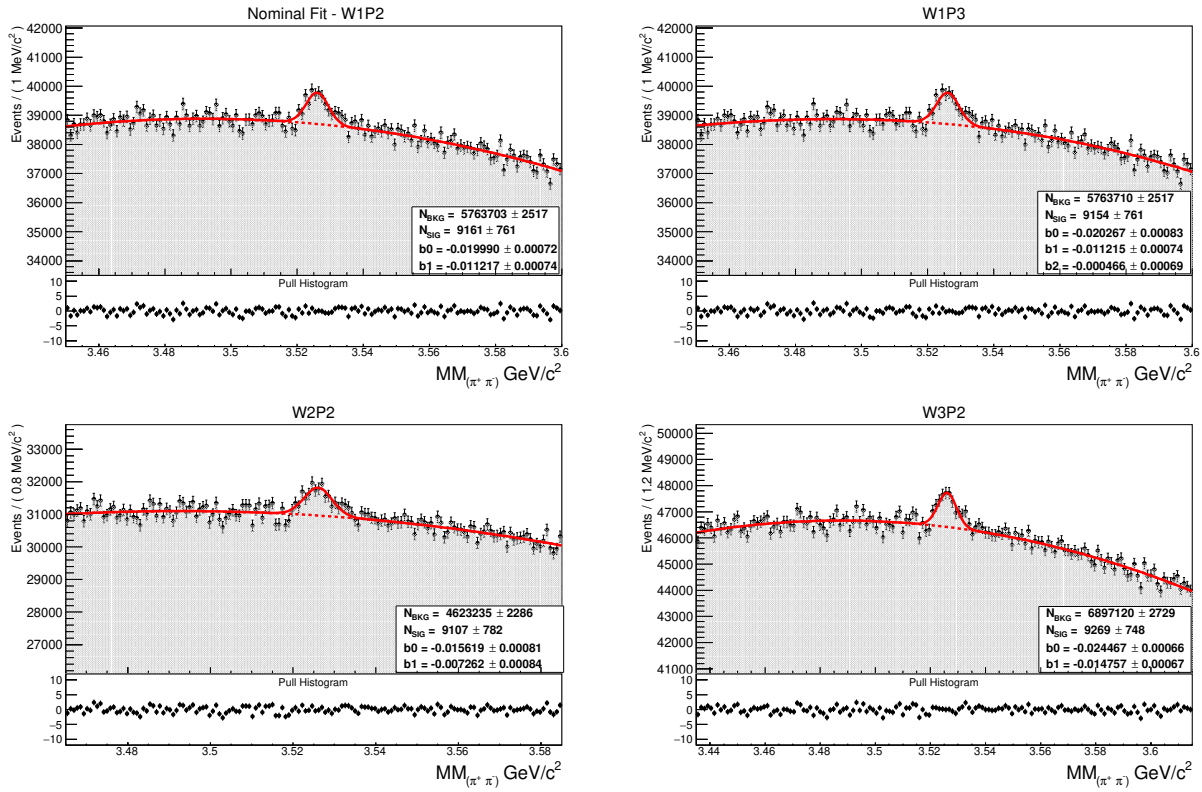

Figure 5.2: Top Left: The nominal fit W_1P_2 of h_c in the missing mass recoiling against $\pi^+\pi^-$. Top Right: The fitted h_c mass distribution in the fit range W_1 where the background is described with a third order polynomial function P_3. Bottom left: The fitted h_c mass distribution in W_2. Bottom Right: h_c fitted in W_3.

The data samples with the biggest background shape and fit range systematic uncertainty contributions are 4530, 4575 and 4310. Similar to the J/ψ case, h_c was not observed and the signal shape was fixed for theses energies from the Monte-Carlo simulation parameters.

Table 5.2: The h_c signal yield extracted from the 8 different fit variations with the combined fit range and background shape related systematic uncertainty for different BESIII data samples.

DATAset	$N_{sig_{W1P3}}$	$N_{sig_{W1P4}}$	$N_{sig_{W2P2}}$	$N_{sig_{W3P2}}$	$N_{sig_{W2P3}}$	$N_{sig_{W3P4}}$	$N_{sig_{W3P3}}$	$N_{sig_{W2P4}}$	$\delta_{WP}(\%)$
4160	3134 ± 879	2264 ± 888	5870 ± 900	5500 ± 878	5340 ± 879	2987 ± 805	4500 ± 904	3800 ± 889	27.84
4190	3694 ± 683	3961 ± 715	3925 ± 697	3321 ± 675	3894 ± 697	3736 ± 740	3325 ± 675	4232 ± 700	6.54
4200	7063 ± 1025	6713 ± 1135	6101 ± 1071	6732 ± 996	6910 ± 1071	6058 ± 1229	6683 ± 996	7347 ± 1080	10.01
4210	5284 ± 700	5047 ± 735	5226 ± 715	5275 ± 690	5237 ± 715	5113 ± 763	5284 ± 690	5157 ± 718	1.43
4220	7968 ± 731	7382 ± 774	7741 ± 750	7866 ± 720	7753 ± 750	7092 ± 807	7877 ± 720	7705 ± 753	3.54
4230	22743 ± 1242	21808 ± 1344	22011 ± 1285	23587 ± 1215	22011 ± 1285	21441 ± 1378	23550 ± 1215	21949 ± 1294	3.42
4237	9914 ± 881	10146 ± 978	9878 ± 872	10246 ± 833	9866 ± 881	10088 ± 978	10249 ± 833	9718 ± 887	1.70
4245	959 ± 234	1036 ± 248	1020 ± 220	990 ± 220	979 ± 220	1002 ± 220	1095 ± 220	939 ± 220	5.00
4246	9154 ± 761	9121 ± 810	9107 ± 782	9269 ± 748	9091 ± 782	9034 ± 849	9267 ± 748	8899 ± 786	1.06
4260	11612 ± 949	11386 ± 1013	11580 ± 977	12045 ± 932	11580 ± 977	10910 ± 1065	12051 ± 932	11614 ± 982	2.26
4270	7142 ± 704	7292 ± 745	7344 ± 722	7087 ± 693	7341 ± 722	6964 ± 777	7201 ± 725	7089 ± 693	6.31
4280	2174 ± 444	1860 ± 475	2087 ± 457	2142 ± 436	2060 ± 458	1805 ± 500	2158 ± 436	2101 ± 460	21.73
4310	764 ± 299	900 ± 335	2052 ± 460	770 ± 111	770 ± 111	770 ± 111	770 ± 111	770 ± 111	25.73
4360	8525 ± 990	8393 ± 778	8559 ± 950	8798 ± 717	8540 ± 1000	8287 ± 816	8776 ± 717	8690 ± 755	22.26
4390	1301 ± 730	1147 ± 730	1236 ± 917	1348 ± 278	1233 ± 874	1079 ± 1411	1342 ± 278	1222 ± 295	12.27
4420	20568 ± 284	20698 ± 306	20549 ± 980	21017 ± 1205	20514 ± 984	20720 ± 984	20880 ± 1206	20337 ± 987	0.82
4470	621 ± 1231	673 ± 1325	619 ± 125	537 ± 381	610 ± 340	620 ± 450	530 ± 380	672 ± 324	7.06
4530	324 ± 948	504 ± 426	359 ± 340	238 ± 256	352 ± 332	334 ± 376	227 ± 563	192 ± 342	43.17
4575	146 ± 221	222 ± 230	194 ± 221	120 ± 209	198 ± 220	203 ± 243	145 ± 209	191 ± 222	28.79

For the $e^+e^- \to D^0\bar{D}^0$ decay channel :

The nominal fitting range of the D^0-meson in the missing mass recoiling against a $\bar{D}^0$ is W_1: [1.8, 1.95], the distribution is fitted in two other ranges W_2: [1.785,1.965] and W_3: [1.815,1.935].
The background is described with a polynomial function of the first order($P1$) in the nominal fit. We do not expect a large amount of background events in this decay channel as the previous channels. Not to mention, the background shape in this case is more linear. Because of that, the order of the polynomial is varied only to three ($P3$) and we will have five instead of eight fit variations. The signal yields and the systematic uncertainty are shown in table 5.3. As an example, three out of the six fit variations are shown in figure 5.3 for the 4.22 GeV sample.
The combined systematic uncertainties for this decay channels are generally bigger than the ones in $e^+e^- \to (J/\psi, h_c)\pi^+\pi^-$. This could be due to the fact that the background subtraction approach was not used here to extract the signal shape's parameters.

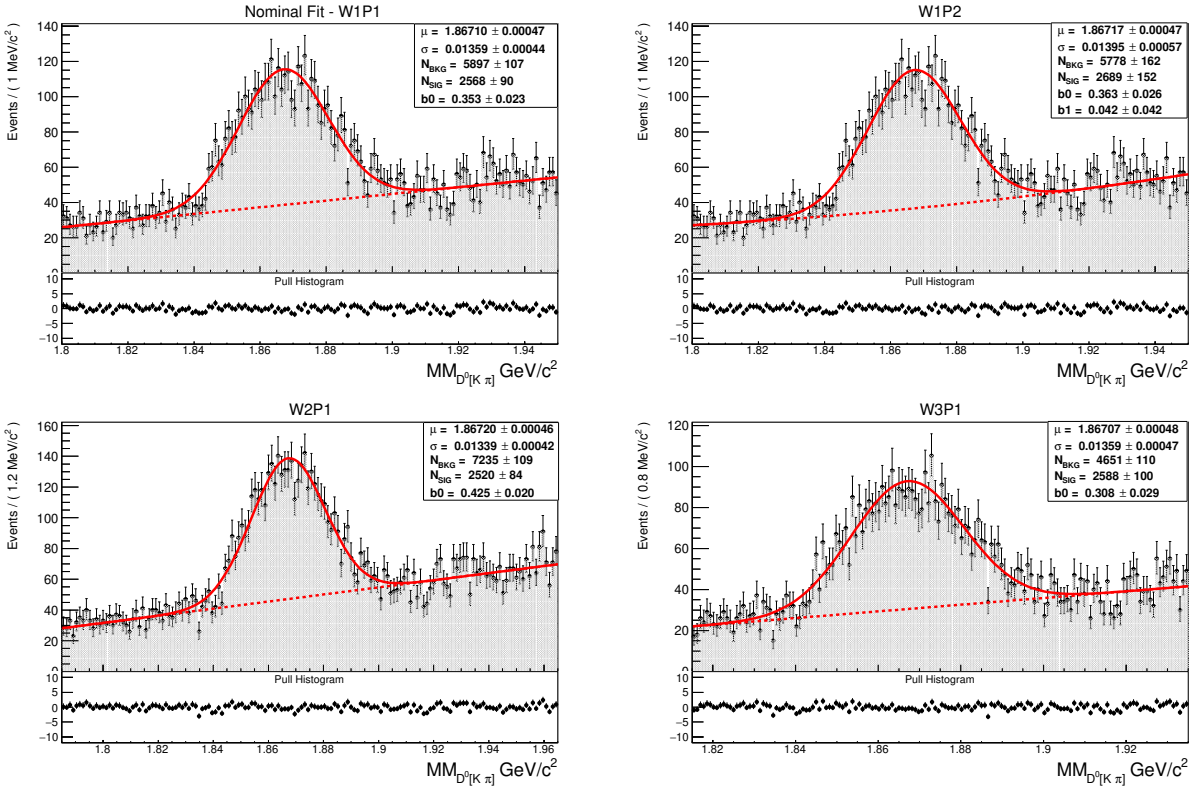

Figure 5.3: Top Left: The nominal fit W_1P_1 of D^0 in the missing mass. Top Right: The fitted D^0 mass distribution in the fit range W_1 where the background is described with a second order polynomial function P_2. Bottom left: The fitted D^0 mass distribution in W_2. Bottom Right: D^0 fitted in W_3.

Table 5.3: The D^0-meson signal yield extracted from the 5 different fit variations with the combined fit range and background shape related systematic uncertainty for different BESIII data samples.

DATAset	$N_{sig_{W1P2}}$	$N_{sig_{W2P1}}$	$N_{sig_{W3P1}}$	$N_{sig_{W2P2}}$	$N_{sig_{W3P2}}$	$\delta_{WP}(\%)$
4130	3988 ± 152	3945 ± 93	4021 ± 109	4026 ± 126	4157 ± 223	1.71
4160	2855 ± 176	2390 ± 82	2563 ± 102	2736 ± 129	2780 ± 251	9.66
4190	3642 ± 175	3077 ± 90	3211 ± 109	3391 ± 134	4067 ± 299	12.17
4200	3736 ± 183	3190 ± 91	3335 ± 110	3501 ± 135	3793 ± 267	9.25
4210	3196 ± 161	3085 ± 89	3205 ± 109	3261 ± 133	3041 ± 221	2.78
4220	2689 ± 152	2520 ± 84	2588 ± 100	2691 ± 125	3020 ± 260	5.95
4230	4901 ± 226	4394 ± 115	4604 ± 140	4699 ± 173	4597 ± 302	4.82
4237	1348 ± 111	1410 ± 73	1378 ± 82	1320 ± 93	1412 ± 158	2.33
4245	104 ± 36	84 ± 19	101 ± 25	110 ± 34	72 ± 28	11.48
4246	1572 ± 144	1310 ± 73	1392 ± 90	1405 ± 107	1789 ± 256	12.73
4260	1783 ± 139	1675 ± 82	1682 ± 94	1805 ± 118	1869 ± 193	4.43
4270	1540 ± 167	1124 ± 69	1205 ± 88	1289 ± 109	1616 ± 259	19.26
4280	452 ± 108	359 ± 41	382 ± 51	510 ± 98	460 ± 139	13.79
4290	961 ± 135	763 ± 61	859 ± 78	892 ± 99	849 ± 156	9.68
4310	69 ± 19	68 ± 17	72 ± 22	152 ± 96	173 ± 199	50.66
4315	974 ± 136	802 ± 66	904 ± 83	917 ± 107	891 ± 204	10.08
4340	707 ± 115	760 ± 67	845 ± 85	780 ± 123	733 ± 314	5.88
4360	1149 ± 126	1140 ± 70	1200 ± 96	1277 ± 125	1242 ± 52	4.16
4380	1609 ± 192	1229 ± 25	1438 ± 36	1537 ± 42	1656 ± 451	17.87
4390	171 ± 215	163 ± 76	163 ± 95	160 ± 127	149 ± 294	3.89
4400	2400 ± 150	1937 ± 111	2035 ± 139	2171 ± 164	2161 ± 171	7.52
4420	4000 ± 92	4186 ± 85	4085 ± 108	3915 ± 134	3823 ± 90	2.90
4440	2050 ± 31	2175 ± 33	2098 ± 50	2043 ± 51	1981 ± 27	4.47
4470	362 ± 12	359 ± 54	379 ± 41	340 ± 54	346 ± 12	3.12
4530	182 ± 0	177 ± 10	242 ± 11	182 ± 11	272 ± 0	19.12
4570	37 ± 12	35 ± 10	43 ± 11	34 ± 11	37 ± 12	7.36

For the $e^+e^- \to D^{*0}\bar{D}^0$ decay channel :

The uncertainty due to the fitting range of D^{*0} in the missing mass is estimated by changes of the signal yield in two different ranges $W_2 : [1.961, 2.049]$ and $W_3 : [1.955, 2.055]$ instead of the nominal fitting range $W_1 : [1.95, 2.06]$. The background shape is described in the nominal fit with a second order polynomial, the uncertainty due to the background shape is estimated increasing the polynomial function by one order. Just like the previous decay channel, we expect to have in this case five fit variations. The estimated signal yields are shown in table 5.4 and the distributions of three variations are shown as an example in figure 5.4.

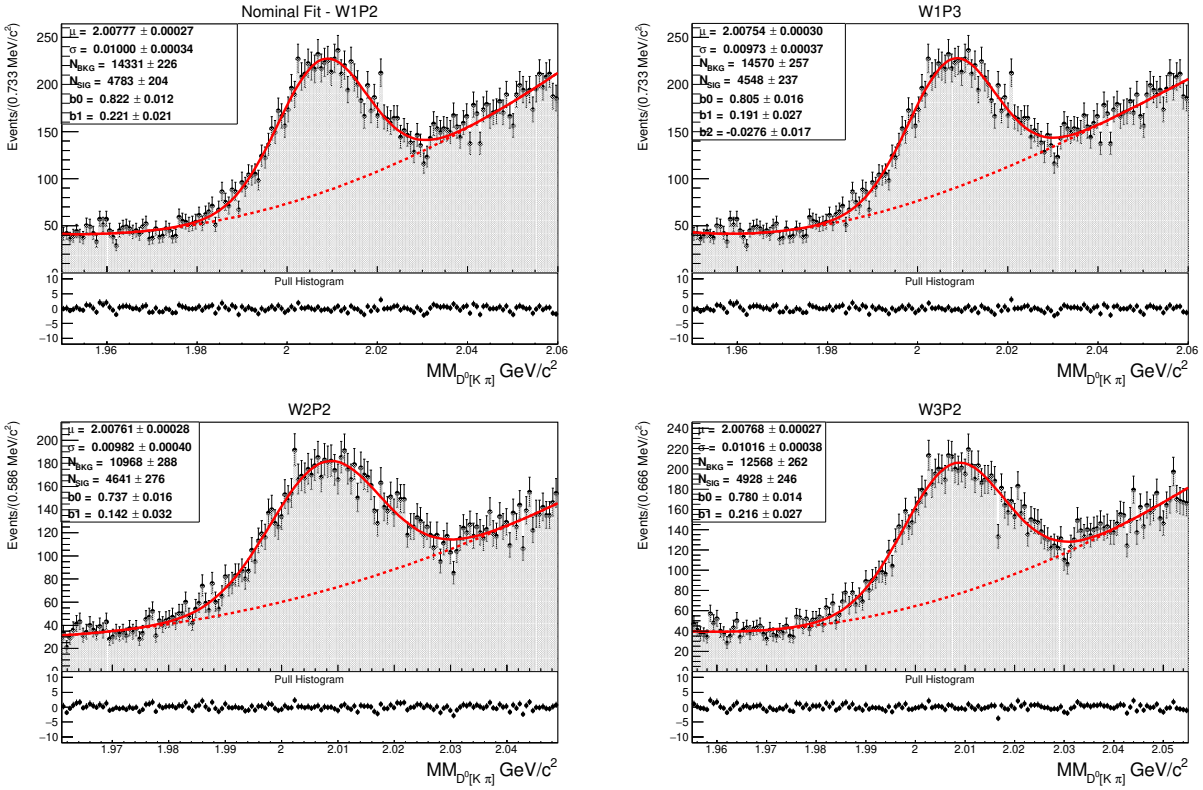

Figure 5.4: Top Left: The nominal fit W_1P_2 of D^{*0} in the missing mass. Top Right: The fitted D^0 mass distribution in the fit range W_1 where the background is described with a third order polynomial function P_3. Bottom left: The fitted D^0 mass distribution in W_2. Bottom Right: D^0 fitted in W_3.

Table 5.4: The D^{*0}-meson signal yield extracted from the 5 different fit variations with the combined fit range and background shape related systematic uncertainty for different BESIII data samples.

DATAset	$N_{sig_{W1P3}}$	$N_{sig_{W2P2}}$	$N_{sig_{W3P2}}$	$N_{sig_{W2P3}}$	$N_{sig_{W3P3}}$	$delta_{WP}(\%)$
4130	4428 ± 196	6062 ± 280	6343 ± 255	4948 ± 301	4765 ± 236	18.48
4160	4676 ± 222	5799 ± 304	6157 ± 268	5180 ± 372	5161 ± 289	11.33
4190	5602 ± 259	6832 ± 408	6797 ± 308	5944 ± 423	5898 ± 323	8.57
4200	5412 ± 250	6023 ± 336	6014 ± 270	5786 ± 390	5245 ± 271	7.76
4210	4635 ± 258	4680 ± 296	4943 ± 257	4111 ± 314	4394 ± 275	10.61
4220	4548 ± 237	4641 ± 276	4928 ± 246	4691 ± 377	4613 ± 283	3.28
4230	9425 ± 330	9740 ± 396	9463 ± 305	9714 ± 517	9700 ± 399	1.29
4237	4448 ± 213	4390 ± 256	4468 ± 212	4627 ± 338	4737 ± 274	2.44
4245	615 ± 85	532 ± 97	566 ± 82	615 ± 147	586 ± 103	5.15
4246	4962 ± 247	4836 ± 287	4878 ± 232	5145 ± 425	4981 ± 299	33.31
4260	8252 ± 332	7979 ± 393	7940 ± 302	9005 ± 637	8621 ± 423	4.82
4270	5194 ± 249	5484 ± 379	5157 ± 249	5445 ± 442	5385 ± 316	6.34
4280	1671 ± 151	1452 ± 175	1550 ± 149	1708 ± 257	1711 ± 187	8.44
4290	4406 ± 294	3929 ± 298	4377 ± 273	4397 ± 555	4753 ± 421	6.81
4310	471 ± 151	376 ± 119	345 ± 73	262 ± 79	343 ± 107	18.09
4315	4969 ± 355	4333 ± 380	4532 ± 303	4149 ± 470	4697 ± 408	6.27
4340	4725 ± 349	3763 ± 325	4100 ± 275	3899 ± 458	4803 ± 472	9.30
4360	5862 ± 394	5419 ± 545	5333 ± 339	5958 ± 886	5707 ± 489	7.26
4380	5549 ± 733	4604 ± 295	4788 ± 242	4408 ± 301	4848 ± 866	15.79
4390	605 ± 128	529 ± 140	510 ± 96	560 ± 193	477 ± 110	7.46
4400	3843 ± 361	4176 ± 249	4226 ± 198	2900 ± 500	3562 ± 436	12.40
4420	10654 ± 492	9465 ± 610	9428 ± 424	10681 ± 965	10077 ± 574	5.86
4440	5709 ± 421	5874 ± 742	5403 ± 405	5906 ± 1014	6301 ± 693	9.93
4470	996 ± 224	992 ± 284	798 ± 134	645 ± 218	667 ± 184	19.25
4530	1025 ± 286	644 ± 238	914 ± 270	527 ± 151	1100 ± 443	20.82
4570	430 ± 162	180 ± 53	260 ± 93	187 ± 93	460 ± 158	38.26

2 Total Systematic Uncertainties

The total uncertainty for the Born cross sections listed in the previous chapter for the different decay channels are obtained from the quadratic sum of all the above mentioned contributions.

$$\delta_{Total} = \sqrt{\delta_{WP}^2 + \delta_{Tr}^2 + \delta_{PID}^2 + \delta_{L}^2} \tag{5.3}$$

The total systematic uncertainty values $\delta_{Total}(J/\psi)$, $\delta_{Total}(h_c)$, $\delta_{Total}(D)$ and $\delta_{Total}(D^*)$ of the four decay channels $e^+e^- \to J/\psi\pi^+\pi^-$, $e^+e^- \to J/\psi\pi^+\pi^-$, $e^+e^- \to D^0\bar{D}^0$ and $e^+e^- \to D^{0*}\bar{D}^0$ are shown respectively in the tables 5.5, 5.6 and 5.7. As evident by the values listed in these tables, the total systematic uncertainties are strongly dominated by the fitting range and background shape related systematics.

Table 5.5: The different systematic contributions and total systematic uncertainties of $e^+e^- \to J/\psi\pi^+\pi^-$ for the XYZ BESIII data samples.

DATAset	$\delta_{Tr}(\%)$	$\delta_L(\%)$	$\delta_{PID}(\%)$	$\delta_{WP}(J/\psi)(\%)$	$\delta_{Total}(J/\psi)(\%)$
4160	2	1	2	21.85	22.06
4190	2	1	2	4.49	5.40
4200	2	1	2	8.44	8.96
4210	2	1	2	2.20	3.72
4220	2	1	2	1.43	3.32
4230	2	1	2	0.89	3.13
4237	2	1	2	0.86	3.12
4245	2	1	2	3.20	4.38
4246	2	1	2	2.02	3.61
4260	2	1	2	3.68	4.75
4270	2	1	2	2.18	3.71
4280	2	1	2	4.20	5.16
4290	2	1	2	3.59	4.68
4310	2	1	2	17.80	18.05
4315	2	1	2	4.44	5.36
4340	2	1	2	7.08	7.69
4360	2	1	2	17.48	17.73
4380	2	1	2	42.28	42.38
4390	2	1	2	21.08	21.29
4400	2	1	2	16.73	17.00
4420	2	1	2	41.58	41.69
4440	2	1	2	8.71	9.22
4470	2	1	2	10.86	11.26
4530	2	1	2	163.68	163.71
4575	2	1	2	28.76	28.92

Table 5.6: The different systematic contributions and total systematic uncertainties of $e^+e^- \to h_c\pi^+\pi^-$ for the XYZ BESIII data samples.

DATAset	$\delta_{Tr}(\%)$	$\delta_L(\%)$	$\delta_{PID}(\%)$	$\delta_{WP}(h_c)(\%)$	$\delta_{Total}(h_c)(\%)$
4160	2	1	2	27.84	28.00
4190	2	1	2	6.54	7.19
4200	2	1	2	10.01	10.45
4210	2	1	2	1.43	3.33
4220	2	1	2	3.54	4.64
4230	2	1	2	3.42	4.55
4237	2	1	2	1.70	3.45
4245	2	1	2	5.00	5.83
4246	2	1	2	1.06	3.18
4260	2	1	2	2.26	3.75
4270	2	1	2	6.31	6.99
4280	2	1	2	21.73	21.93
4310	2	1	2	25.73	25.90
4360	2	1	2	22.26	22.46
4390	2	1	2	12.27	12.64
4420	2	1	2	0.82	3.11
4470	2	1	2	7.06	7.67
4530	2	1	2	43.17	43.28
4575	2	1	2	28.79	28.94

Table 5.7: The different systematic contributions and total systematic uncertainties of $e^+e^- \to D^0\bar{D}^0$ and $e^+e^- \to D^{*0}\bar{D}^0$ for all data samples.

DATAset	$\delta_{Tr}(\%)$	$\delta_L(\%)$	$\delta_{PID}(\%)$	$\delta_{WP}(D^*)(\%)$	$\delta_{WP}(D)(\%)$	$\delta_{Total}(D^*)(\%)$	$\delta_{Total}(D)(\%)$
4160	2	1	2	11.33	9.66	11.72	10.11
4190	2	1	2	8.57	12.17	9.08	12.53
4200	2	1	2	7.76	9.25	8.31	9.73
4210	2	1	2	10.61	2.78	11.07	4.09
4220	2	1	2	3.28	5.95	4.44	6.66
4230	2	1	2	1.29	4.82	3.26	5.68
4237	2	1	2	2.44	2.33	3.86	3.79
4245	2	1	2	5.15	11.48	5.95	11.87
4246	2	1	2	33.31	12.73	33.44	13.08
4260	2	1	2	4.82	4.43	5.68	5.35
4270	2	1	2	6.34	19.26	7.01	19.49
4280	2	1	2	8.44	13.79	8.96	14.11
4290	2	1	2	6.81	9.68	7.44	10.14
4310	2	1	2	18.09	50.66	18.33	50.75
4315	2	1	2	6.27	10.08	6.94	10.52
4340	2	1	2	9.30	5.88	9.76	6.60
4360	2	1	2	7.26	4.16	7.85	5.13
4380	2	1	2	15.79	17.87	15.95	18.12
4390	2	1	2	7.46	3.89	8.04	4.91
4400	2	1	2	12.40	7.52	12.75	8.09
4420	2	1	2	5.86	2.90	6.58	4.17
4440	2	1	2	9.93	4.47	10.37	5.38
4470	2	1	2	19.25	3.12	19.48	4.33
4530	2	1	2	20.82	19.12	21.03	19.35
4575	2	1	2	38.26	7.36	38.38	7.95

SUMMARY

Many charmonium-like XYZ states have been discovered experimentally in the previous years. The $Y(4260)$ is one of the most intriguing charmonium-like state. Possible $Y(4260)$ decay channels have been investigated with the BESIII experiment in order to shed more light on the nature of this state. For this analysis, we used the missing mass technique to explore the BESIII data and the possible decay patterns of the $Y(4260)$. We studied inclusively the processes $e^+e^- \to J/\psi\pi^+\pi^-$, $h_c\pi^+\pi^-$, $\psi(2S)\pi^+\pi^-$, $D^0\bar{D}^0$, $D^*(2007)^0\bar{D}^0$, $J/\psi K^+K^-$ based on the XYZ data samples collected between 2013 and 2019 with the BESIII detector at center of mass energies above 4 GeV. In this analysis, more XYZ energy points have been analyzed than in previous exclusive analyses of these channels performed at BESIII. This allowed us to provide an up-to-date precise description of the inclusive energy dependent cross sections. The most interesting results appeared in the $\pi^+\pi^-$ recoil system. Two resonant structures are observed in the inclusive energy dependent cross sections of $e^+e^- \to h_c\pi^+\pi^-$ and $e^+e^- \to J/\psi\pi^+\pi^-$, which is consistent with the exclusive studies at BESIII performed previously. In the $J/\psi\pi^+\pi^-$ case, the positions of the resonances in both studies are almost identical, with the second Breit-Wigner, the so called $Y(4320)$ appearing to be 35 MeV wider in the inclusive analysis. In the h_c case, the first resonance is found to be 5 MeV wider in the inclusive study, while the second resonance is roughly 30 MeV narrower with a slight shift in the positions. In the case of the open charm decay channels, $e^+e^- \to D^0/D^*(2007)\bar{D}^0$, two resonant structures appeared in the cross section line shape between 4.13 and 4.6 GeV. The first resonance has a mass of 4.18 GeV/c^2 and the second one of about 4.42 GeV/c^2. These structures are found to be consistent with the $\psi(4160)$ and $\psi(4415)$, observed by the BaBar and Belle Collaborations. For the other decay channels, such as $J/\psi K^+K^-$ and $\psi(2S)\pi^+\pi^-$, the J/ψ and $\psi(2S)$ are not observed in the majority of the data samples. Therefore, we are not able to provide an accurate description of the inclusive cross section's line shape. Finally, the recoil mass technique shows a great discovery potential. The main disadvantage of the inclusive analysis approach is, however, the huge amount of background. There is still some work to be done in order to make the missing mass technique fully efficient at BESIII. Background rejection techniques should be developed in order to rival the inclusive results produced by the B-meson factories such as Belle.

ZUSAMMENFASSUNG

Das Standardmodell der Elementarteilchenphysik (SM) konnte experimentelle Phänomene erfolgreich beschreiben und wurde daher allgemein als grundlegende Theorie der Elementarteilchenphysik anerkannt. Das SM ist in der Lage, drei der vier bekannten Grundkräfte im Universum (die elektromagnetischen, schwachen und starken Wechselwirkungen) zu beschreiben und alle bekannten Elementarteilchen zu klassifizieren. Trotz seines Erfolgs lässt das SM viele Fragen offen. Es beschreibt die Teilchenphysik bis zu Energien von etwa 100 GeV. Hochenergieexperimente, z.B. die Experimente am LHC Cern, zielen darauf ab, den Bereich höherer Energie zu untersuchen. Die Experimente mit niedrigerer Energie und hoher Luminosität, z.B. das BESIII-Experiment am BEPCII, können die Fragen im Zusammenhang mit dem Hadronenspektrum und der Hadron-Struktur beantworten.

Das BESIII-Experiment

Das BESIII-Experiment am BEPCII-Elektronen-Positronen-Kollider in Peking, China, ist ein internationales Teilchenphysik-Experiment, an dem 500 Mitglieder aus 72 Institutionen in 15 Ländern teilnehmen. Elektronen und Positronen werden in zwei unterschiedlichen Speicherringen beschleunigt, bevor sie bei Massenschwerpunktsenergien zwischen 2,0 und 4,6 GeV zur Kollision gebracht werden. Der BESIII-Detektor, der Haupt und einzige Detektor am BEPCII, ist direkt um den Interaktionspunkt herum aufgebaut. Innerhalb seiner schalenartigen Struktur werden eine Driftkammer, ein Flugzeitdetektor, ein elektromagnetisches Kalorimeter und ein Myonendetektor verwendet, um Partikel im Endzustand zu rekonstruieren. Das BESIII-Experiment nimmt seit 2008 Daten in der Charmonium-Massenregion. Es hat die weltweit größte Datensatz von J/ψ-Ereignissen gesammelt, sowie die größten Datensatz von $\psi(2S)$ und $\psi(3770)$. Dies bietet die einmalige Gelegenheit, entscheidende Fragen zu beantworten, die frühere Experimente aufgrund niedriger Statistiken nicht beantworten konnten. BESIII verfügt über ein breites Physikprogramm, das Charmonium- und Leicht-Hadron-Spektroskopie, Studien zu elektroschwachen und starken Wechselwirkungen, Tau-Physik und Physik jenseits des Standardmodells umfasst. Eines der Hauptziele von BESIII ist das Verständnis der Natur der XYZ-Charmonium-ähnlichen Zustände. BESIII läuft direkt in der relevanten XYZ-Massenregion, was bedeutet, dass diese Zustände mit beispielloser

Genauigkeit untersucht werden können.

Die XYZ-Charmonium-ähnlichen Zustände

Die konventionellen $c\bar{c}$-Zustände, z.B, J/ψ oder h_c, werden durch Quark-Potentialmodelle gut beschrieben. Viele charmonium-ähnliche XYZ-Zustände sind in den vergangenen Jahren experimentell von BESIII und anderen Experimenten, z.B. Belle und BaBar endeckt worden. Die experimentell entdeckten Charmonium-ähnlichen Mesonen scheinen jedoch nicht in das herkömmliche $c\bar{c}$-Spektrum zu passen. Es gibt zunehmend Hinweise darauf, dass zumindest einige dieser neuen Zustände, QCD-erlaubte exotische Zustände sind. Es werden verschiedene theoretische Interpretationen vorgeschlagen, z.B. Tetraquarks, hadronische Moleküle, Hybridzustände oder Klebebälle. Im Charmoniumspektrum unterhalb der DD-Schwelle, gibt es eine ausgezeichnete Übereinstimmung zwischen theoretischen Vorhersagen und experimentellen Beobachtungen. Allerdings ist die Region oberhalb des Schwellenwerts mit vielen unerwarteten XYZ-Zuständen gefüllt. Die bekanntesten experimentell bestätigten Zustände sind die $Z_c(3900)^{\pm}$, $Z_c(4020)^{\pm}$, $Z_c(4200)^{\pm}$ und $Z_c(4430)^{\pm}$ (die geladenen Zustände) sowie die $X(3872)$, $Y(4260)$, $Y(4360)$ und $Y(4660)$ (die neutrale Zustände).
In der vorliegenden Studie interessieren wir uns hauptsächlich für den $Y(4260)$-Zustand. Es wurde im ISR-Prozess $e^+e^- \to J/\psi\pi^+\pi^-$ von BaBaR im Jahr 2005 entdeckt und wurde von Belle im Jahr 2007 bestätigt. Es ist sehr schwierig, das $Y(4260)$ als herkömmliches Charmonium in das Spectrum aufzunehmen. Dieser Zustand, der ein Spinvektorzustand ist, liegt weit außerhalb der vorhergesagten Massen eines herkömmlichen Vektormesonen. Dieser Zustand hat eine große Zerfallsrate zum Charmoniumzustand J/ψ mit a leichtes Mesonensystem. Es hat jedoch überraschenderweise eine starke Unterdrückung von DD-Zerfällen, obwohl das $Y(4260)$ nur etwa 300 MeV über der $DD\pi$-Schwelle liegt.

Motivation dieser Arbeit

Um die Natur des $Y(4260)$-Zustands und sein Zerfallsmuster zu verstehen, wurde eine inklusive Analyse für verschiedene Rückstoßsysteme ($\pi^+\pi^-$, K^+K^-, $K^{\pm}\pi^{\mp}$ ...) durchgeführt, basierend auf den zwischen 2013 und 2019 oberhalb von 4 GeV aufgezeichneten XYZ-BESIII-Datensätzen. Für diese Analyse haben wir die "Missing Mass"-Technik verwendet, um die BESIII-Daten hinsichtlich möglicher Zerfallsmuster des $Y(4260)$ zu untersuchen. Hierfür haben wir die Prozesse $e^+e^- \to J/\psi\pi^+\pi^-$, $h_c\pi^+\pi^-$, $\psi(2S)\pi^+\pi^-$, $D^0\bar{D}^0$, $D^*(2007)^0\bar{D}^0$ und $J/\psi K^+K^-$ untersucht. Die "Missing Mass"-Technik wurde in den letzten zwei Jahrzehnten und in verschiedenen Experimenten angewendet und führte zu vielen neuen interessanten Ergebnissen. Eine der bekanntesten Entdeckungen wurde in 2013 von dem Belle-Experiment gemacht, als sie zum ersten Mal die Singulett-P-Zustände von Bottonium $h_b(1P)$ und $h_b(2P)$ im Spektrum der "Missing Mass" beobachten konnte. Diese Belle-Inclusive-Studie war eine große Motivation für diese Doktorarbeit.

Ergebnisse der Analyse

In der ersten Phase der Analyse werden Monte-Carlo-Simulationen verwendet, um Auswahlkriterien zu untersuchen und zu optimieren und die Rekonstruktionseffizienz, die Vakuumpolarisation und (ISR) Korrekturfaktoren zu extrahieren. Die untersuchten Zustände und Zerfälle wurden als Signal Monte-Carlo mit 30000 Ereignissen an allen 27 Energiepunkten unter Verwendung die Ereignisgeneratoren CONEXC und BesEvtGen simuliert. Um die Hintergrundereignisse zu reduzieren, wurden Ereignisauswahlschnitte für einige Variablen durchgeführt, z.B. POCA, Partikelidentifikation und invariante Massenschnitte. Dann wird die Signalausbeute für die verschiedenen Zerfallskanäle von dem BESIII-Datensatz abgezogen. Die Signalform wird unter Verwendung des Untergrundsubtraktionsansatzes beschrieben. Die inklusiven energieabhängigen Wirkungsquerschnitte berechnet und anschließend untersucht. Darüber hinaus werden die systematischen Unsicherheiten bezogen auf die Wirkungsquerschnittsmessungen werden berechnet. Einige der systematischen Unsicherheitsbeiträge stammen hauptsächlich aus der Luminositätmessung, Tracking, Teilchenidentifikation, Anpassungsbereich und Hintergrundform.
In dieser Analyse wurden mehr XYZ-Energiepunkte analysiert als in früheren exklusiven BESIII-Analysen dieser Kanäle. Die interessantesten Ergebnisse haben wir für das $(\pi^+\pi^-)$-Rückstoßsystem gefunden. Zwei resonante Strukturen beobachten wir in den inklusiven energieabhängigen Wirkungsquerschnitten von $e^+e^- \to h_c\pi^+\pi^-$ und $e^+e^- \to J/\psi\pi^+\pi^-$, welche mit den exklusiven BESIII-Studien übereinstimmt, die zuvor durchgeführt worden sind. Im Fall von $J/\psi\pi^+\pi^-$ sind die Positionen der Resonanzen in beiden Studien fast identisch, wobei der zweite Breit-Wigner das so genannte $Y(4320)$ beschreibt und sich mit 35 MeV etwas breiter ergibt als in der exklusiven Analyse. Im h_c-Fall ergibt sich die erste Resonanz um 5 MeV breiter in der inklusiven Studie, während die zweite Resonanz um etwa 30 MeV schmaler ist, mit einer leichten Verschiebung in den Positionen. Bei den "Open Charm"-Zerfallskanälen, $e^+e^- \to D^0/D^*(2007)^0\bar{D}^0$, werden zwei resonante Strukturen im energieabhängigen Wirkungsquerschnitt zwischen 4,13 und 4,6 GeV beobachtet. Die erste Resonanz hat eine Masse von 4,18 GeV/c^2 und die zweite von etwa 4,42 GeV/c^2. Diese Strukturen sind in Übereinstimmung mit dem $\psi(4160)$ und dem $\psi(4415)$, die von der BaBar und der Belle Kollaboration beobachtet wurden. Für die anderen Zerfallskanäle, $J/\psi K^+K^-$ und $\psi(2S)\pi^+\pi^-$, werden das J/ψ und das $\psi(2S)$ in der Mehrzahl der Datensätze nicht beobachtet. Daher sind wir hier nicht in der Lage, eine genaue Beschreibung der Linienform des inklusiven Wirkungsquerschnitten zu erhalten.

Schlussfolgerung

Wir konnten eine genaue Beschreibung der energieabhängigen Wirkungsquerschnitte von vier der sechs untersuchten Zerfallskanäle liefern, in denen einige Y-Charmonium-ähnliche Zustäde beobachtet wurden. Die "Missing Mass"-Technik erwies sich als leistungsstarke Technik zur Untersuchung der möglichen Zerfallskanäle der Y-Zustände. Sie bietet eine großes Entdeckungspotenzial. Der wesentliche Nachteil des inklusiven Analyseansatzes ist jedoch, die enorme Menge an Untergrund. Es bleibt noch einiges zu tun, um die "Missing Mass"-Technik bei BESIII noch erfolgreicher

zu machen. Techniken zur Unterdrückung des Untergrundes sollten entwickelt werden, um es mit den inklusiven Ergebnissen der B-Mesonen Fabriken wie das Belle-Experiment aufnehmen zu können.

APPENDIX

A.I Analysis of $e^+e^- \to \psi(2S)\pi^+\pi^-$

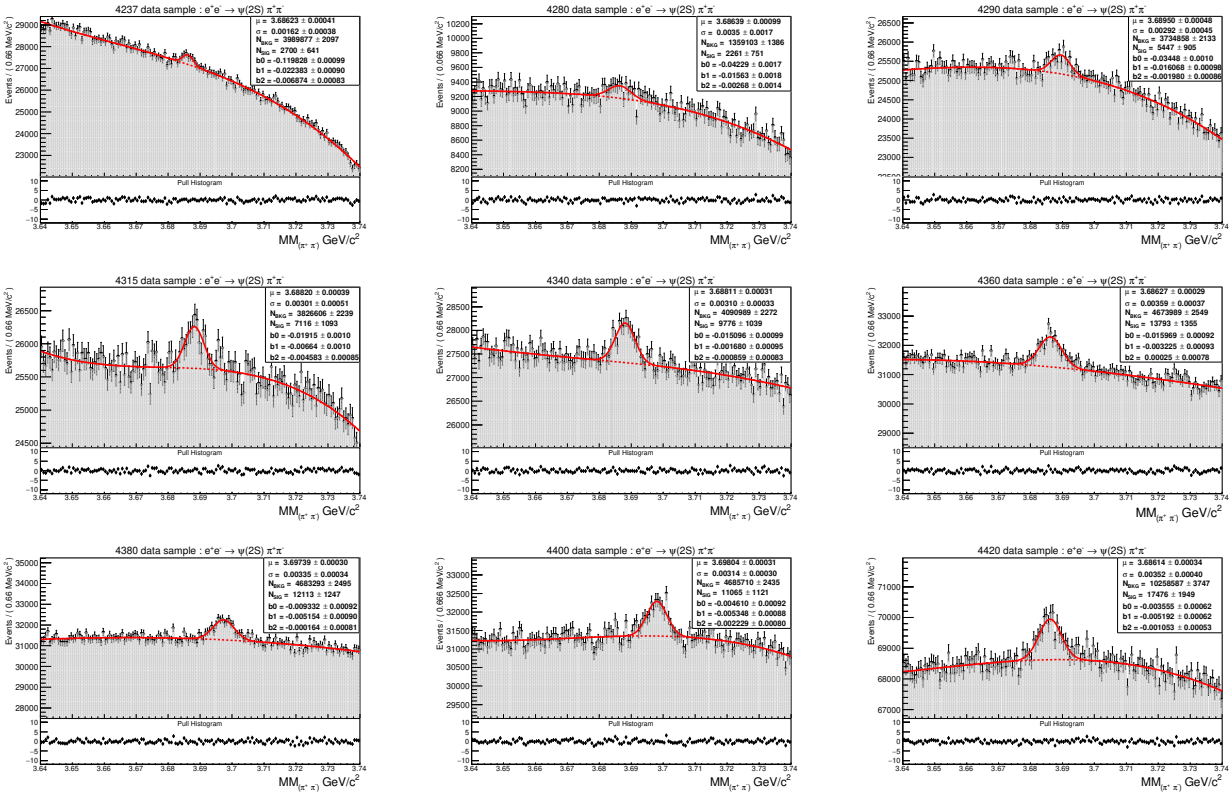

Table 5.8: The fitted missing mass distributions in the $\psi(2S)$ mass region for the BESIII XYZ data samples. The signal parameters are estimated with a chi-square fit, where the model consists of a Gaussian and a first order Chebyshev polynomial. $\psi(2S)$ appear in 9 out of all data samples.

A.I Analysis of $e^+e^- \to J/\psi\pi^+\pi^-$

A.I.1 Exclusive Analysis

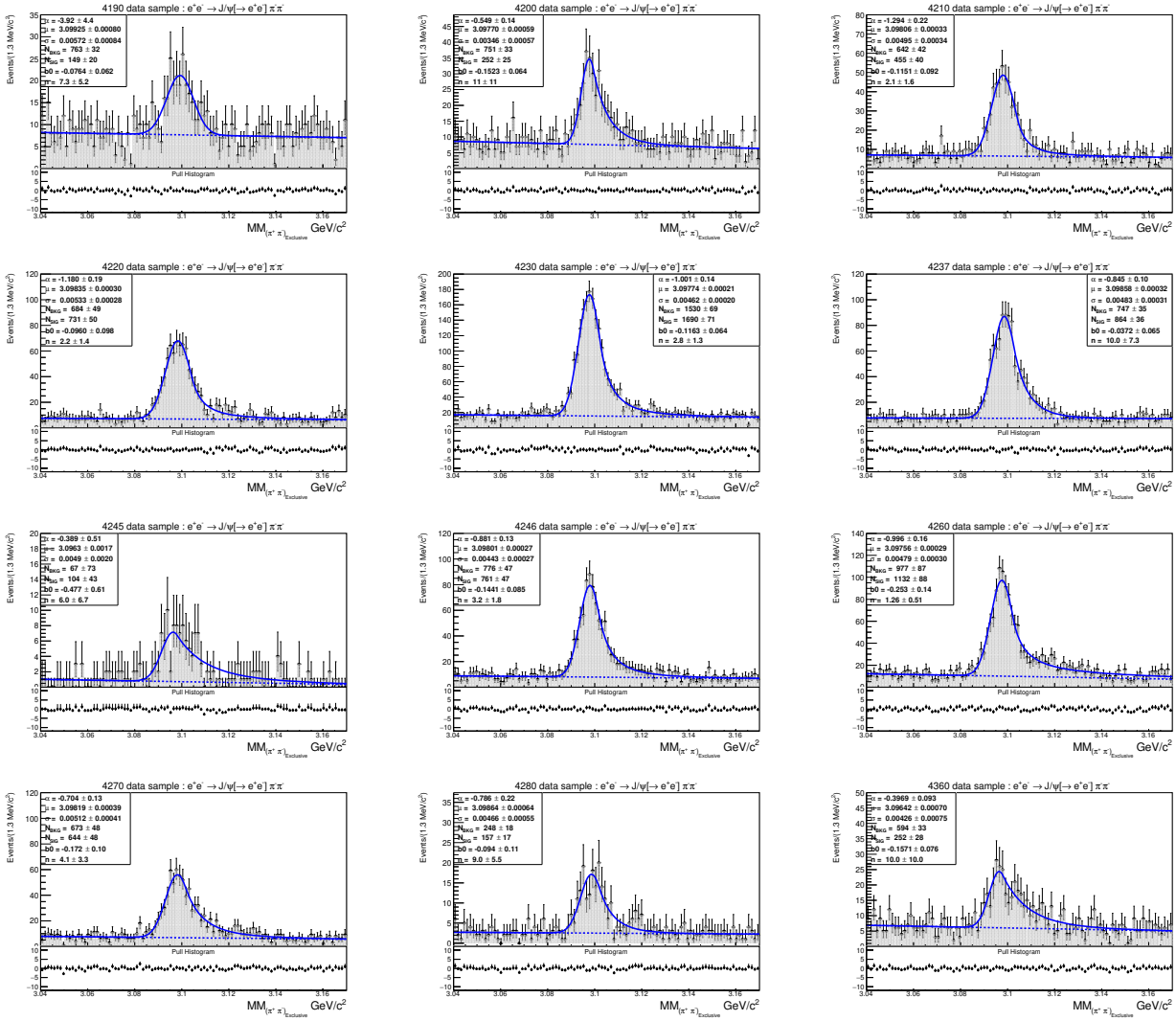

Table 5.9: The fitted exclusive missing mass distributions. In this approach, J/ψ is reconstructed from two electrons.

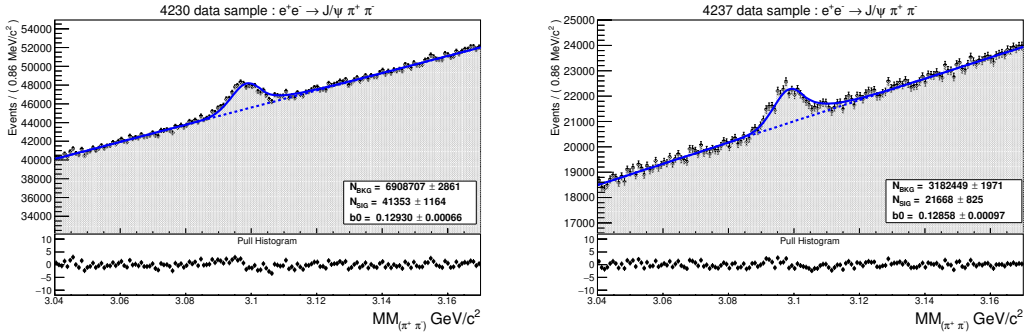

Table 5.10: The inclusive missing mass distributions for the 4230 and 4237 data samples. The J/ψ signal shape is fixed using the exclusive approach. As shown, this approach does not offer a good description of the signal.

A.I.2 Inclusive Analysis

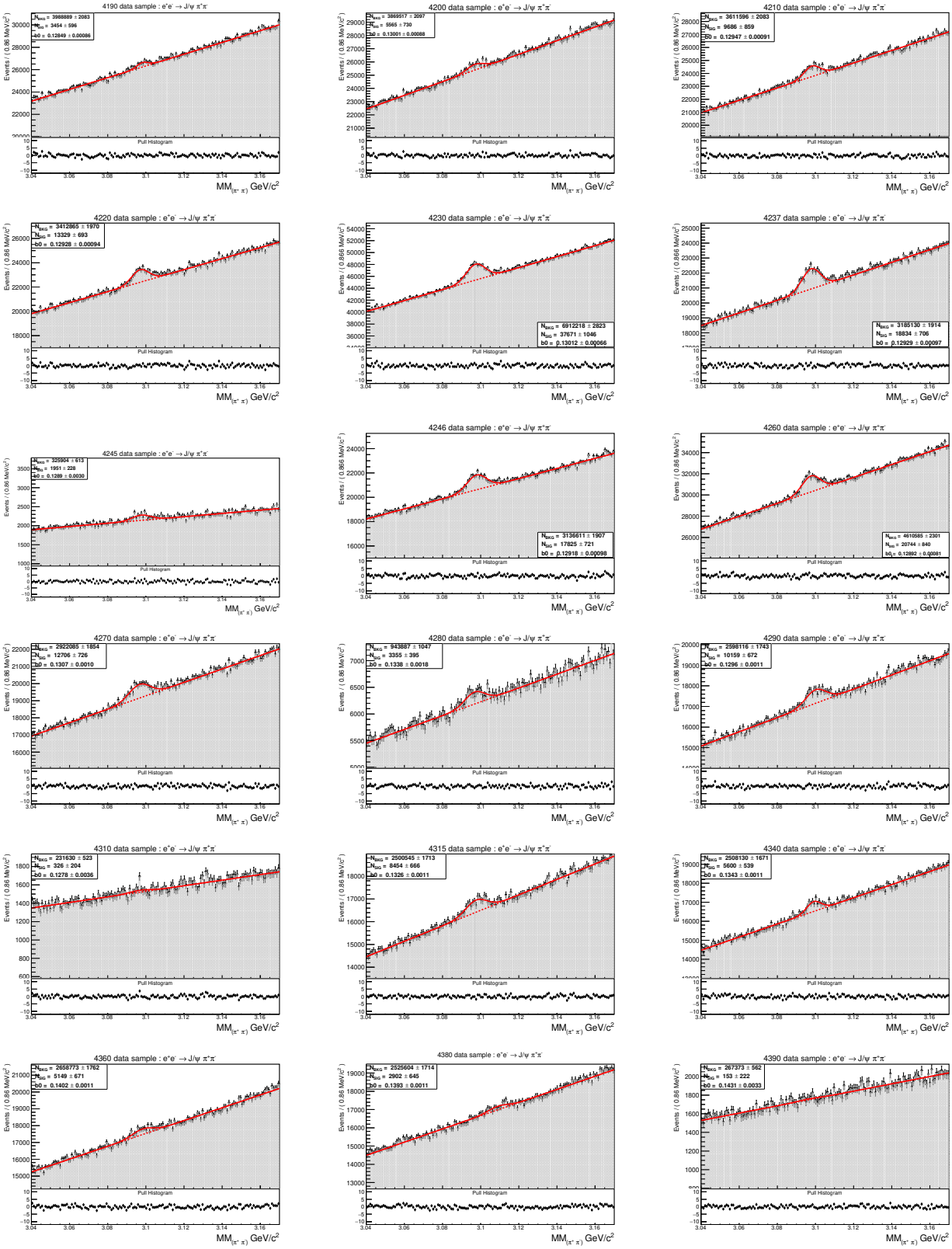

Table 5.11: The fitted inclusive missing mass distributions for the XYZ BESIII data samples in the J/ψ mass region. The J/ψ signal shape is fixed using the background subtraction approach. The signal parameters are estimated with a chi-square fit, where the model consists of a Gaussian and a first order Chebyshev polynomial.

A.I Analysis of $e^+e^- \to h_c\pi^+\pi^-$

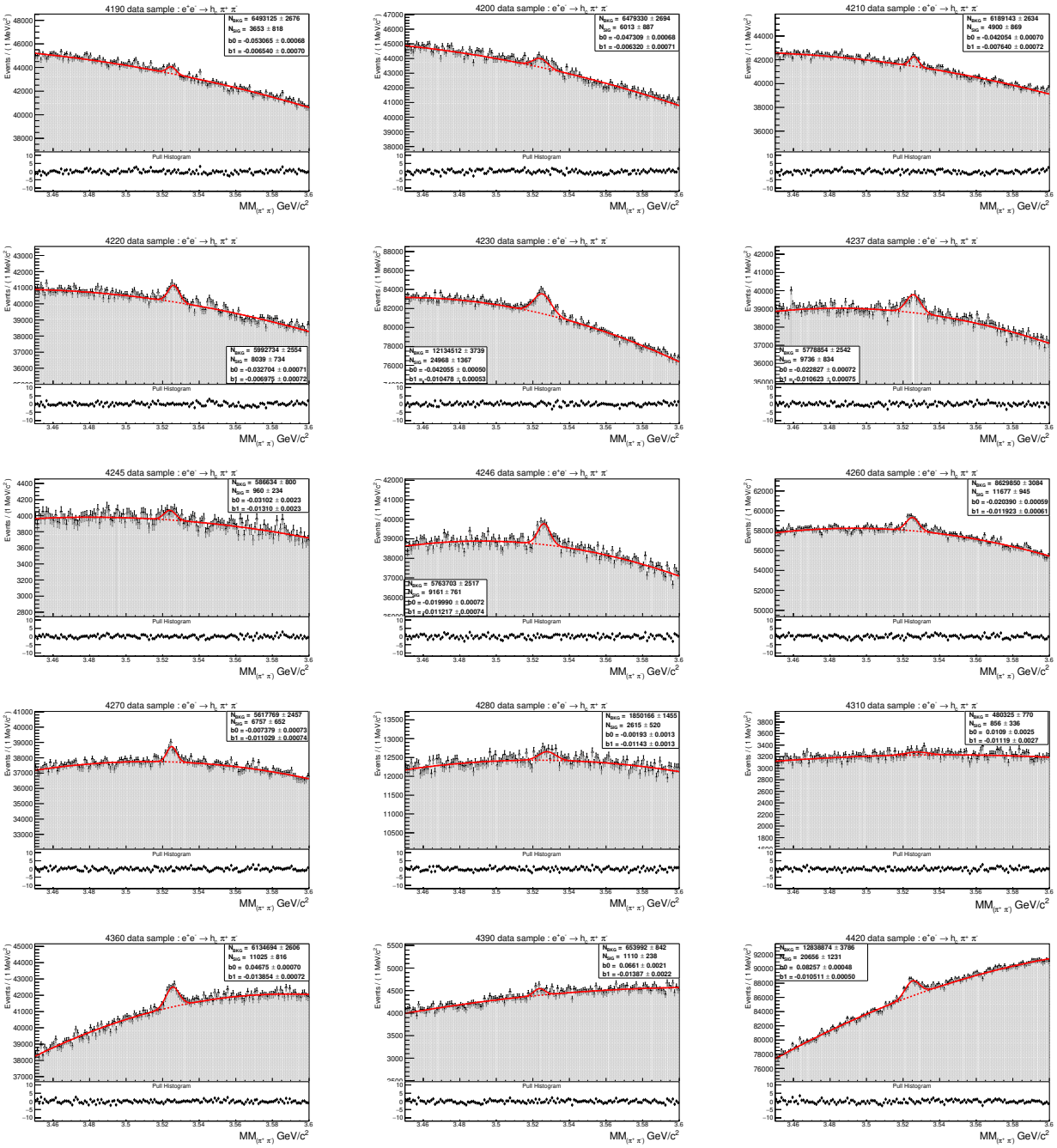

Table 5.12: The fitted inclusive missing mass distributions for the XYZ BESIII data samples in the h_c mass region. The h_c signal shape is fixed using the background subtraction approach. The signal parameters are estimated with a chi-square fit, where the model consists of a Gaussian and a second order Chebyshev polynomial.

A.I Analysis of $e^+e^- \to D^0D^0[K^\pm\pi^\mp]$

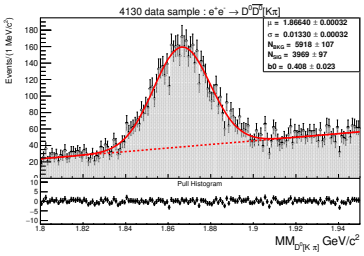

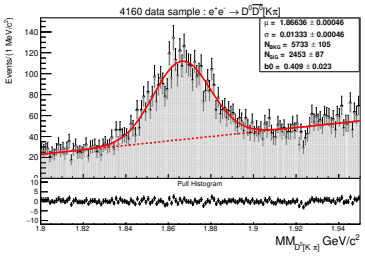

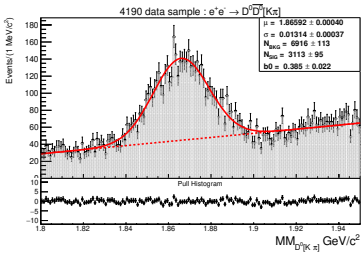

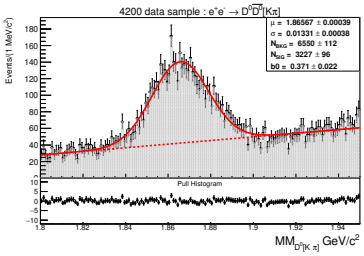

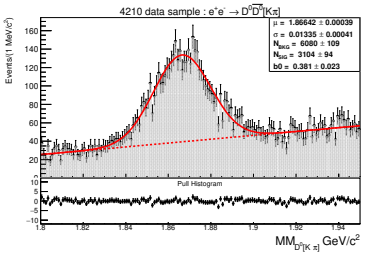

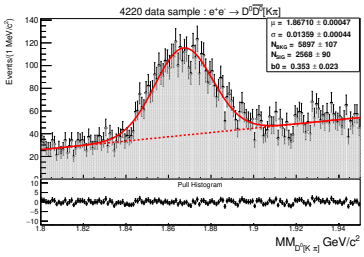

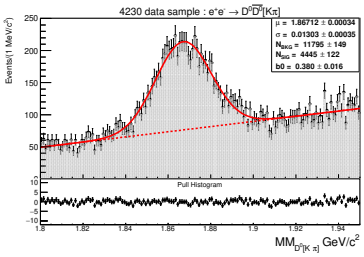

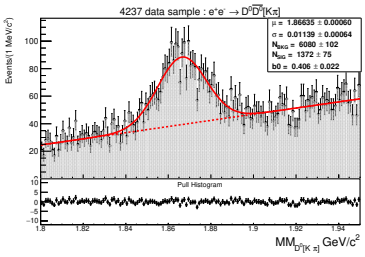

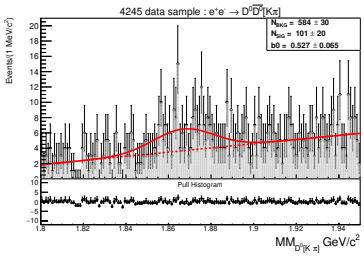

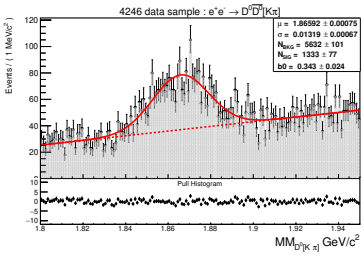

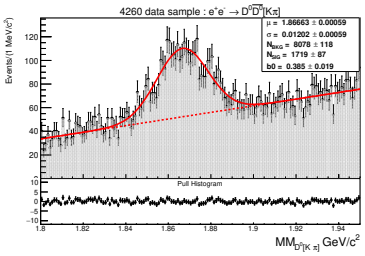

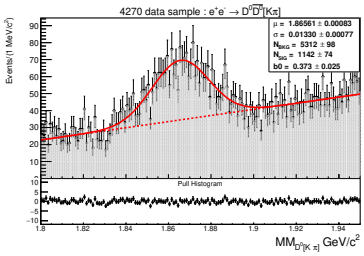

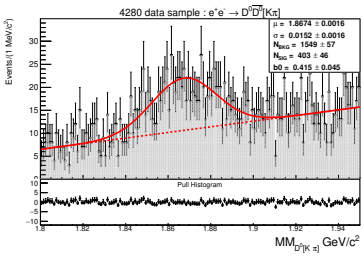

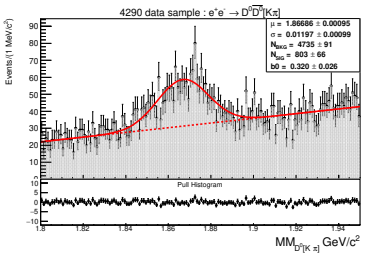

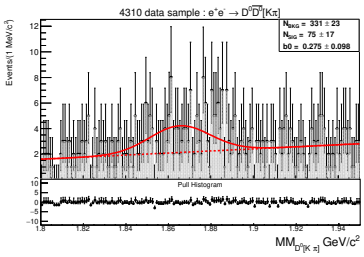

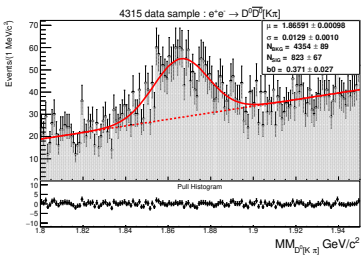

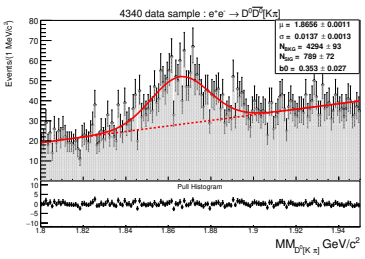

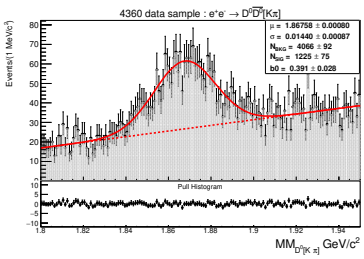

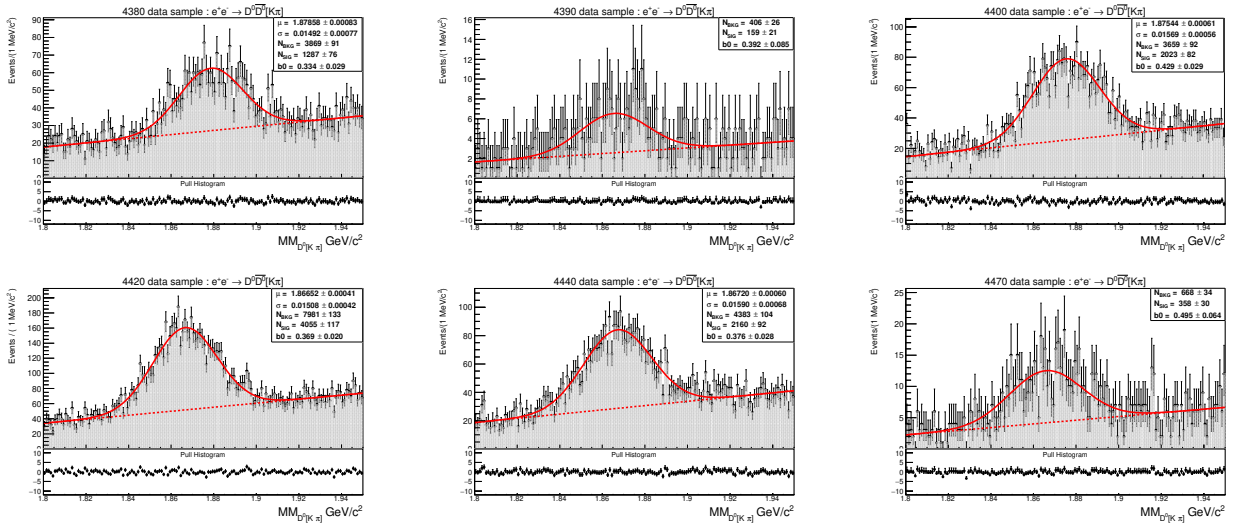

Table 5.13: D^0 in the fitted distributions of the missing mass recoiling against a $D[K^{\pm}\pi^{\pm}]$ for the XYZ BESIII data samples. The signal parameters are estimated with a chi-square fit, where the model consists of a Gaussian and a first order Chebyshev polynomial.

A.I Analysis of $e^+e^- \to D^{*0}D^0[K^{\pm}\pi^{\mp}]$

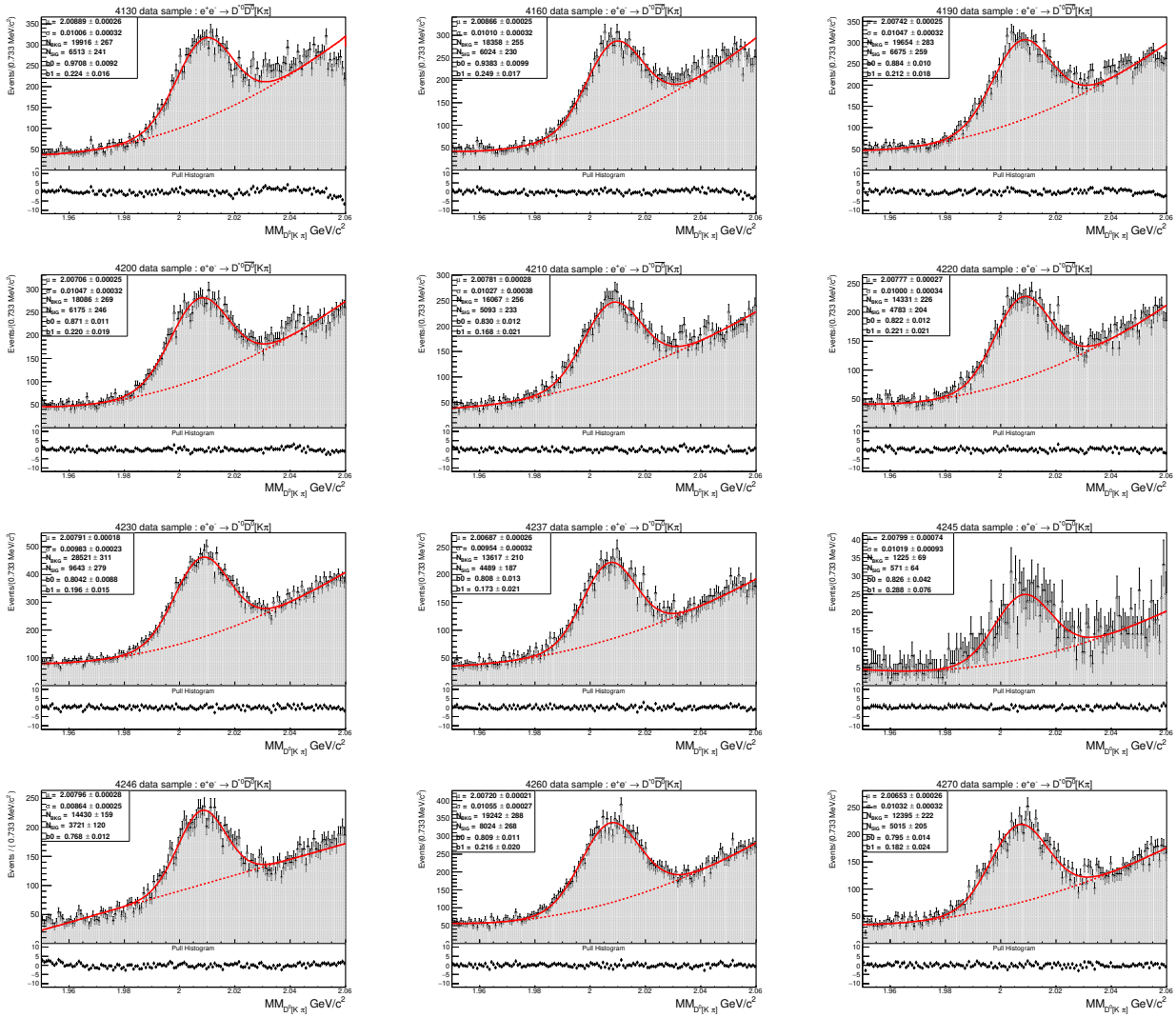

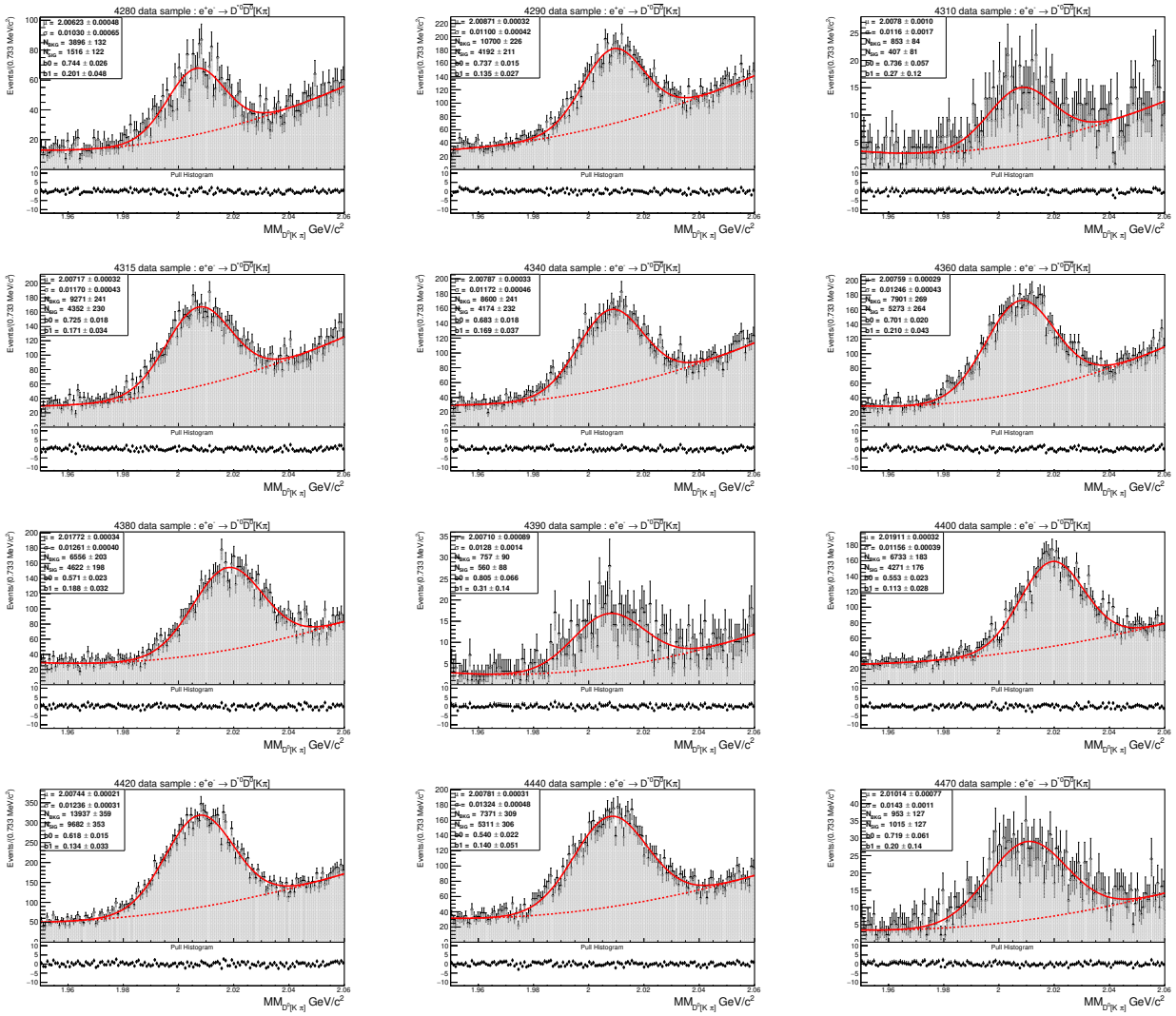

Table 5.14: D^{*0} in the fitted distributions of the missing mass recoiling against a $D[K^{\pm}\pi^{\pm}]$ for the XYZ BESIII data samples. The signal parameters are estimated with a chi-square fit, where the model consists of a Gaussian and a second order Chebyshev polynomial.

BIBLIOGRAPHY

[1] Choi, S.-K. et al. (Belle Collaboration) (2003),Physicaal Review Letters. 91 (26):262001, "Observation of a Narrow Charmoniumlike State in Exclusive $B^{\pm} \to K^{\pm}\pi^{+}\pi^{-}J/\psi$ Decays".

[2] B. Aubert et al. (BABAR Collaboration),, Phys. Rev. Lett. 95, 142001, "Observation of a Broad Structure in the $\pi+\pi-J/\psi$ Mass Spectrum around 4.26 GeV/c^2" Published 28 September 2005.

[3] M. Ablikim et al. (BESIII), Nucl. Instrum. Meth.A614, 345 (2010), 0911.4960.262001

[4] M. Ablikimet al.(BESIII Collaboration), Phys. Rev. Lett.110, 252001 (2013), "Observation of a Charged Charmoniumlike Structure in $e^{+}e^{-} \to {}^{+-}J/\psi$ at $\sqrt{s} = 4.26$âGeV"

[5] *M. Tanabashiet al.(Particle Data Group), Phys. Rev. D98, 030001 (2018) and 2019 update*

[6] Buchmann A.J. (2007) Structure of strange baryons. In: Pochodzalla J., Walcher T. (eds) Proceedings of The IX International Conference on Hypernuclear and Strange Particle Physics Springer, Berlin, Heidelberg.

[7] PDG review, Revised August 2019 by J. Huston (Michigan State U.), K. Rabbertz (KIT) and G. Zanderighi.

[8] Experimental Observation of a Heavy Particle J J. J. Aubert, U. Becker, P. J. Biggs, J. Burger, M. Chen, G. Everhart, P. Goldhagen, J. Leong, T. McCorriston, T. G. Rhoades, M. Rohde, Samuel C. C. Ting, Sau Lan Wu, and Y. Y. Lee, Phys.Rev.Lett.33, 1404 - Published 2 December 1974.

[9] E. Eichten et al. Spectrum of Charmed Quark-Antiquark Bound States.PhysicalReview Letters, 34(6), 1974.

[10] B. Aubert et al. (BaBar), Nucl. Instrum. Meth.A479, 1 (2002), hep-ex/010504

[11] A. A. Alves, Jr. et al. (LHCb), JINST3, S08005 (2008).

[12] A. Abashian et al. (Belle), Nucl. Instrum. Meth.A479, 117 (2002).

[13] GlueX Collaboration, Jonathan Zarling(Indiana U.) for the collaboration, JPS Conf.Proc. 26 (2019) 022002, "The GlueX Experiment : Recent Results and Future Plans."

[14] PANDA Collaboration (2009), arXiv:0903.3905, "Physics Performance Report for PANDA: Strong Interaction Studies with Antiprotons".

[15] X. Liu (2013),hep-ph/1312.7408.

[16] Johan Messchendorp. Physics with Charmonium A few recent highlights of BESIII. PoS, Bormio2013:043, 2013.

[17] S. K. Choi et al. (Belle Collaboration), Phys. Rev. Lett. 100 (2008) 142001.

[18] Z. Q. Liu et al. (Belle Collaboration), Phys. Rev. Lett. 110 (2013) 252002.

[19] M. Ablikim et al. (BESIII Collaboration), Phys. Rev. Lett. 111 (2013) 242001.

[20] M. Ablikim et al. (BESIII Collaboration), Phys. Rev. Lett. 118, 092002, Published 1 March 2017, "Observation of Two Resonant Structures in $e^+e^- \to h_c\pi^+\pi^-$"

[21] M. Ablikim et al. (BESIII Collaboration), PHYSICAL REVIEW D96,032004 (2017), Measurement of $e^+e^- \to \psi(3686)\pi^+\pi^-$ from 4.008 to 4.600 GeV and observation of a charged structure in the $\psi(3686)\pi^\pm$ mass spectrum.

[22] C. Z. Yuan et al. (Belle Collaboration) Phys. Rev. Lett. 99, 182004 Published 2 November 2007, "Measurement of the $e^+e^- \to \pi+\pi-J/\psi$ Cross Section Via Initial-State Radiation at Belle."

[23] M. Ablikim et al. (BESIII Collaboration), Phys. Lett.B660,315(2008), "Determination of the psi(3770), psi(4040), psi(4160) and psi(4415) resonance parameters."

[24] Zhiqing Liu et al. (BESIII Collaboration), Phys. Rev. Lett. 118, 092001 (2017), "Precise measurement of the $e^+e^- \to J/\psi\pi^+\pi^-$ cross section at BESIII".

[25] Qian Wang, Christoph Hanhart, and Qiang Zhao, Phys. Rev. Lett., 111(13):132003, 2013. "Decoding the riddle of $Y(4260)$ and $Z_c(3900)$."

[26] Shi-Lin Zhu, jphysletb.2005.08.068, "The possible interpretations of $Y(4260)$".

[27] *J. Z. Bai et al. Observation of a Near-Threshold Enhancement in the pp Mass Spectrum from Radiative $J/\psi \to \gamma pp$ Decays.* Phys. Rev. Lett., 91:022001, Jul 2003.

[28] M. Ablikim et al. Observation of a Resonance $X(1835)$ in $J/\psi \to \gamma\pi^+\pi^-\eta$. Phys.Rev. Lett., 95:262001, Dec 2005.

[29] M. Ablikim et al. Confirmation of the $X(1835)$ and Observation of the Resonances $X(2120)$ and $X(2370)$ in $J/\psi \to \gamma\pi^+\pi^-\eta$. Phys. Rev. Lett., 106:072002, Feb 2011.

[30] M. Ablikim et al., Nuclear Instruments and Methods in Physics Research Section A: Accelerators, Spectrometers, Detectors and Associated Equipment 614,345 (2010).

[31] D. Asner et al., Physics at BESIII, Int. J. Mod. Phys. A24, S1 (2009).

[32] *URL http://bes3.ihep.ac.cn/system/offline/offline.htm.*

[33] W.-D. Li et al., Int. J. Mod. Phys. A24, 9 (2009).

[34] S. Agostinelli et al. GEANT4: A Simulation toolkit.Nucl. Instrum. Meth., A506:250-303, 2003.

[35] S. Jadach, B. F. L. Ward, and Z. Wa Ì§s. Coherent exclusive exponentiation for precision Monte Carlo calculations.Phys. Rev. D, 63:113009, May 2001.

[36] Manual of event generators for e^+e^- scan experiments Rong-Gang Ping and Rui-Ling Yang (IHEP)

[37] Ping Rong-Gang. Event generators at BESIII.Chinese Physics C, 32(8):599, 2008

[38] A. Ryd. EvtGen A Monte Carlo Generator for B-Physics.Babar Analysis Document522 V6 EvtGen V00-11-06, 2004

[39] I. Adachi et al. (Belle Collaboration), Phys. Rev. Lett. 108, 032001 - Published 18 January 2012, "First Observation of the P-Wave Spin-Singlet Bottomonium States $h_b(1P)$ and $h_b(2P)$".

[40] The Belle Collaboration: K. Abe, et al Submitted on 4 Jul 2005 (v1), "Observation of a new charmonium state in double charmonium production in e^+e^- annihilation at $\sqrt{s} = 10.6$ GeV"

[41] M. Tanabashiet al.(Particle Data Group), Phys. Rev. D98, 030001 (2018) and 2019 update

[42] Maria Grazia Pia and Georg Weidenspointner on behalf of the NANO5 Team-Monte Carlo Simulations for Particle detectors- July 2012

[43] X.L.Wang et al. (Belle Collaboration),Phys.Rev.Lett.99,142002(2007); arXiv:0707.3699.

[44] BESII Collaboration, Daniel Bennett et al., Measurement of $e^+e^- \to K\bar{K}J/\psi$cross sections at center-of-mass energies from 4.189 to 4.600 GeV, PHYSICAL REVIEW D97,071101(R) 2018.

[45] Belle Collaboration, Measurement of the near-threshold $e^+e^- \to DD$ cross section using initial-state radiation, arXiv:0708.0082v3, 14 Jan 2008.

[46] BaBar Collaboration, Exclusive initial-state-radiation production of the $D\bar{D}, D^*\bar{D}, D^*\bar{D}^*$ systems, PHYSICAL REVIEW D 79, 092001 (2009).

[47] M. Ablikim et al. (BESIII Collaboration), Chin. Phys. C 39 (2015) 093001.

[48] Study of tracking efficiency and its systematic uncertainty from $J/\psi \to p\bar{p}\pi^+\pi^-$ at BESIII. arXiv:1507.03453

[49] M. Ablikim et al. Study of χ_{c1} radiative decays into a vector meson. Phys. Rev. D, 83:112005, 2011.

.